Nucleon transfer from heavy-ion reactions using the AFRODITE gamma-ray spectrometer

by

Marco Benatar

A thesis submitted in fulfilment of
the requirements for the degree of Doctor of Philosophy in the Department of Physics

University of Cape Town

Submitted 16 August 2004

Submitted in revised form : 18 November 2005

Abstract

The γ- radiation following the interactions of ^{127}I on ^{197}Au and ^{194}Pt at E_{LAB} = 730 MeV has been studied. The beam energy is approximately 9.5% above the Coulomb barrier. The aim of the present work is to study multinucleon transfer to and from the target. At energies above the Coulomb barrier, stripping and pickup reactions occur, quasi-elastic and deep-inelastic events dominate, with the target-like and projectile-like fragments remaining in contact over a sufficient period of time for degree of mass and N/Z ratio equilibration to occur. Relative intensities of various target-like fragments as well as projectile-like fragments have been extracted using the RADWARE and GRAZING program respectively. The spectroscopy of the fragments has been investigated by γ-γ coincidence techniques using the AFRODITE Spectrometer from the iThemba Laboratories. Isotopes of Au and Pt have been observed as well as other nuclei having lost or gained one to two protons in the process. Q-values are also calculated and plotted versus the relative intensities. The results of these plots are compared with the predictions of the GRAZING program. The aim of the present work is to determine whether the unpaired proton from both the projectile and the target influences the transfer of nucleons and whether the transfer is done in purely statistical way or again if the unpaired proton does play a part in the transfer. It was found that for both ^{127}I on ^{197}Au and ^{194}Pt at E_{LAB} = 730 MeV, the maximum number of transfered nucleons was only 4 and that the predictions from the GRAZING program do not agree with the extracted relative intensities from RADWARE.

I dedicate this work to the memory of my father Benedetto Baruh Benatar (Cairo 1916 - Cape Town 1991).

ACKNOWLEDGMENTS

- First of all I would like to thank my supervisors Professor D.G. Aschman, Professor J.F. Sharpey-Schafer and Dr S.M. Mullins. They have always made time for discussions and have always helped me in terms of theory and experiments. Their experience and expertise in the fields of nuclear structure and nuclear reactions have guided me past many difficulties throughout the course of this work. I also thank them for allowing me to embark on such a fascinating journey.

- I am particularly indebted to Professor Giovanni Polarollo from the INFN and Theoretical Physics Department from the University of Turin for helping me with The GRAZING program and helping me with theoretical calculations. Nanni has also taught me that Physics has no frontiers and a friendship can be developed without actually meeting him personally.

- Dr. J.J. Lawrie for his wizardry in electronics and for being a great Group Head, and Dr J.V. Pilcher for his help using the VAX system.

- Dr Given Mabala and Mr Sean Murray with whom I spent very enjoyable times were always willing to help when I had difficulties with problems concerning the computing and especially LaTeX. Sean, I owe you a lot. You have been extremely helpful and you were never annoyed when I disturbed you so often with so many questions.

- Dr Paddy Regan and Dr Carl Wheldon from Surrey University, Professor Peter Butler from Liverpool University for always answering so promptly all my questions concerning the Physics of Heavy ions as well as Dr Neil Rowley and Dr Anna Wilson.

- The invaluable help from Ms Janet Sampson from Liverpool University Physics Department is very much appreciated. Janet has been extremely kind to answer all my questions on MTsort and actually introducing me to this sorting program.

- I wish to thank the AFRODITE Group, Dr R.T. Newman, Dr E. Lawrie, Dr F.D. Smit, Ms Judith Ncapayi, Mr Phakamisa Kwinana, Dr D.G. Roux, K. Korir for helping me with the shifts.

- I would like to thank the Cyclotron team for providing a very good beam.

- Dr S.A.R Wynchank who has always been a mentor and a friend. Sinclair has been an example of what a scientist must be, kind and humble. He has been instrumental in advising me to carry on with my studies. I will never forget your kindness, wisdom and the good times spent at the MRC under your supervision. May you find in these few lines the expression of my gratitude. I would also like to thank Sinclair for proof reading this work.

- My family have continuously supported me. Their kindness and understanding have helped me get through.

- Pat, your love and support have been instrumental. You'll never understand how grateful I am. As you know, I am not good with words. You

have given up many weekends and evenings just to allow me to study and never complaining. Thank you from the bottom of my heart.

- **I am very grateful to the UCT Physics Department and iThemba Labs for their financial assistance.**

TABLE OF CONTENTS

LIST OF FIGURES

LIST OF TABLES

Chapter 1

INTRODUCTION

It is well known that when two very heavy ions collide, they do not fuse and evaporate particles to form a quasi-stable nucleus with a mass a little less than the sum of the target and projectile. Indeed it would be easy to create super heavy nuclei if they did. The boundary of fusability is given roughly by $Z_t + Z_p \leq 110$, where Z_t and Z_p refer to the charges of the target and projectile nuclei, respectively. Very heavy ions, colliding above their mutual Coulomb barrier, exchange particles and energy in deep-inelastic reactions. Alternatively, they can momentarily fuse before the coagulated nuclear matter fissions with little memory of its mode of formation.

A difficulty of studying the details of these reactions by heavy ion detection methods, is that it is difficult to design detectors with sufficient Z and A resolution to separate out the individual nuclei produced. In addition, no information is given on the excitation energies and angular momenta of the nuclei.

Recently there have been pioneering studies of such reactions using large array of γ-ray detectors to identify excited reaction products. Daly et al. [Dal95] have used GAMMASPHERE [Lee90] to study the reaction ^{124}Sn + ^{136}Xe at 655 MeV. The nuclei populated are shown in Fig. 1.1. It can be seen that more nuclei are populated on the neutron deficient rather than the neutron rich side of the target nucleus. This suggests that after collision, the nuclei are highly excited and boil off neutrons in the usual manner. In Fig. 1.3 the results of Cocks et al.

[Coc00] are shown for 362 MeV ^{56}Fe ions incident on a target of ^{232}Th. They see many nuclei with some neutrons and protons removed from the target. They also see nuclei corresponding to fusion-fission reactions. The TARDIS [Lhe96] spectrometer at Jyväskylä was used for their measurements. These studies are very new, as high resolution efficient γ-ray arrays have not previously been available on accelerators of very heavy ions. The iThemba LABS Separated Sector Cyclotron (SSC) can produce beams of Xe ions above the Coulomb barrier on most targets. The advent of good Ge detectors in escape suppression shields allows coincident γ-ray measurements to be made which will uniquely define the reaction products. In addition information can be obtained on the input angular momentum and excitation energy. This can be done by observing coincidences between target-like and projectile-like residual nuclei and determining how many neutrons/protons have boiled off. The interesting questions to try and answer in this work are the following:

- How are transfers affected by whether there is an unpaired proton in the target?
- Are pairs of paired neutrons/protons preferentially exchanged due to the quantum nature of the nuclear fluid?
- Are nucleons exchanged in an entirely statistical manner?
- Do such collisions show any preference for populating any particular shape?

The answer to these questions will be found in Chapter 5 (Conclusions).

In this thesis, the reactions using a ^{127}I beam bombarding thick targets of ^{197}Au and ^{194}Pt at about 10% above the Coulomb barrier have been studied. The aim was to measure the relative cross-sections/yields of channels like:

$^{127}\mathrm{I} + {}^{197}\mathrm{Au} \rightarrow {}^{126}\mathrm{Te} + {}^{(198-x)}\mathrm{Hg} + x\mathrm{n}$

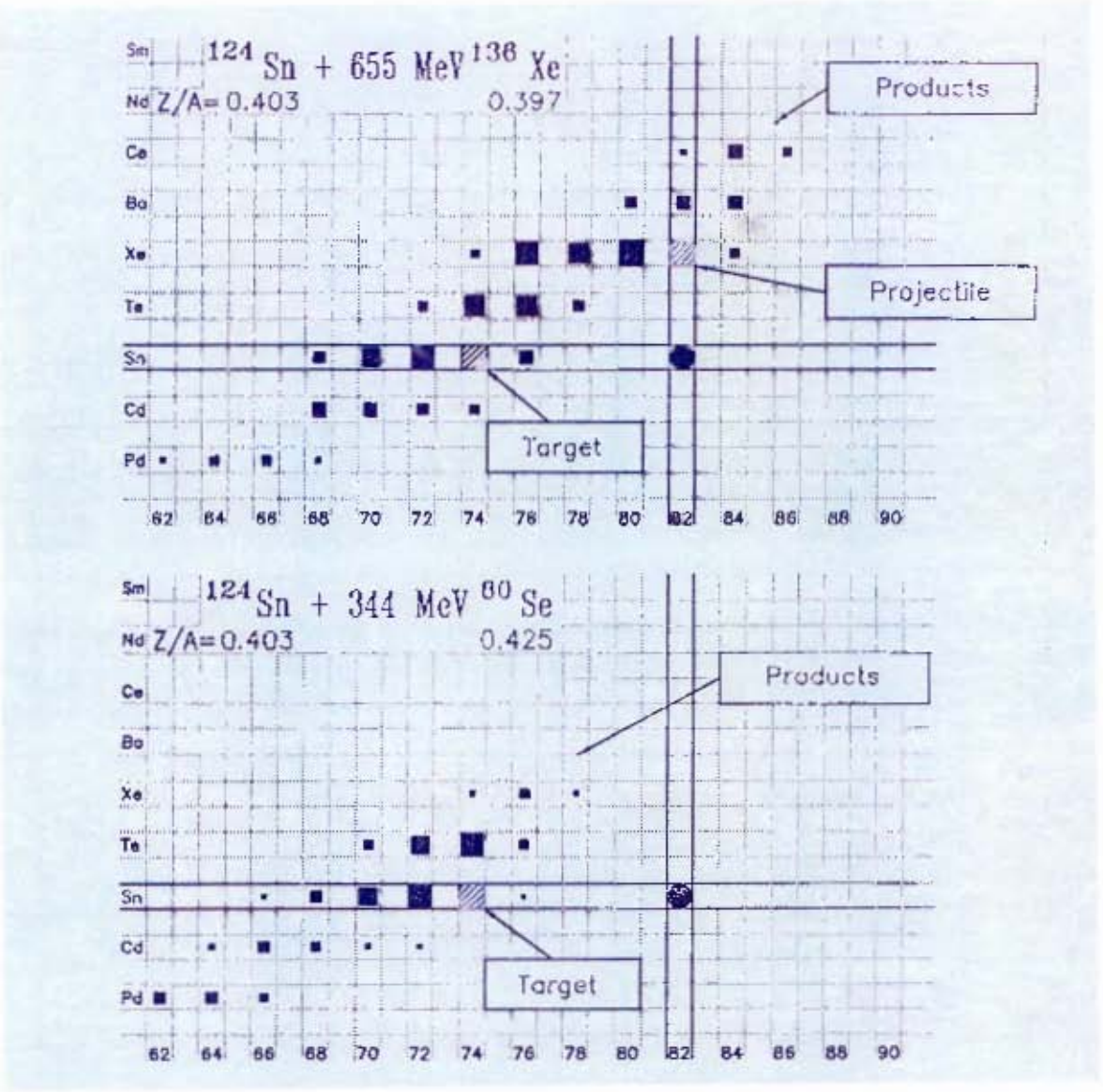

Figure 1.1: Relative yields of even-even products of the reactions indicated in the plot. Sizes of the black boxes indicate the measured intensity ratio $I_\gamma(4^+ \rightarrow 2^+)/I_\gamma(2^+ \rightarrow 0^+)$. Target and projectile squares are cross-hatched [Dra96] after [Dal95]

$^{127}\mathrm{I} + {}^{197}\mathrm{Au} \rightarrow {}^{128}\mathrm{Xe} + {}^{(196-x)}\mathrm{Pt} + x\mathrm{n}$

The advantage of studying proton transfer in this manner is that the residual nuclei all have their first excited states at quite high energies, making for easy identification. Stripping or pickup of a single nucleon are the simplest examples of transfer reactions [Lil90]. The utilization of heavy ion beams for the study of transfer reactions appears to be a modern development, yet as early as 1952 a proposal by Breit et al. was submitted. This early experiment proposal consisted when deuteron-stripping reactions were being assessed as powerful probes into single aspects of nuclear structure [Gol79]. The technical problems in accelerating and detecting heavy nuclei have delayed the implementation of this proposal until about 1979. In spite of the relatively slow technological development of heavy ion production and detection,the theory has been enriched by the efforts made in understanding conventional light ion experiments. One of the many advantages of using heavy ions is the fact that it can supplement what has been obtained by other means. It is useful in addition, to repeat measurements of certain nuclear states, by using different beams so as to validate questionable measurements and the use of heavy ions allow one to reach states of high angular momentum.

The quality of the beam is of crucial importance. Heavy ion beams can be obtained from cyclotrons, tandem Van de Graaf accelerators and linear accelerators.

Particle identification in heavy ion reactions is of course of primary importance, and will be be discussed in Chapter 3 and 4. However, two quantities in addition to the energy of a particle must be measured, namely the mass and the nuclear charge Z if identification is to be made of the emitted nuclei. Some techniques are useful but not used in the present work, but will be briefly described.

- Measurement of energy loss ΔE and the energy E, using the relationship $\Delta E \simeq MZ^2E^{-1}$, from which one deduces the quantity MZ^2. This is usually unique if the nuclei not too far away from the line of stability with $M \simeq 2Z$. The advantage of using the ΔE-E telescope system, as compared to magnetic analyzer systems, is the fact that almost the whole mass-charge spectrum of the reaction products is obtainable simultaneously in one measurement.

- Measurement of time of flight and energy gives a determination of the mass according to $t = (2E/M)^{1/2}/S$, where S refers to the flight path. The advantage of the method used in this work is that known γ-rays fix this quantity exactly.

- Coincidence between kinematically correlated events. This method is applicable mainly to reactions in which both the target and the projectile are of similar mass and where the measurements are confined to the intermediate angular range ($\theta_{c.m} = 90°$) where θ is the angle of a detector relative to another one. In certain circumstances kinematical coincidences combined with ΔE-E techniques can give a powerful and clean separation of reaction products. There is however a disadvantage: it yields only one transition to a single final state [Gol79], whereas in the present work known γ-rays fix these quantities exactly.

1.1 Deep-Inelastic Reactions

The first observation of deep inelastic reactions came in experiments performed by Kaufmann and Wolfgang [Kau59], [Kau61], [Kau61b]. They have studied complex nucleon transfer reactions using 10 MeV/nucleon ^{16}O and ^{14}N beams with targets of aluminium, copper and tin. The observation was that the

cross sections for the final reaction products showed a much weaker dependence than the exponential decrease with the number of nucleons transfered between the target and the projectile nuclei than that predicted by quantum tunneling process, and that there was a relatively weak correlation of cross section with the binding energy of exchanged groups of nucleons as well as the Q-value of the reaction. It was proposed that a grazing contact reaction mechanism existed covering a range of impact parameters intermediate to those of capture and quasi-elastic reactions for which the Coulomb and centrifugal repulsion was greater than the nuclear surface attraction. The different driving mechanisms for the different degrees of freedom mean that the neutron-to-proton (N/Z) ratio, energy, angular momentum and mass equilibrate at different rates. A non-zero impact parameter will set the system rotating and the angle of rotation will increase with time. Reaction fragments emitted at small rotation angles arise from the early stage of the reaction. Using this reaction clock, it has been observed that the kinetic energy equilibrates first in around 10^{-22} seconds. Angular momentum equilibrates next, then mass equilibration takes place approximately 50 times longer than N/Z equilibration: This process is slow and is not complete when the dinuclear system is forced apart by Coulomb and centrifugal repulsion. The result is the formation of target-like and projectile-like fragments. In such reactions, where the projectile nucleus is incident upon the target at an energy above the Coulomb barrier but where the formation of a compound nucleus is inhibited, the interacting nuclei come together long enough to exchange some number of nucleons before flying apart. The two outgoing fragments share the angular momentum and excitation energy brought about by the reaction. The angular momentum is divided into three components - that of the target-like fragment, that of the projectile fragment and the relative motion between the two. This last component depends on the degree of contact between the beam and target nuclei. Studies have shown

that, in multi-nucleon transfer reactions, it accounts on average for something close to 5/7 [Boc77], [Tak88] of the total angular momentum available in the reaction, the amount one would expect using a classical model of the motion of colliding spheres. Either fragment or both may emit one or more neutrons and/or protons if their excitation is high enough, and then decay via γ-ray emission. Deep-inelastic reactions result in the population of a large range of product nuclei, with most of the intensity concentrated close to the target or projectile system. The N/Z ratio of the product nuclei tends toward that of the compound system. The following features of deep-inelastic reactions have emerged from the vast amount of experimental and theoretical work carried out [Mor81], [Sch84], [Gob80], [Bas80], [Hib93]:

(a) The reaction is fundamentally a binary process.

(b) There is damping of the entrance-channel kinetic energy, with the final kinetic energies of the reaction products varying from essentially elastic energies down to the Coulomb interaction energy between fragments.

(c) Neck formation enables nucleon exchange between the two reacting nuclei, resulting in mass distribution with a width determined by the interaction time and the potential energy of the intermediary complex.

(d) The angular distributions of the projectile-like fragments are either side-peaked or forward-peaked, showing that the interaction times are typically shorter than the rotational period of the dinuclear system.

(e) The average neutron-to-proton ratio of the projectile-like and target-like fragments evolves towards the value which minimizes the potential energy of the intermediate complex.

(f) Angular momentum is transfered from relative orbital motion to the intrinsic spin of the two primary fragments.

(e) The primary fragments produced de-excite mainly through the evaporation of light particles (neutrons, protons, and α particles), the emission γ-rays

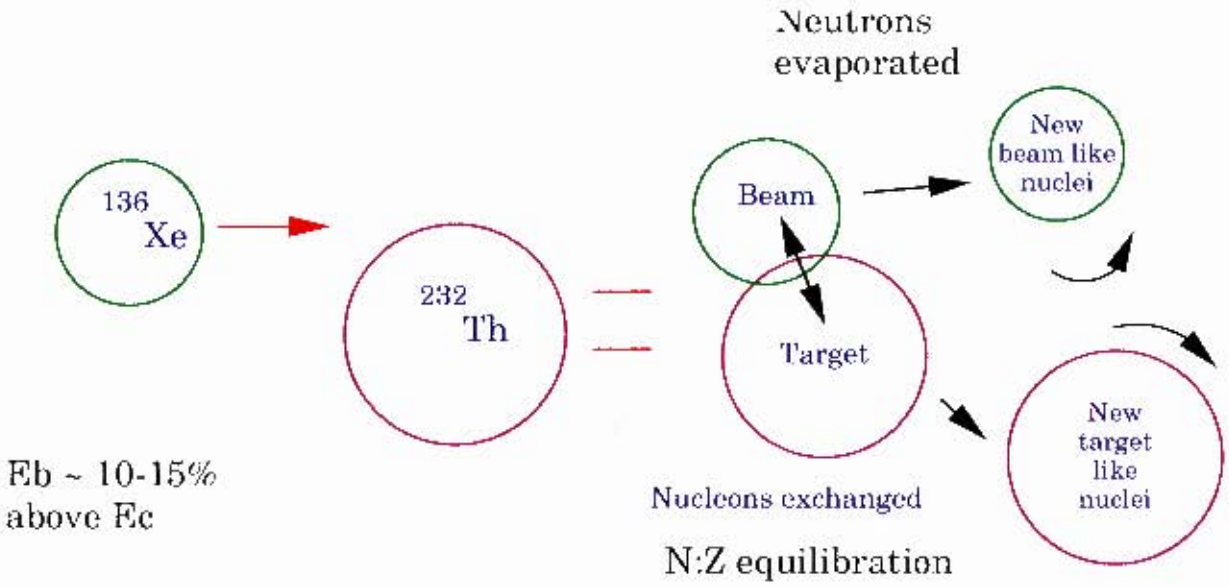

Figure 1.2: Schematic of the use of deep inelastic collisions to populate yrast states of neutron rich nuclei [Reg00].

and in the case of very heavy fragments via fission.

For neutron rich nuclei, it is difficult to observe the yrast sequence to high spins (such as through the backbend) due to preferential population of neutron-deficient species in fusion-evaporation reaction at low angular momentum involved [Reg97]. The use of deep- inelastic reactions provides an efficient way of studying the yrast states of stable and slightly neutron rich nuclei. Fig.1.2 illustrates clearly the use of deep inelastic reactions to populate neutron rich nuclei. It has been shown experimentally that the binary system equilibrates into systems with approximately N/Z ratios [Kro03]. This means that the extra neutron excess of heavy, stable targets, indicate that bombarding these with lighter beams usually results in an overall flow of neutrons onto the the lighter, beam like fragments. However evaporation of charged particles is strongly hindered by the Coulomb barrier, and thus the total charge Z of the compound sys-

tem ($Z_{beam} + Z_{target}$) is usually conserved in the break up. Typically, between 2 and 6 neutrons will be evaporated from the two hot binary fragments and thus a specific nucleus will be accompanied by a number of binary partner nuclei, comprising of between 2 and 4 isotopes of the same element. To avoid dealing with large recoil velocities in the present work, thick targets were used which stop the beam-like fragments and target-like fragments inside the target. Hence, decays with apparent lifetimes greater than the stopping time have no Doppler shift and can be easily resolved. As an example, in the reaction ^{86}Kr + ^{110}Pd [Reg97], the maximum spin obtained was 14^+ for ^{104}Ru, which is high enough to get useful insights into the alignment processes. In heavier deformed nuclei, higher spins can be obtained using binary reactions with thick/backed targets and high efficiency γ-ray arrays. These high efficiency arrays give rise to very clean spectra, with only the nucleus of interest and a few binary partners. The following illustration (Fig. 1.3) is the case of such distribution of target-like products from the reaction ^{56}Fe + ^{232}Th. This experiment was performed using the GAMMASPHERE array [Coc00].

The deep-inelastic reaction mechanism has been studied at length [Bas80], [Sh84], initially through experiments measuring energy, angle, charge and mass of the reaction products.

Using transfer reactions, one can produce nuclei far from the line of stability, depending on the choice of beam and target. Such nuclei can be subjected to spectroscopic studies using high efficiency γ-ray detector arrays.

The advent of high efficiency, multi-detector arrays [Sha88] enables studies of both reaction mechanisms and the spectroscopy of neutron-rich nuclei. The above statement has been demonstrated by investigations of various fissioning systems [Boc82], [Abd87], [Hot90], [Hot91]. In our case we concentrate on the study of multi-nucleon transfer reaction using a high efficiency γ-ray array namely AFRODITE to probe the physics of deep-inelastic and grazing

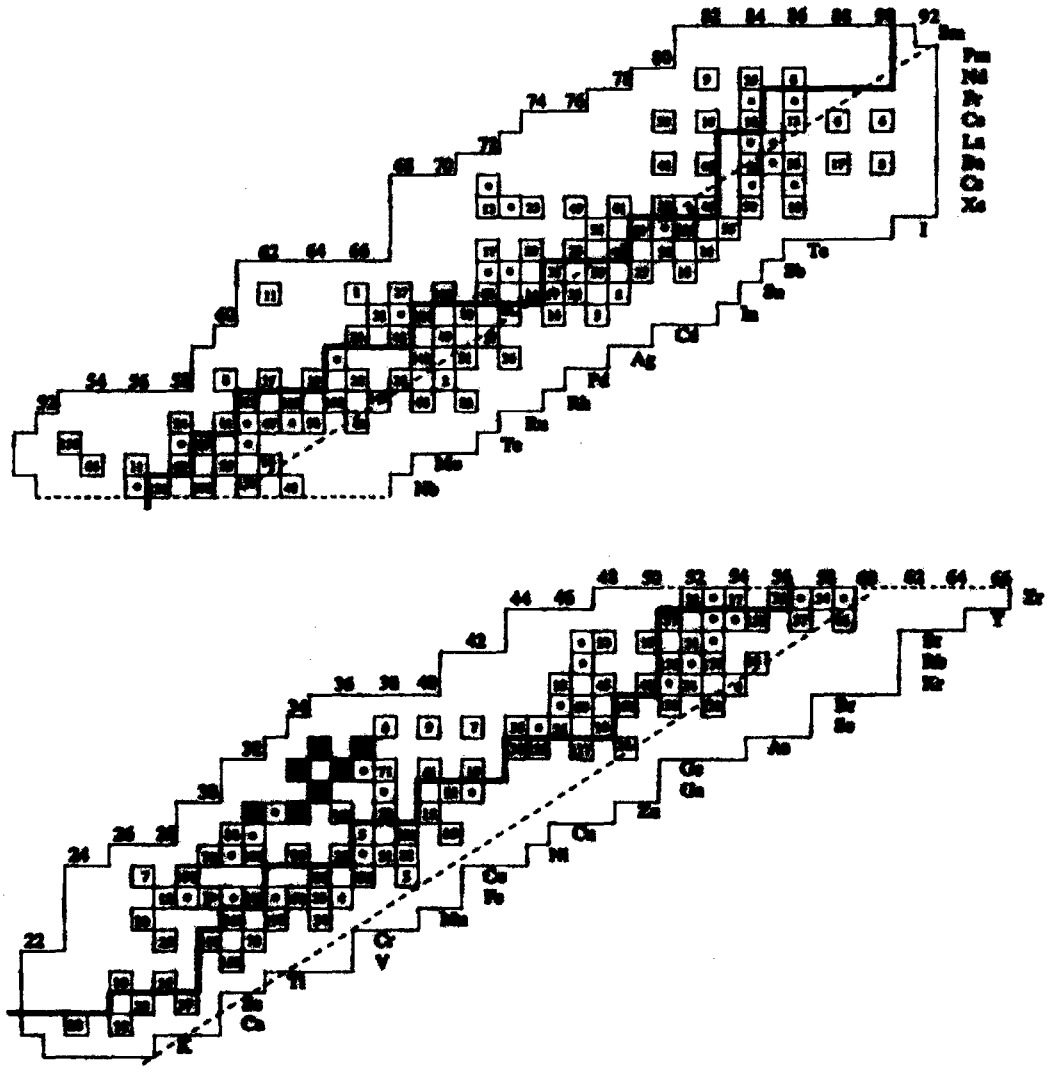

Figure 1.3: Distribution of target-like products in ^{56}Fe + ^{232}Th at 362 MeV [Coc00].

reactions.

Deep-inelastic reactions are not efficient in generating high spin states, particularly in the case of the present work where both ^{197}Au and ^{194}Pt are not deformed. Unlike fusion-evaporation reactions, not all of the input angular momentum of the reaction goes into the intrinsic angular momentum of the final products. Most of the angular momentum goes into the relative spin of the two fragments with respect to each other. Classically, it can be shown that in the presence of strong friction between two rolling spheres (i.e the target and the beam like nuclei), known as the rolling limit, $\frac{5}{7}$ of the maximum initial maximum angular momentum (for a grazing collision), L_{max} goes into the relative motion of the two fragments while only $\frac{2}{7}$ goes into the intrinsic spins of the beam and target-like fragments respectively [Boc82]. The maximum input spin into the beam and target like fragments (BLF and TLF) A_B and A_T can be estimated using semi-classical expressions and will be derived in the next chapter. By increasing the beam energy, one increases the angular momentum input of the target and beam nuclei.
Multi-nucleon transfer reactions have recently been used for a number of applications in nuclear structure:

- P.J. Daly et al. produced Yrast excitations in hard to reach $Z \sim 50$ neutron-rich nuclei produced in deep-inelastic collisions by studying γ-ray coincidence measurements using multidetector arrays [Dal95].

- Butler et al. [But98] have used multinucleon transfer reactions to study the population of octupole nuclei in the actinide region.

- Wilson et al. [Wil00] have also shown that the use of deep-inelastic multinucleon transfer reactions is useful for reaching high spin states. Deep-inelastic reactions populate relatively high angular momentum states in

nuclei along the valley of stability and even towards the neutron rich side of the Segrè chart.

- Rejmund et al. [Rej98] have also published a very interesting paper describing the use of multinucleon transfer reactions in order to study the γ spectroscopy of ^{209}Pb with deep inelastic reactions. These results are interesting as ^{209}Pb is a doubly magic nucleus plus one neutron. In order to get to their result, again fusion-evaporation reactions were not a suitable tool for their study. They have used ^{76}Ge, ^{136}Xe, and ^{208}Pb beams on a ^{208}Pb target at 12% above the Coulomb barrier. In a similar study, Rejmund et al. [Rej97], have populated ^{210}Pb using the same reactions at about 50 MeV above the Coulomb barrier, where a thick ^{208}Pb target was used. ^{136}Xe and ^{208}Pb beams were used in this experiment. They have found four new states above the 8^+ isomer in ^{210}Pb.

- R. Broda et al. [Bro90] have demonstrated that also in the vicinity of doubly closed shell nuclei around ^{208}Pb, the study of high spin states is possible using thick target method of gamma spectroscopy in deep-inelastic reactions.

- By extending the field of spectroscopy to very neutron-rich heavy nuclei has been impaired by reaction Q-values that consistently favor the formation of the lighter isotopes, Dasso et al. [Das94] carried out a systematic study of cross sections for multi-nucleon transfer processes in order to determine the actual neutron excess in the projectiles that is needed to reverse the aforementioned tendency.

- In his paper on multinucleon transfer, G. Pollarolo introduces the GRAZING program [Pol99], which will be used in this thesis in the results sec-

tion. In this work, Pollarolo discusses transfer reactions between heavy ions with special emphasis on multi-nucleon transfer, by using a semi-classical model that incorporates, in an independent description, both inelastic excitation to collective states and one particle transfer channels.

- In their publication, Kratz et al. [Krat81] also used a ^{197}Au target being bombarded by various Xe isotopes namely ^{129}Xe, ^{132}Xe and ^{136}Xe. The unpaired nucleon in ^{129}Xe is a neutron whereas in the present work the unpaired nucleon is a proton. They have studied the N/Z ratios of light and heavy fragments from the collisions mentioned just above the interaction barrier.

- In their work, Corradi et al. [Cor01] have studied the distinction between the maximum number of nucleons transferred and the maximum one might expect to observe. The study was performed at Legnaro on studying multinucleon transfers through charged-particle experiments.

- Funke et al. [Fun96] have studied quasi-elastic transfer reactions in ^{197}Au + ^{197}Au and ^{197}Au + ^{238}U collisions near the Coulomb barrier. Differential cross sections as a function of centre of mass angle were measured for 1n and 2n transfer reactions in ^{197}Au + ^{238}U and ^{197}Au + ^{197}Au reactions. In this experiment, they have used an even-even system and a odd-even system to study reactions, but near the Coulomb barrier and sometimes below.

The above is certainly not an exhaustive list of applications of transfer reactions, but it gives the reader a good idea of the importance of such methods for their applications in nuclear structure. The novelty of this work is by using an odd-even projectile namely ^{127}I on an odd-even target,^{197}Au,and an even-even

target in a second experiment, namely ^{194}Pt at around 9% above the Coulomb barrier. In all of the above references, one will notice that all the reactions involved even-even beams on even-even targets except for Kratz et al. who have used an odd-even beam on an odd-even target, but as mentioned the unpaired nucleon in Kratz's work is a neutron. In Funke et al. work [Fun96], an even-even system and a odd-even system were used to study reactions, but near the Coulomb barrier and sometimes below.

Chapter 2

THEORY

In this chapter an overview of some nuclear reactions that take place in order to produce the results described in this thesis is given.

2.1 Reactions between Heavy Ions

The interaction between a heavy ion projectile (a nucleus containing more than 4 nucleons) with an energy of less than 10 MeV/nucleon and a target nucleus may have a number of outcomes. The reaction is determined by: the centre of mass energy, the angular momentum L (or impact parameter b as in the classical limit $L\hbar = pb$ with p being the projectile momentum, and the nature of the projectile and the target (mass, charge). Even at low energy (5 MeV/nucleon), heavy ions have a short wavelength compared to the dimensions of the collision region around the target nucleus. The projectile can then be seen as a classical particle moving with a well defined trajectory, and using this semi-classical picture the various reaction types can be classified according to their angular momentum or simply their impact parameter b. The impact parameter specifies how close the collision is to being central or head-on. All impact parameters are possible but the smaller impact parameters are less likely because of the smaller cross-sectional area [Hib93], [Sch84], [Tak88], [Boc77].
The main reaction types are, in order of descending impact parameter:

- Elastic scattering involves no loss of kinetic energy, just a change in direction of the projectile and the target. Coulomb excitation results from

the conversion of kinetic energy to internal excitation of the reacting nuclei via the long range Coulomb interaction. In this reaction, no nuclear forces are involved.

- Quasi-elastic reactions.

  Quasi-elastic reactions consist of nuclear elastic and inelastic scattering and the transfer of a few nucleons. These collisions are peripheral (grazing) and involve the nuclear surfaces and take place during the transit time of the projectile, of the order of 10^{-22} seconds, with the reaction products strongly focused around the grazing angle.

- Deep-inelastic reactions.

  Deep inelastic reactions involve substantial mass flow and an important transfer of incident kinetic energy into internal excitation of the reacting nuclei. The large mass and charge of heavy ions increase the Coulomb and centrifugal repulsion which combines with the energy damping or dissipation to prevent the complete fusion of the two nuclei. Deep-inelastic reactions take place in around 10^{-21} to 10^{-22} seconds.

- Quasi-fission reactions.

  In these reactions, massive mass transfer takes place without the mononuclear intermediate going through an equilibrated compound nucleus stage. These reactions occur on a time scale of 10^{-19} to 10^{-21} seconds.

- Compound nuclear processes.

  In these reactions the two nuclei fully fuse to form an equilibrated compound nucleus (Fusion reactions) and are long lived (10^{-16} to 10^{-20} seconds) as opposed to the treatment of quasi-fission reactions and de-excite

via nucleon evaporation or fission. The fusion of two interacting nuclei with charge products greater than 2000 is severely inhibited [Qui93]. This inhibition is brought about by the large Coulomb potential and the centrifugal repulsion for non-zero impact parameters, combined with the rapid dissipation of relative kinetic energy as the nuclei approach each other. It is is therefore obvious from the above statement that in the present work where the products of the charges for the reactions ^{197}Au + ^{127}I and ^{194}Pt + ^{127}I, are 4187 and 4154 respectively, hence quasi-fission and compound nuclear processes do not apply and no fusion can be observed.

2.1.1 Motion of Touching Spheres

When a nucleus of radius r_p approaches a target nucleus of radius r_t at an impact parameter such that the initial angular momentum is L, there would be a distribution of L values corresponding the range of partial waves which contribute to the deep-inelastic process. After contact, the spheres will move around the centre of mass with an angular speed ω. Each sphere may have its own intrinsic rotation, ω_t and ω_p and ω_t. The law of conservation of angular momentum requires:

$$L = \mu R^2 \omega + I_p \omega_p + I_t \omega_t \tag{2.1}$$

where R = r_p + r_t and the reduced mass, μ, is given in terms of the target and projectile mass numbers (A_p and A_t) as

$$\mu = \frac{A_p A_t}{A_p + A_t} \tag{2.2}$$

$J_p = I_p \omega_p$ and $J_t = I_t \omega_t$ are the intrinsic angular momenta of the projectile and target, whose calculated values can be compared with those obtained experimentally. The sharing of the angular momenta between relative and intrinsic rotation depends upon the details of the frictional forces between the

nuclei. The particular cases of interest are sliding, rolling and sticking which correspond to minimum, intermediate and maximum angular momentum dissipation from relative motion.

2.1.1.1 Sliding

Motion of the target and projectile where they slide with respect to one another is the simplest case to consider. There is no intrinsic rotation at all and the relative motion: $\omega_p = \omega_t = 0$ and hence $J_t = J_p = 0$. Then Eq. 2.1 reduces to $L = \mu R^2 \omega$ which gives the relative angular speed as $\omega = \frac{L}{\mu R^2}$

2.1.1.2 Sticking

In the case of the projectile and the target sticking together, each sphere rotates around its own centre at the same angular speed, and this angular speed is the relative one, i.e. $\omega_p = \omega_t = \omega$. Eq. 2.1 becomes

$$L = \mu R^2 \omega + I_p \omega + I_t \omega \tag{2.3}$$

which gives the relative angular speed as

$$\omega = \frac{L}{\mu R^2 + I_p + I_t} \tag{2.4}$$

then $J_p = \frac{I_p}{\mu R^2 + I_p + I_t} L$ and $J_t = \frac{I_t}{\mu R^2 + I_p + I_t} L$. The absolute value of these angular momenta are therefore dependent upon the partial wave distribution. For the moment of inertia of a nucleus, $I = \frac{2}{5} A r^2$, and $r = 1.2 A^{\frac{1}{3}}$, where A is the mass number of the nucleus and r is its radius, the ratio of the target to projectile angular momenta can be evaluated:

$$\frac{J_p}{J_t} = \frac{I_p}{I_t} = \frac{A_p r_p^2}{A_t r_t^2} = \left(\frac{A_p}{A_t}\right)^{\frac{5}{3}} \tag{2.5}$$

2.1.1.3 Rolling

Sticking immediately after contact is the extreme conversion of translational to rotational energy. An intermediate situation between sliding and sticking can arise in the presence of strong friction: rolling. In the case of angular speeds of the target and the projectile ω_t and ω_p, with the rotation of the line of centres taken as ω, then:

$$\omega_p > \omega \tag{2.6}$$

the point of contact between the two spheres moves forward a distance:

$$(\omega_p - \omega)r_p \tag{2.7}$$

on the surface of the projectile. The condition for no sliding is given by:

$$(\omega_p - \omega)r_p = -(\omega_t - \omega)r_t \tag{2.8}$$

When combined with the conservation of angular momentum given by Eq. 2.1, there are two equations for three variables: ω_p, ω_t and ω. There are further constraints for rolling. The usual assumption is that of purely tangential friction. This leads to equal and opposite frictional forces, $\vec{F}$, acting at the contact point. This tangential force gives a torque on the projectile: $\vec{F}\times\vec{r_p}\rightarrow\vec{J_p}$ and a torque on the target nucleus gives: $-\vec{F}\times\vec{r_t}\rightarrow\vec{J_t}$ Therefore the angular momentum sharing is given by:

$$\frac{J_p}{J_t} = \frac{r_p}{r_t} = \left(\frac{A_p}{A_t}\right)^{\frac{1}{3}} \tag{2.9}$$

To calculate the amount of angular momentum that has been converted into relative motion and the absolute magnitudes for the angular momenta of the target and projectile, Eqs. 2.1 and 2.8 must be solved simultaneously with the condition that $\frac{J_p}{J_t} = \frac{r_p}{r_t} = \frac{I_p\omega_p}{I_t\omega_t}$ namely:

$$\frac{\omega_p}{\omega_t} = \frac{I_t r_p}{I_p r_t} \tag{2.10}$$

Eq. 2.8 gives $\omega_p r_p - \omega r_p = -\omega_t r_t + \omega r_t$ $\omega_p r_p = \omega(r_p + r_t) - \omega_t r_t = \omega R - \omega_t r_t$ $\omega_p = \omega\frac{R}{r_p} - \omega_t\frac{r_t}{r_p}$ but from Eq.2.10: $\omega_p = \omega_t\frac{I_t r_p}{I_p r_t}$ hence $\omega_t\frac{I_t r_p}{I_p r_t} + \omega_t\frac{r_t}{r_p} = \omega\frac{R}{r_p}$ $\omega_t\frac{I_t r_p^2 + I_p r_t^2}{I_p r_t r_p} = \omega\frac{R}{r_p}$ $\omega_t = \frac{I_p r_t R\omega}{I_t r_p^2 + I_p r_t^2}$ and using:
$\omega_p = \frac{I_t r_p R\omega}{I_t r_p^2 + I_p r_t^2}$. The sum of the angular momenta of the projectile and target is then given by:

$$\begin{aligned} J_p + J_t &= I_p\omega_p + I_t\omega_t && (2.11)\\ &= \frac{I_p I_t r_p R\omega + I_t I_p r_t R\omega}{I_t r_p^2 + I_p r_t^2} && (2.12)\\ &= \frac{I_p I_t R\omega(r_p + r_t)}{I_t r_p^2 + I_p r_t^2} && (2.13)\\ &= \frac{I_p I_t R^2\omega}{I_t r_p^2 + I_p r_t^2} && (2.14) \end{aligned}$$

but

$$I_p = \frac{2}{5}A_p r_p^2 \qquad (2.15)$$

and

$$I_t = \frac{2}{5}A_t r_t^2 \qquad (2.16)$$

hence:

$$J_p + J_t = \frac{2}{5}\frac{A_p A_t r_p^2 r_t^2 R^2\omega}{A_t r_t^2 r_p^2 + A_p r_p^2 r_t^2} = \frac{2}{5}\frac{A_p A_t}{A_p + A_t}R^2\omega = \frac{2}{5}\mu R^2\omega \qquad (2.17)$$

and

$$L = \mu R^2\omega + J_p + J_t = \mu R^2\omega + \frac{2}{5}\mu R^2\omega = \frac{7}{5}\mu R^2\omega \qquad (2.18)$$

i.e. $\omega = (\frac{5}{7})(\frac{L}{\mu R^2})$ Therefore

$$J_p + J_t = \frac{2}{7}L \qquad (2.19)$$

and $L_{rel} = \mu R^2\omega = \frac{5}{7}L$. The fraction $\frac{2}{7}$ of the initial angular momentum is converted into angular momenta of the target and the projectile, while $\frac{5}{7}$ stays in

relative motion. Combining Eq. 2.3 and Eq. 2.5 yields

$$J_p = \frac{2}{7}\left(\frac{1}{1+\left(\frac{A_t}{A_p}\right)^{\frac{1}{3}}}\right)L \tag{2.20}$$

$$J_t = \frac{2}{7}\left(\frac{1}{1+\left(\frac{A_p}{A_t}\right)^{\frac{1}{3}}}\right)L \tag{2.21}$$

where for deep-inelastic reactions, L can be estimated as:

$$L = 0.219R[\mu(E_{CM} - V_{CM})]^{1/2} \tag{2.22}$$

the units of L are in $\hbar$ and R = 1.16 $[(A_1)^{1/3} + (A_2)^{1/3} + 2]$ fm and A is in atomic mass units. E_{CM} and V_{CM} are the beam energy and the Coulomb barrier in the center of mass respectively. These equations,derived above, allow one to estimate the angular momentum of a given fragment. Recent studies show that it is possible to estimate the angular momentum transfer into the two fragments [Reg03], [Lee97], [Val04].

2.2 The GRAZING Program

The GRAZING program has been developed over many years at the Niels Bohr Institute in Copenhagen by A.Winther [Win94] and used extensively by G. Pollarolo [Pol02], and has been used very successfully in the describing of grazing reactions. In particular one has been able to elucidate the importance of one-particle transfer channels in the imaginary part of the optical potential and also in the polarization potential [Pol99]. In the semi-classical description of grazing reactions one uses a basis that is a product of the eigenstates of the two separated ions. The relative motion is treated classically. For more information on this treatment, the reader is referred to Broglia and Winther [Bro91]. The input parameters for the program are the beam energy, and the proton number

of both the projectile and target. The calculations were performed in Italy by G. Pollarolo. In brief, in this model, the collision between two heavy ions has been reduced to the study of the redistribution in time of nucleons among two single particle density distributions that move along classical trajectories. This approximation is justified, *a posteriori*, by the fact that the change in population of the different single particle states in the projectile and target is quite small. The outcome of the reaction is determined by well known form factors for one-particle transfer and the excitation of collective states, from the actual binding energies of the two nuclei and by the average single particle level density. The values of the cross sections for the different channels are determined by the width of the Q-value windows that is centered at the optimum Q-value.

Chapter 3

GAMMA-RAY DETECTION

3.1 Gamma-Ray Detection

The study of γ-rays emitted from highly excited nuclei can reveal much about the internal structure of the nucleus. This has led to the development of more advanced detectors and detector arrays. Complementary advances have also had to have been made in the data acquisition systems and analysis software used to sort and analyze the resulting data.

This section will discuss the various interactions of γ rays and their detection by various detectors as well as the advantages and disadvantages of these various detectors.

3.1.1 Gamma-Ray Interactions

There are three major interaction mechanisms for γ rays in matter that are of interest in γ-ray spectroscopy: photo-electric absorption, Compton scattering and pair production. These all involve the partial or complete transfer of the incident γ-ray energy into the detector material. The three interaction mechanisms relative strengths are illustrated in Figs. 3.1, 3.2 and 3.3.

- Photo-electric Absorption. Photo-electric absorption occurs when a photon completely transfers its energy to one of the bound electrons of an atom. The kinetic energy of the ejected electron is equal to the photon

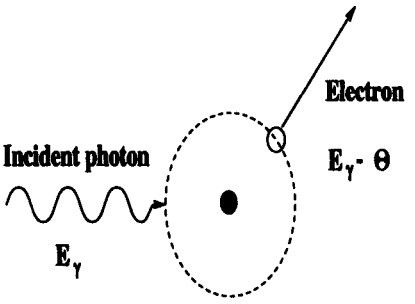

Figure 3.1: Diagram of photoelectric effect

energy less the electron binding energy:

$$E_e = h\nu - E_B \tag{3.1}$$

The photo-electric effect creates an ionized absorber atom in the detector matter with a vacancy in one of its electron shells, which is filled by either a free electron or by the rearrangement of the electrons in the other shells. It is most significant for low energy photons ($E_\gamma \leq 100$ keV). It increases rapidly with the atomic number of the absorber material and decreases rapidly with increasing photon energy.

- Compton Scattering. Compton scattering is the process by which a photon scatters from a nearly free atomic electron, resulting in a less energetic photon and a scattered electron carrying the energy lost by the photon. The energy of the scattered photon has an angular dependence

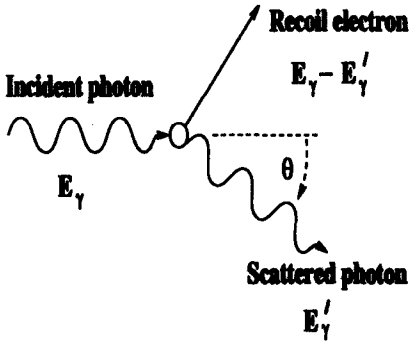

Figure 3.2: Diagram of Compton scattering.

and it can be shown through conservation of energy and momentum that

$$E'_\gamma = \frac{E_\gamma}{1 + \frac{E_\gamma}{m_0 c^2}(1 - \cos\theta)} \tag{3.2}$$

where E_γ and E'_γ are the energies of the incident and scattered photons respectively, θ is the scattering angle of the photon with respect to its initial directions and m_0 is the electron's rest mass. It is important to note the photon does not transfer all its energy and thus multiple interactions are required to obtain the total photon energy. Often this is not possible since the photon scatters out of the detector before all its energy has been absorbed by the detector. Compton scattering is most probable for γ-ray energies in the range 200 - 1000 keV and the range of energy values constituting the Compton continuum is the major source of background events in γ-ray spectra.

- Pair Creation. If the energy of a γ ray is greater than the rest mass of an electron-positron pair (1.022 MeV) then it can undergo pair production

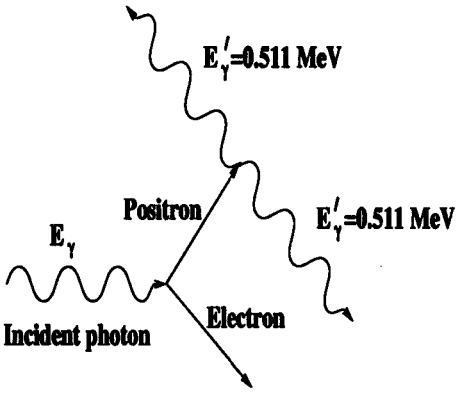

Figure 3.3: Diagram of the pair production mechanism.

(produce an electron-positron pair). The pair production must take place in the Coulomb field of the absorber so as to conserve energy and momentum. Any excess energy is divided between the electron-positron pair as kinetic energy. When the positron has slowed down to the thermal velocity of an atomic electron, it will annihilate with an electron and create a back-to-back γ-ray pair, of 511 keV each. Pair production is significant for energy ranges > 5 MeV.

3.1.2 Germanium Detector Characteristics

- **Absolute Efficiency**

$$\epsilon_{abs} = \frac{N_{det}}{N_{emitted}} \tag{3.3}$$

where N_{det} is the number of events detected, and $N_{emitted}$ is the number of γ rays emitted by the source.

- **Photopeak Efficiency**

A photopeak, can be defined as the full γ-ray energy deposited in the detector. The photoelectric effect is the dominant mode of interaction at low energies i.e $\simeq$ 200 keV and falls off rapidly with increasing energy. As the γ-ray energy increases, the dominant mode of interaction is the Compton effect and pair production.

$$\epsilon_{ph} = \frac{N_{peak}}{\Omega\, N_{emitted}} \tag{3.4}$$

where N_{peak} is the number of γ-rays in the photopeak.

- Relative Efficiency

$$\epsilon_{rel} = \frac{[\epsilon_{ph}\, \Omega]_{detector}}{[\epsilon_{ph}\Omega]_{NaI}} \tag{3.5}$$

where $[\epsilon_{ph}\Omega]_{NaI} = 1.224 \times 10^{-3}$ for a NaI detector of 76 mm long and 76 mm in diameter at a distance of 250 mm from the source when using standard NaI detector for the 1.332 MeV γ ray in ^{60}Co.

- Peak-to-Total Ratio

$$\frac{P}{T} = \frac{N_{peak}}{N_{total}} \tag{3.6}$$

where N_{peak} is the number of recorded events that fall in the peak, and N_{total} is the total number of events recorded. The peak-to-total ratio is a measure of the fraction of total events where the γ ray deposits its full energy in the detector. The ratio of counts for a particular incident γ-ray in its detected photopeak to the total number of counts in the Compton background is energy dependent. This has resulted in a standard being set involving measuring this ratio for a ^{60}Co source with photopeak energies at 1173 keV and 1332 keV.

- Energy Resolution. The energy resolution is a measure of photopeak width which is usually taken at half the maximum value, generally referred to as the Full Width at Half Maximum (FWHM). The Ge detectors

we used have standard measurements using a ^{60}Co source of a FWHM $\approx$ 2.0 keV for the 1173 keV and 1332 keV photopeaks for the CLOVERS.

- Escape Suppression. The peak-to-total ratio described above can be improved if all those events where the γ ray escapes from the detector, after only depositing part of its energy, are rejected. This is done by surrounding the Ge crystals with a shield of scintillator detectors. This shield will then act as a veto on the signal from the Ge crystals. The choice of shield requires a material of high efficiency, and no consideration for the resolution. A scintillator is often used, and the one we used, is bismuth germanate (BGO).

- Doppler Shift. The γ-ray emitted by a recoiling nucleus has an energy:

$$E_\gamma = E_\gamma^0 [1 + \beta \cos\theta] \tag{3.7}$$

to first order, where E_γ^0 is the actual γ-ray energy, E_γ is the observed energy, and θ is the angle between the detector and the recoil velocity vector of the nucleus and is known as the the Doppler shift and is maximal for θ=0 and zero at θ=π/2. When taking into account the solid angle subtended by the detector, the spread in energy of a γ ray entering a detector at the angle θ can be written for small $\Delta\beta$:

$$\Delta E = | E_\gamma(\theta - \Delta\theta) - E_\gamma(\theta + \Delta\theta) | \tag{3.8}$$

$$\Delta E = 2 E_\gamma^0 \beta \sin\theta \Delta\theta \tag{3.9}$$

3.1.3 Multi-Detector Arrays

Multi-detector arrays provide the ideal tool for doing high-spin studies. The angular distribution and coincidence information derived from studies using these arrays is essential in making studies of high-spin states in nuclei. This

is especially evident when studying the more "exotic" features of spinning nuclei such as superdeformation. The development of arrays capable of providing the necessary information for these studies has gone hand in hand with detector, electronic and software development to enable the full utilization of these multi-detector arrays. A single detector used on its own would allow one to list the observed γ-ray energies from all manner of reaction products, but it would be difficult if not impossible to infer anything at all about nuclear states from the data. A minimum of two detectors placed near the target allows one to perform coincidence experiments. Coincident γ rays detected simultaneously in detectors are associated with a particular decay pathway in one of the reaction products, and a level scheme may be constructed on the basis of the observed coincidence and anti-coincidence relationships. From the above statement, it is clear that the chance of intercepting the maximum possible number of γ rays from a given nuclear de-excitation improves as more detectors are used. This led to the development of large escape suppressed spectrometer arrays (ESSA's). GAMMASPHERE [Lee90] is the result of an American collaboration and consists of 110 Compton suppressed high-purity germanium detectors. GAMMASPHERE's capabilities are further enhanced by further auxiliary detectors. EUROGAM [Bec94], was a UK - France collaboration. It consisted of 30 Compton suppressed coaxial germanium detectors and 24 Compton suppressed CLOVER type germanium detectors (like those we used on AFRODITE). The original collaboration has been extended to other European nations. EUROBALL was a European collaboration that brought together detectors from EUROGAM (UK/France) and GaSp (Italy) and Cluster detectors from Germany, Italy, Sweden, Denmark and the UK. EUROBALL was exploited at Legnaro, and was then transferred to the VIVITRON accelerator at IReS (Strasbourg), in France for a second campaign which ended in 2003. EXOGAM [Sim00] is a relatively new γ-ray spectrometer which has the

same geometry as the AFRODITE spectrometer.

3.1.4 The iThemba LABS Facility

A floor-plan of the iThemba LABS facility is shown in Fig. 3.4. The features relevant to the present work are the electron cyclotron resonance (ECR) ion source, the two solid pole injector cyclotrons SPC1 and SPC2, the large k = 200 separated sector cyclotron (SSC). The AFRODITE spectrometer array is located on beam line F. A wide range of heavy ion beams have been produced at iThemba LABS ranging from ^{1}H to ^{136}Xe at various beam energies. The maximum beam energy attained was for ^{136}Xe at 750 MeV. To produce ion beams, the vapour from the element is extracted from a micro furnace and then stripped of orbital electrons in the ECR ion source. The plasma is then accelerated from the source using an electrostatic lens, and ions of the correct charge state are selected for injection into the k = 10 SPC2. The beam is extracted from the injector cyclotron and then further accelerated in the SSC until the beam particles attain the kinetic energy required for the experiment. From the SSC, the ions are guided to the experimental vault via the high energy beam line using quadrupole magnets for focusing and dipoles for bending the beam. The SSC delivers a pulsed beam with repetition rate from 8 to 26 MHz. The SPC1 is used to accelerate light ions (p,d,α), while the SPC2 is used to accelerate heavy ions, polarized protons and deuterons.

3.1.4.1 AFRODITE

AFRODITE (African Omnipurpose Detector for Innovative Techniques and Experiments) is a γ-spectroscopy detector array at the separated sector cyclotron facility at the iThemba LABS, Faure, South Africa. AFRODITE consisted of 8 CLOVER type intrinsic germanium detectors with BGO escape-suppression

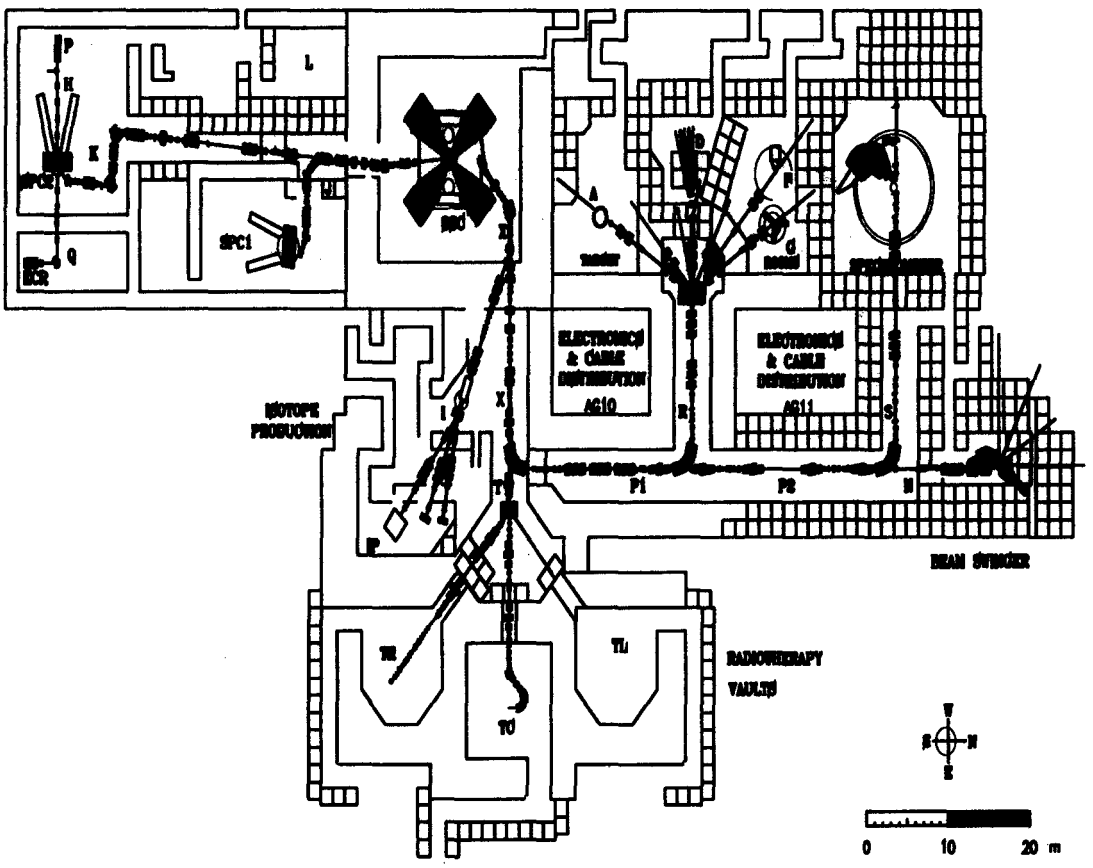

Figure 3.4: Diagram of the iThemba LABS facilities.

shields for this experiment. The AFRODITE frame that holds the detectors is a rhombicuboctahedron in shape with 16 detector positions [New98]. The 8 CLOVER detectors subtend 11% of the 4π solid angle. Each CLOVER consists of four rectangular n-type germanium, 50 x 70 mm, crystals. The crystals are mounted together on a single cryostat.The shape of the rhombicuboctahedron allows four detectors at a forward angle of 45° four at a backward angle of 135° and 8 perpendicular to the beam. The sensitivity and energy resolution in the low energy regime (approximately 100 keV), was enhanced by the inclusion of up to 8 low energy photon spectrometers (LEPS). In AFRODITE the LEPS detectors are cheaper than the BGO-suppressed CLOVERS, and they are ideal for detecting characteristic X-rays and this could afford the possibility of good Z-selectivity, particularly for heavy nuclei where electron conversion becomes important. The position of the detectors was the following: 2 CLOVER and 2 LEPS detectors were at an angle of 135° to the beam axis, 3 CLOVER and 4 LEPS detectors were at 90° to the beam axis and 2 CLOVER and 2 LEPS detectors were at 45° to the beam axis.

3.1.5 Detectors

The CLOVERS [Jon95], [Bea96], [Duc99], [She99], comprising four n-type coaxial HPGe crystals housed in a common cryostat and BGO suppressor, are identical in design to those first used in the EUROGAM II array. Fig. 3.5 illustrates the arrangement of the four CLOVER elements. CLOVER performance has been detailed in many theses but some features are discussed below. Each crystal element has its pre-amplifier, which allows energies deposited in more than one element of a detector due Compton scattering to be added. An energy dependent add-back factor of up to 1.5 has been reported [Bea96]. With scattered events included, the relative efficiency for the Clover detectors is on average

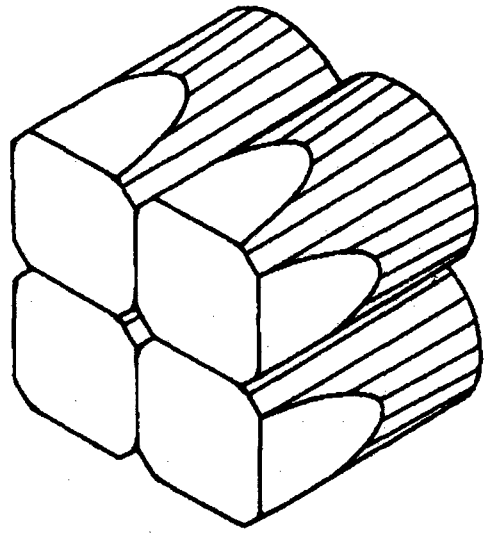

Figure 3.5: Geometrical arrangement of HPGe crystals in a CLOVER detector.

140%, comparing favourably with a relative efficiency of approximately 80% for the large single-crystal Ge detectors [New98] present in both EUROBALL III and GAMMASPHERE. Each BGO Compton suppression shield consists of 8 optically separated segments, each of which has in turn 2 PM tubes. All 16 PM tubes for a given shield are then connected in series. The BGO signal from a Compton-scattered event vetoes the associated CLOVER. LEPS are planar (10 mm thick, 60 mm diameter) detectors made from a single crystal of p-type HPGe electrically segmented into four quadrants. The signal from each quadrant is processed separately, as in the case of the CLOVERS. One consequence of the planar geometry is that LEPS efficiency falls off much faster with increasing energy than that of CLOVERS, and that is negligible above 400 keV (Fig. 4.3). Since low energy photons are less likely to Compton scatter out of the crystal, LEPS are thus neither BGO-suppressed nor operated with addback.

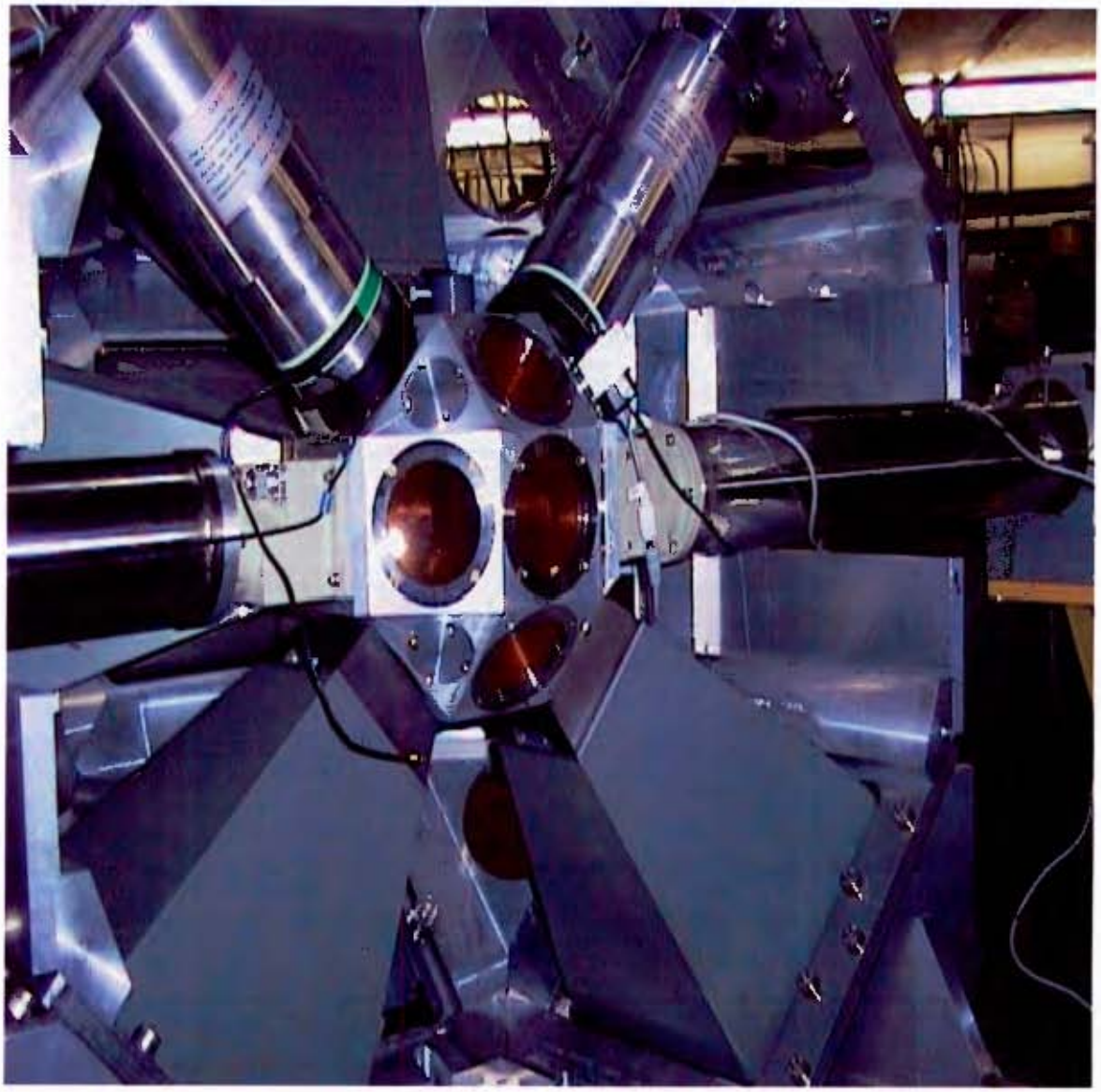

Figure 3.6: Photograph of the AFRODITE γ-ray spectrometer at iThemba LABS.

3.1.6 Semi-Conductor Detectors

Semiconductors have an energy gap of ~1 eV whereas insulators have one of 5 eV or more. The energy gap is the gap between the valence and conduction bands in the material. At room temperatures very small numbers of the electrons in a semiconductor may be thermally excited across the energy gap into the conduction band, as one electron is excited another takes its place and it appears as if the "hole" migrates through the material. The movement of charges in a semiconductor may be controlled by introducing very small amounts of impurities, or dopants, into the material to create an excess or lack of electrons thereby creating n or p type semiconductors respectively.

When n and p type semiconductors are put against each other a depletion region is formed where the excess electrons cancel the holes. The depletion region's size is limited by the electric field created in the wake of the electrons and holes canceling each other causing a change in the charge states of the two semiconductors. Radiation entering the depletion region results in ionization or creation of electron-hole pairs which in turn causes an electron flow. Since the ionization energy is independent of the radiation energy the electron flow/pulse amplitude is proportional to the energy of the radiation.

Usually a large reverse bias voltage ($\geq$ 1 kV) is also applied to the semiconductor detector so as to increase the size of the depletion region and to increase the electric field in this region thereby increasing the sensitive volume of the detector and improving the charge collection. Semiconductors also need to be kept at low temperatures (usually liquid nitrogen temperature of 77 K) so as to minimize thermal excitation of the electrons.

The most common semiconductor detectors are made from silicon or germanium covered in a small concentration of lithium. The lithium drifts into the germanium or silicon and forms a depletion region. This type of detec-

tor needs to be kept at low temperatures at all times or else the detector will be destroyed as the lithium migrates out of its lattice sites. This clearly is a big disadvantage in using this type of detector, but is often outweighed by the superior energy resolution provided.

Hyperpure Germanium Detectors It is now possible to produce large crystals of germanium with extremely low impurity concentrations. The advantage of this is that their purity and quality is not temperature dependent like the lithium drifted germanium and silicon detectors. They still have to be operated at liquid nitrogen temperatures so as to prevent thermal excitation across a relatively small band gap of 0.67keV. Also since large volume detectors can be produced, this improves the capability of detecting the higher energy γ rays which penetrate deeply into materials. Because of all these advantages hyperpure germanium detectors have now become the detector type of choice in the large detector arrays used in gamma-ray spectroscopy.

3.1.6.1 Frame, Target Chamber and Target Ladder

The aluminium frame supporting the detectors may be retracted from the beam line to allow access to the target chamber. This is illustrated in Fig. 3.7. The target chamber allows a direct view of the target ladder through 25 micron kapton windows, which are flexible and transparent to γ rays. The three frames of the target ladder usually support an aluminium oxide beam position monitor (top) and the target foil (bottom). There is also the middle frame which is empty for checking beam halo.

3.1.7 Electronics and Data Acquisition System

AFRODITE requires electronic instrumentation for up to 64 signals from the germanium detectors. Standard NIM (nuclear instrumentation method) and

CAMAC (computer automated measurement and control) modules are used for the signal processing. These are located in the experimental vault. The data acquisition system is directed from the data-taking room, via a workstation running the VMS operating system and the XSYS data acquisition package which is a general purpose data acquisition system [Pil92]. One of the functions of XSYS is to increment on-line spectra for real time viewing from the control workstation. Signals from various points in the signal processing chain are patched through to the data room to allow the possibility of remote inspection and the monitoring of event rates. The essential electronics for processing the signals from the CLOVERS and LEPS are shown in Fig. 3.8. The circuit can be subdivided into an energy and a timing circuit. As far as the energy circuit is concerned, the first element of the signal processing chain is the preamplifier housed in the detector cryostat. The pre-amplifier output pulse approximately 100 mV/MeV with a decay time of 50 μs, whose area is proportional to the gamma energy deposited, goes through the spectroscopy amplifier. The pulse is then integrated and shaped (3 μs shaping time), giving a linear energy pulse ranging from 0 to 10 V whose height is proportional to the gamma energy. There is also a fast timing signal from a timing filter amplifier fed to a CFD (constant fraction discriminator) where the pulse is converted to a logic pulse required by the timing circuit. The linear pulse is then sent directly to a 12-bit ADC (analog-to-digital converter) (4096 channels) where it is digitized. The ADC gate pulse controls whether or not a signal is digitized. The ADC gate is open for user-defined valid events or closed otherwise. The valid event condition is set up in the timing circuit.

The timing circuit establishes all the coincidence relationships between signals from different hardware components for both experiments. It defines the event trigger used to filter out unwanted events, and controls the ADC gate, the TDC (time-to-digital converter) start and stop signals and the BGO veto. It

links the the detector elements, bit pattern registers, and CAMAC controller. The CLOVER and LEPS signals are processed in the same way, except for the BGO veto needed from the CLOVERS. A single BGO signal from the 16 series-connected PM's (photomultiplier tubes) surrounding a CLOVER is used to veto the combined 4 elements of the associated CLOVER. After passing through a TFA (timing filter amplifier) the BGO pulse is fed to a CFD. Any BGO signal exceeding the threshold (typically 40 keV) is converted to a logic pulse (width of 150 ns) which may veto the clover signal. After amplification the CLOVER signals are fed to a CFD where each channel is split in two. The first branch goes to a bit pattern register while the second is bunched in groups of four (logical OR) giving one output channel per CLOVER. At this stage the CLOVER signal may be vetoed. Appropriate delays are introduced to ensure that BGO and CLOVER signals from the same event are always in coincidence. The bit pattern register provides a record of which elements fired. CLOVER signals which are not vetoed may now be used to generate the event trigger, ADC gate, and TDC start and stop signals. The signals are fed to the MLU (majority logic unit), which is a coincidence unit accepting all signals from all the detectors. CLOVER and LEPS signals are 50 ns wide giving a coincidence overlap time of 100 ns. The MLU generates the event trigger by requiring that an event of minimum fold f be present. In the present work, for both experiments $f = 3$, meaning that MLU only has output when at least 3 detectors (2 CLOVERS and 1 LEPS have fired or 3 CLOVERS). The simultaneous firing of any 2 CLOVERS and 1 LEPS thus constitute a valid event. The event trigger in turn is used to generate the ADC gate, the strobe for the bit pattern register, and the common start for all TDC channels. The presence of a valid event satisfies the ADC gate condition, but the TDC's start require a coincidence between the event trigger and the first RF signal from the beam to arrive at the TDC (range 200 ns) after the TDC start pulse. The stop pulses are generated by individual de-

tectors, and correspond to the first detector element to fire in the valid event. A suitable delay is needed in order to digitize the signal. The ADC and TDC are then read by the FERA (Fera bus, a trademark of Le Croy) which stands for a Fast Encoding and Readout ADC module. During readout, the event trigger sends a busy signal to the MLU, preventing the recording of any further valid events for the duration of the signal in order to prevent pile-up at the ADC. The resulting dead-time depends on the ADC conversion time as well as on the number of data words written per valid event, and this is the main bottleneck in limiting the maximum achievable event rate. In these experiments, the ADC's were read out by a front panel ECL data bus and transfered to a Le Croy VME-based fast memory unit. The maximum event rate was about 2 kHz with the FERA readout, at about 30% dead-time. The data acquisition front-end module builds event buffers sent via the ethernet to the control workstation. An XSYS event-analysis task performs on-line sorting of the received buffers and stores the raw event buffers on tape. Each event is written as a group and contains energy and time information for each coincident γ ray, and bit patterns recording which detector elements fired.

3.1.8 Data Sorting and Manipulation

Due to the large quantity of data available in modern γ-ray spectroscopy, specific techniques and software have been developed to make the job of analyzing the data much simpler and quicker. This section will discuss and explain a few of the basic data sorting and manipulation software packages in modern γ-ray spectroscopy [Rou01].

3.1.9 Gamma-Gamma Coincidence Matrices

The data acquired is usually filtered with a coincidence criterion such that an event is only valid if two or more γ rays are detected by the array. The coincidence relation between the γ rays is of importance in analysis as we wish to build up a level scheme for the decaying nucleus and as such need to know the pattern of the γ rays emitted as the nucleus de-excites. A simple way of collating this coincidence information is by constructing a symmetric γ-energy vs. γ-energy matrix. For such a $\gamma - \gamma$ energy matrix a single row or column provides a spectrum of γ-ray energies that were coincident with the chosen row or column's associated γ-ray energy. A sum of all the rows or columns, referred to as an x or y projection respectively, results in a spectrum of all the γ rays detected by the array that have passed the coincidence criterion.

3.1.10 RADWARE

RADWARE [Rad95] is the name of a suite of programs, written by David Radford, designed specifically to manipulate and perform analysis of $\gamma - \gamma$ matrices (square, cube, and hypercube). However in this thesis only square matrices (2-fold coincidence) are used.

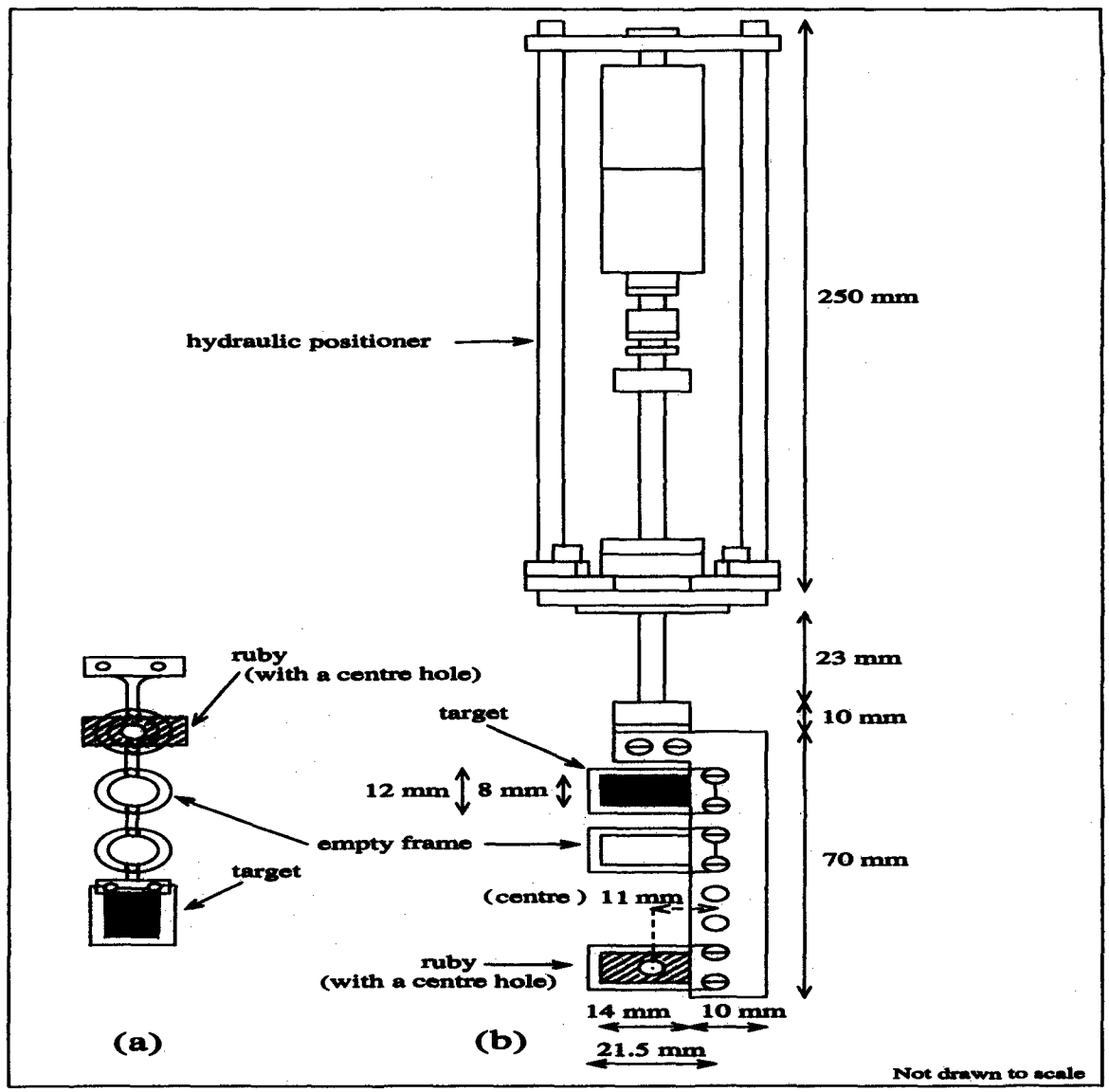

Figure 3.7: A diagram of the target ladder.

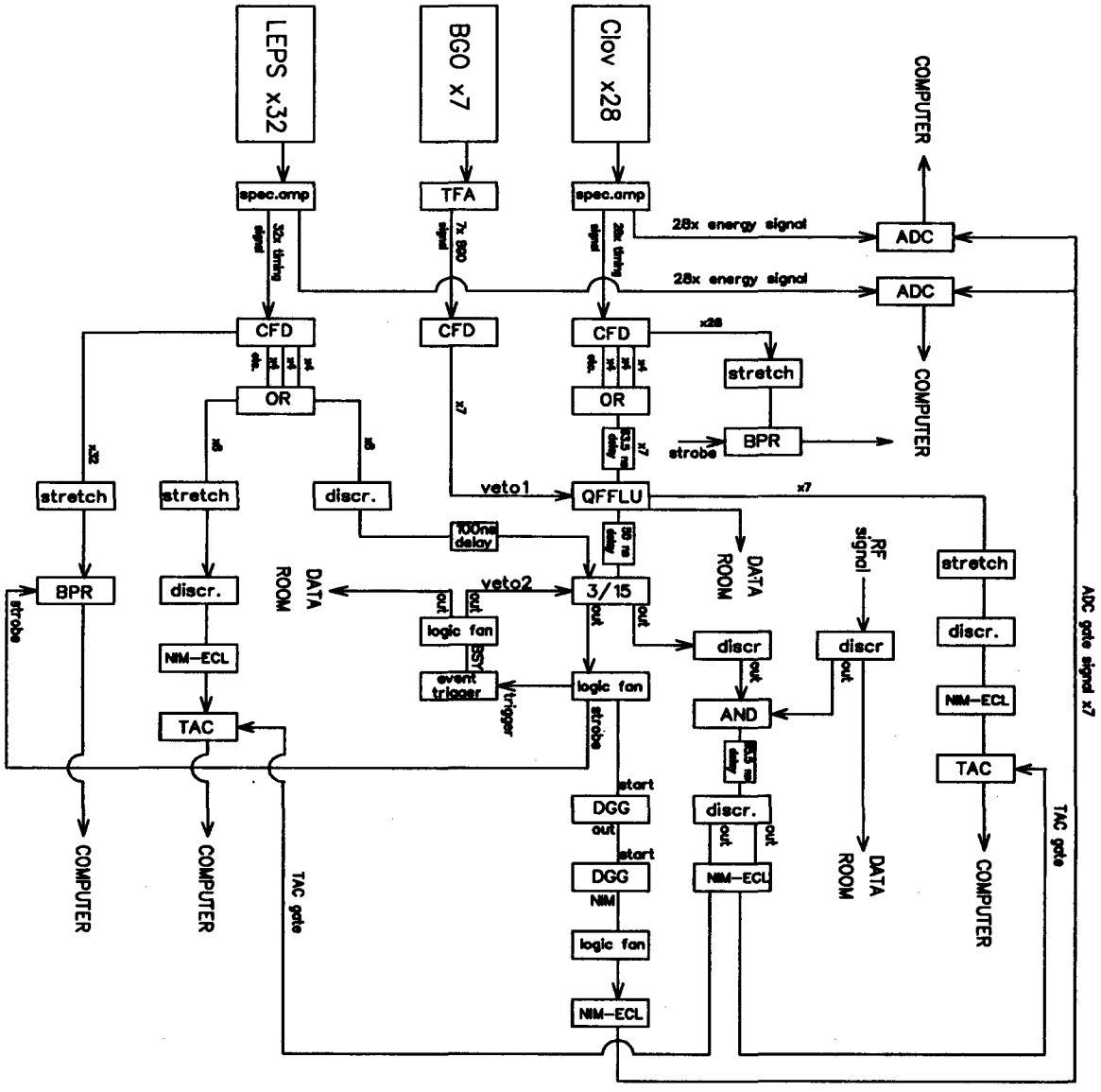

Figure 3.8: Diagram of the electronics for the experimental arrangement of the AFRODITE spectrometer.

Chapter 4

DATA ANALYSIS AND EXPERIMENTAL RESULTS

The data presented in this work were taken in two independent experiments involving transfer reactions, using the AFRODITE array to measure γ-γ coincidences. The heavy ion beams were provided by the k = 200 separated sector cyclotron facility of iThemba Laboratories for Accelerator Based Sciences. From the previous fusion-evaporation reactions studied at iThemba LABS, the codes EVAPOR or PACE2 [Gav80, Gav93] are used to calculate cross sections in order to study various reaction channels. However these codes are important in calculating fusion evaporation which is not what is being studied here. GRAZING calculates transfers as a binary-reaction process and, therefore, can yield relative cross sections as required by this experiment. In the case of the present reactions the products of the charges of the beam and target were too high and the codes could not be used. Thick targets were used: a 35 mg cm^{-2} Au and a 40 mg cm^{-2} Pt so that all the reaction products are stopped in the target and we do not have to apply Doppler shift correction to the emitted γ rays. The γ rays that are studied are emitted after the nuclei stop. The choice of the target thickness was determined by the ELOSS program which calculates the energy deposited in the target per unit length. Prior to the experiments, two codes were used to determine the relative cross sections of various reaction channels, namely the EVAPOR code and PACE2 calculations. The codes were inadequate for such calculations, hence the choice of the GRAZING program as it calculates relative cross-sections irrespective of the mass number of the target and projectile. The terms projectile-like and target-like fragments will

be used throughout this chapter, but it is more correct to use the term complementary fragment to the target-like nucleus under discussion. The sum of the Z and N of the complementary fragments must add up to what one had in the entrance channel. Throughout these experiments, having thick targets, it was assumed that the stopping times are very short and no angular dependent corrections were made. Once the possible fragments and their excitation energies are calculated, evaporation-model codes could be applied to the fragments to see if neutrons will be lost in the final channel. However no codes for neutron evaporation have been used.

4.1 Data Acquisition

The first experiment was performed over 2 weekends during November and December 1999, using the AFRODITE detector array with seven CLOVERS and eight LEPS. Unlike experiments where Doppler shift corrections and Directional Correlation from Orientated nuclear states (DCO) analysis have to be performed, in this case, the detector geometry is not so important as all the reaction products are stopped in the target. The first experiment used the ^{197}Au target. The second experiment was performed over three weekends between December 2000 and January 2001 using the ^{194}Pt target. The preparation for an experiment starts usually the week preceding the scheduled beam time. All the detector modules are correctly biased at least 48 hours before the start of the session to ensure performance stability. Prior to each session, a rough calibration of all the detector elements is performed. The amplifier gain for the CLOVER elements is adjusted to approximately 0.5 keV/channel to provide a 2 MeV range for each 4096 channel ADC, and the LEPS dispersion is adjusted to 0.2 keV/channel corresponding to a range of 0.8 MeV. All CFD lower thresholds are checked and and set to about 30 keV using a ^{133}Ba source. The pole zero and integrating time constant for each amplifier channel are set, and remain fixed during the experiment. Finally, energy and efficiency calibration of all channels was undertaken in singles mode (coincidence level = 1), using standard ^{133}Ba and ^{152}Eu sources which are placed at the target position. This is repeated immediately after the acquisition is terminated at the end of each weekend. These calibrations provide a record of the performance of individual detector elements at the start and end of the weekends for checking amplifier gains. Typical ^{152}Eu and ^{133}Ba source curves detected in a single CLOVER element are shown in Figs. 4.1 and 4.2. The faint curves represent the difference between the calculated energy and the actual energy. This difference is very

small, hence for the purpose of display, that difference is multiplied by a five hundred and an offset of 500 is increased on the y-axis. The general formula is given by $(y - y_{fit})500 + 500$ for the residual. The ^{127}I beam was extracted from the ECR ion source and fed to the SSC. The SSC delivered a pulsed beam with an energy of approximately 730 MeV and 66 ns between beam pulses. With the target mounted, and the beam line under vacuum, the alignment of beam and target was checked by reducing the beam current to approximately 2 nA and using closed circuit television to monitor the beam spot on an aluminium oxide viewer. This viewer has a 3 mm diameter hole at its centre. When well aligned, the beam passes through this hole with no afterglow. Beam halo is reduced by tuning the beam in order to minimize the CLOVER count rate when using an empty target frame. When the AFRODITE array is ready, the coincidence level on the MLU is set on 3, and the beam is guided onto the target. Before the raw experimental data can be transformed into meaningful results, they must be sorted into appropriate data structures. These may in principle be multi-dimensional, and should present the data in a manageable form for the analysis. Since γ-ray energies are written on tape as raw pulse height, they must be accurately be calibrated and gain matched before data sorting can proceed. In some other cases the raw data must also be Doppler corrected, but this does not apply to the present work as very thick targets are used.

4.1.1 Energy Calibration and Efficiency of the Detectors

The first step in processing the data is to obtain a reliable set of calibration coefficients for all detectors, for each weekend. Standard ^{133}Ba and ^{152}Eu sources are placed at the target position in order to reproduce in-beam detector-target distances, and data are taken in singles mode [Rou01]. AUTOCAL [Law97], an automated peak-fitting routine on the VAX cluster is used to determine cen-

troids of the photopeaks of the calibration spectra. For the first experiment, the Ge detector elements are calibrated using the expressions:

$$E_\gamma = bx + c + d/x \tag{4.1}$$

It produces a better fit a lower energies. And

$$E_\gamma = ax + c \tag{4.2}$$

for the second experiment. Typical calibration curves are shown in Figs. 4.1 and 4.2 for both the CLOVERS and the LEPS detectors for the second experiment. The efficiency calibration measurements for the AFRODITE (LEPS and CLOVER) detectors were performed at the end of each experiment with the ^{152}Eu and ^{133}Ba radioactive sources. These sources were mounted on the target ladder. The trigger logic adopted for these calibration measurements was one out of fifteen detectors [Mab03] for calibration purposes. Separate relative efficiency (ϵ) curves for the 8 LEPS and 7 CLOVER detectors are illustrated in Fig. 4.3. The curves were constructed from the summed singles data for the two types of detectors using RADWARE program EFFIT [Rad95]. The energy calibration parameters necessary to be used in RADWARE program ESCL8R [Rad95a] were also generated from the source data with ENCAL program [Rad95]. The efficiency of the LEPS and clovers detectors dropped below 40 keV and 110 keV for LEPS and CLOVER detectors respectively, due to absorption and CFD thresholds. The maximum detection efficiency occurs at 40 keV and 110 keV for the LEPS and CLOVERS detectors respectively, and decreased smoothly as the energy increased. This common feature in both types of detectors is caused by the decrease in photoelectric effect and Compton scattering cross-sections with increasing energy of the γ rays. The calculated energy and efficiency calibration parameters were fed into the ESCL8R program which was used to extract for γ-γ coincidence intensities. These in-

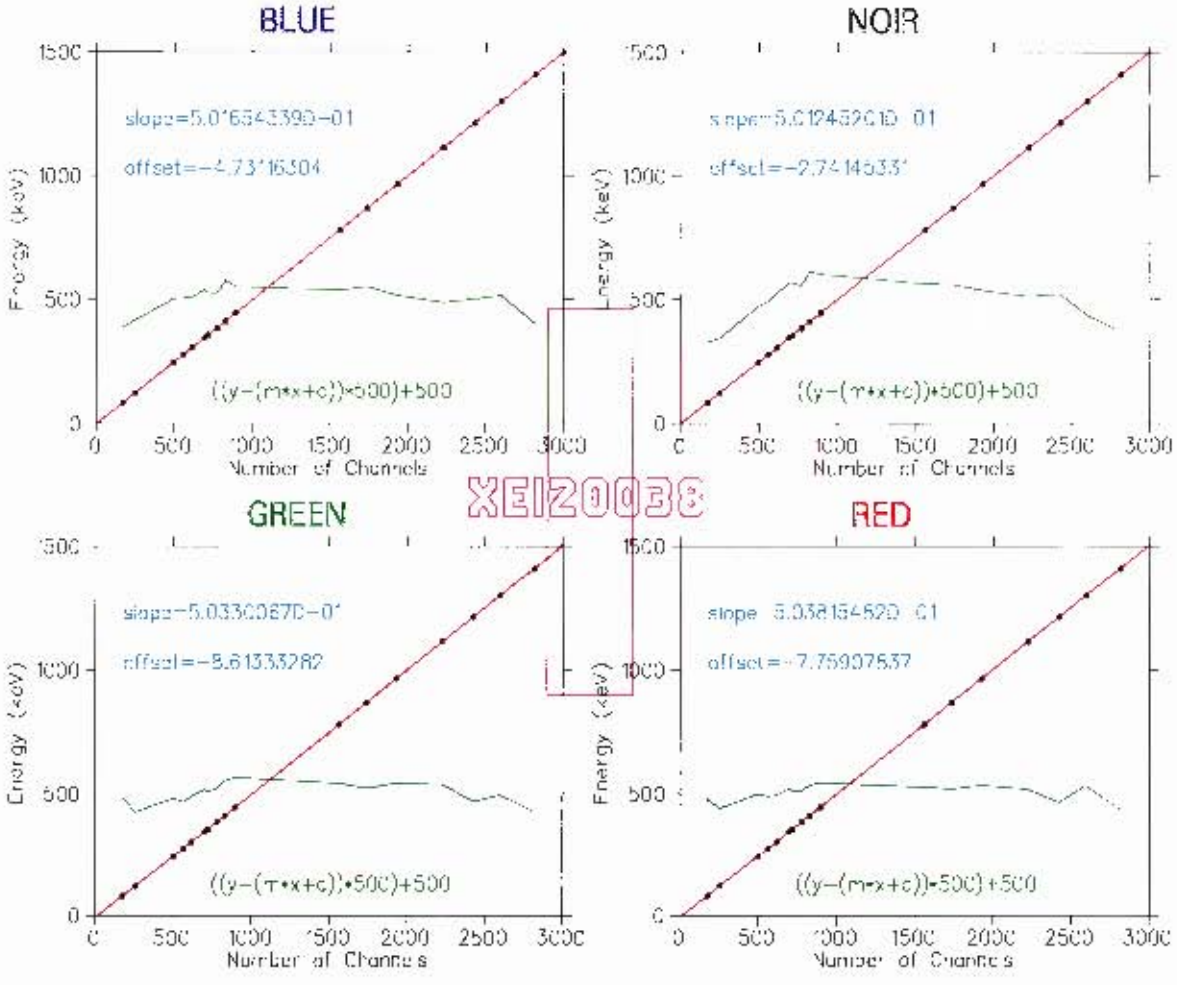

Figure 4.1: Typical calibration curve for a CLOVER. The green curves represent the difference between the actual value and the fitted value multiplied by 500 and + 500 for the offset.

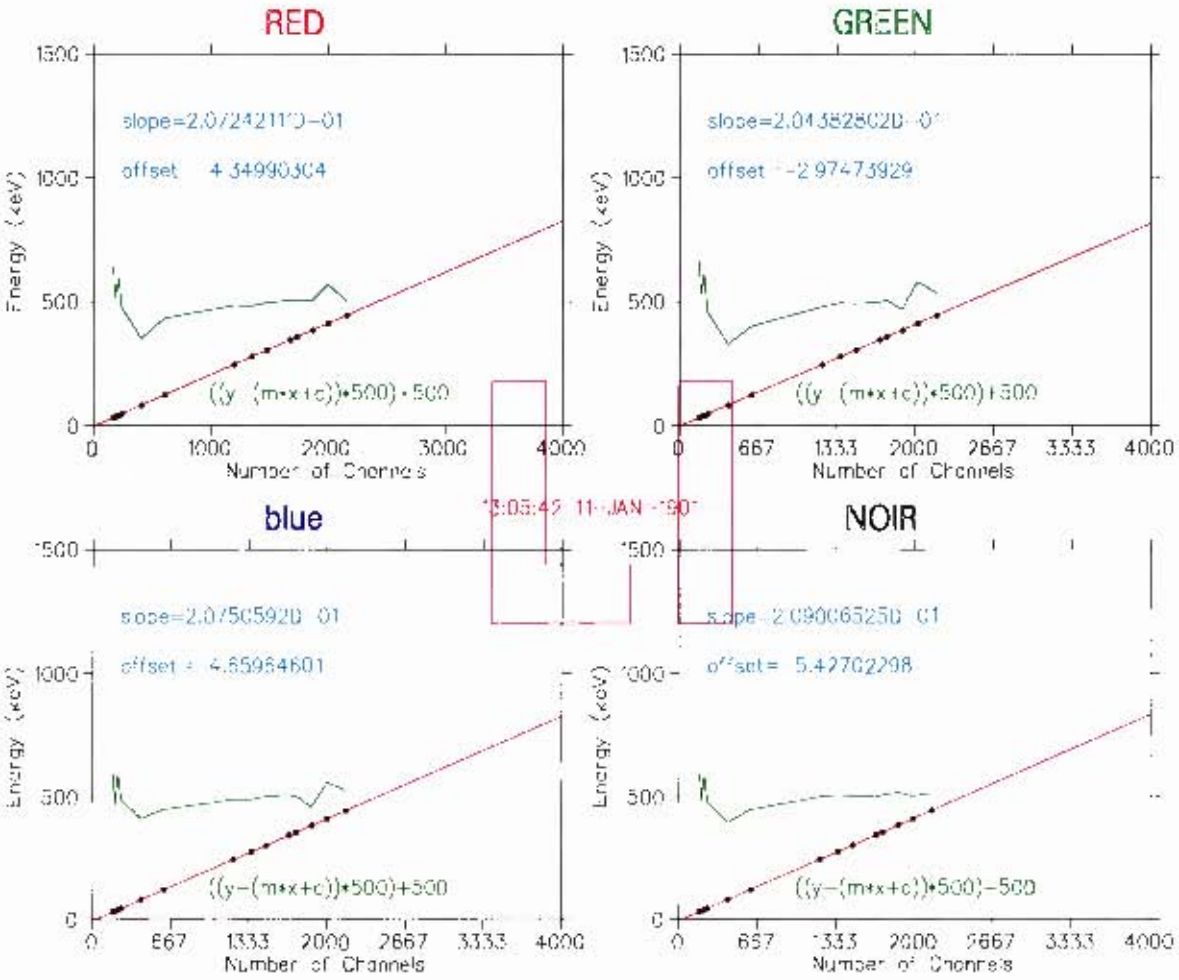

Figure 4.2: Typical calibration curve for a LEPS. The green curves represent the difference between the actual value and the fitted value multiplied by 500 and + 500 for the offset

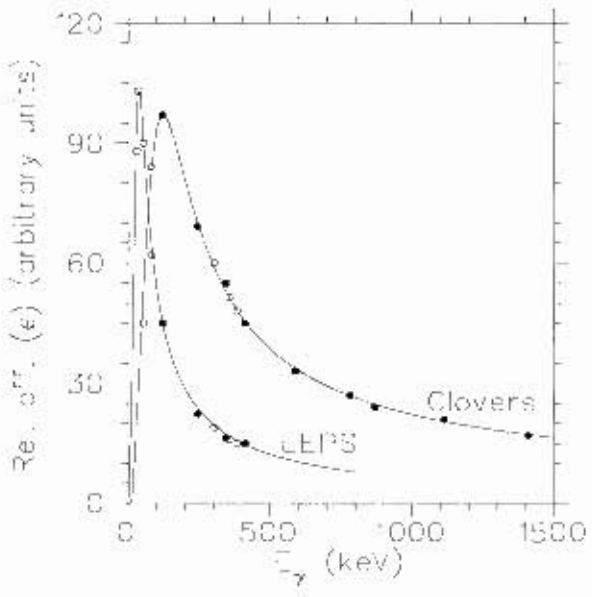

Figure 4.3: Relative efficiency curves for the LEPS and CLOVER detectors measured with the ^{152}Eu (filled circles) and ^{133}Ba (open circles).

tensities were used to determine the relative strength with which nuclei were populated.

4.1.1.1 Level Scheme Construction

The total projection of a matrix is formed by projecting out all of the events onto one energy axis. The projections of the matrices are shown in Figs. 4.4 and 4.5. For the present work, only CLOVER-CLOVER matrices were constructed for both experiments, as the LEPS detectors did not offer much information besides identifying some X-rays. A gate can then be set on a particular photopeak using channel numbers determined from the total projection spectrum to produce a coincidence spectrum of all the γ rays associated with that particular photopeak [Hib93]. The matrix for the first experiment was constructed by Kwinana for his MSc thesis [Kwi01] and the author. The XSYS program was used for the construction of such a matrix. The results proved to be good,

but during the first weekend the data were completely contaminated by the beam hitting the aluminium target frame as well as the target. During the second weekend of the first experiment, the data were also contaminated, but we could retrieve a lot of useful information. The use of the XSYS program proved to be reliable, but too slow, as we first had to adjust the gains manually, before constructing the matrix. The matrix for the second experiment was used using a much faster program from Liverpool University, namely the MT-sort program,[NSP], which adjusts the gains, and builds the matrix in a matter of hours instead of months as was the case with the first experiment. There were not sufficient triples for a more accurate cube analysis . Upon analysis of the data, the first surprising fact was that any gated photopeak would be in coincidence with the target and beam ground state peaks. The reason for this phenomenon is the following.

- there could be two separate γ rays with the same energies, which is rather rare.

- more likely, it could be due to a couple of peaks, e.g the $2^+ \rightarrow 0^+$ and even the $4^+ \rightarrow 2^+$ in the target nucleus being so strongly populated that it comes through as a random peak. Since the Coulomb excitation is by far the strongest interaction (much more likely than deep-inelastic collisions), this 'random' is usually there in most of the gates, unless one does some sort of subtraction. The main problem being that the background subtraction relies on the subtraction of two large numbers (counts in the strongest peaks) to obtain a small number (i.e. close to zero if the background subtraction is done correctly). Statistically, this means that one often gets this random or randoms. One way of eliminating some of these randoms would have been to apply TDC or TAC conditions on the $\gamma - \gamma$ coincidence matrices used for the analyses, but in the early days of

AFRODITE, no timing information could be measured. This also explains the large number of 'contaminant' lines from the beam and target nuclei in the subsequent spectra presented in this chapter.

One of the most important aspects of this thesis is to construct level schemes after having identified which nuclei have been produced in the reactions. The construction of a level scheme can be complicated and is well explained in Hibbert's thesis [Hib93] and his text is reproduced in the next few lines for thoroughness. The total projection of a matrix is formed by projecting out all of the events onto one energy axis. Such projections for the matrices associated with our reactions are shown in Figs. 4.4 and 4.5 and consist of 2×10^6 events for the ^{197}Au + ^{127}I and 1.5×10^9 events for the ^{194}Pt + ^{127}I reactions. A spectrum gated on a particular photopeak will also contain events which are in coincidence with the background that the photopeak sits upon. The background consists of unsuppressed Compton events from the discrete and continuum γ rays, as well as random coincidences. A number of background regions, usually two, close to and on either side of the photopeak are then used to produce a spectrum with an area normalized (the number of counts in the background spectrum is normalized to the number of counts in the background region under the photopeak) to the background fraction in the gated spectrum. This spectrum is then subtracted from the gated spectrum to produce the coincidence spectrum for a given photopeak in the total projection. Negative spikes in the coincidence spectrum occur often and indicate the presence of a fairly strong photopeak in one of the background regions. One can eliminate those negative spikes by choosing a different background region. As an example of how the level scheme for a given nucleus can be constructed, consider the level scheme of Fig. 4.6. Five transitions are shown in the ground-state band or yrast band (from the Swedish word meaning dizzy; thus the yrast level is the dizziest. An

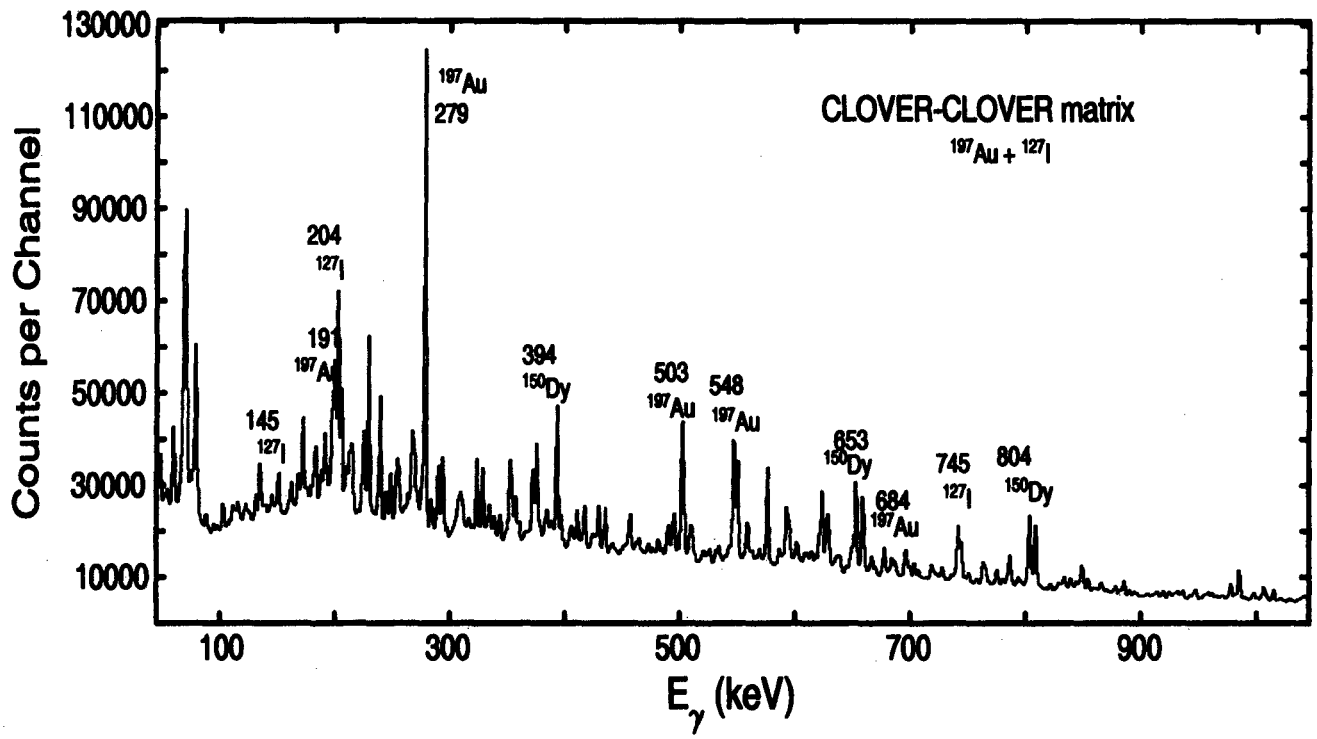

Figure 4.4: Total projection of the CLOVER-CLOVER matrix for the ^{197}Au + ^{127}I reaction.

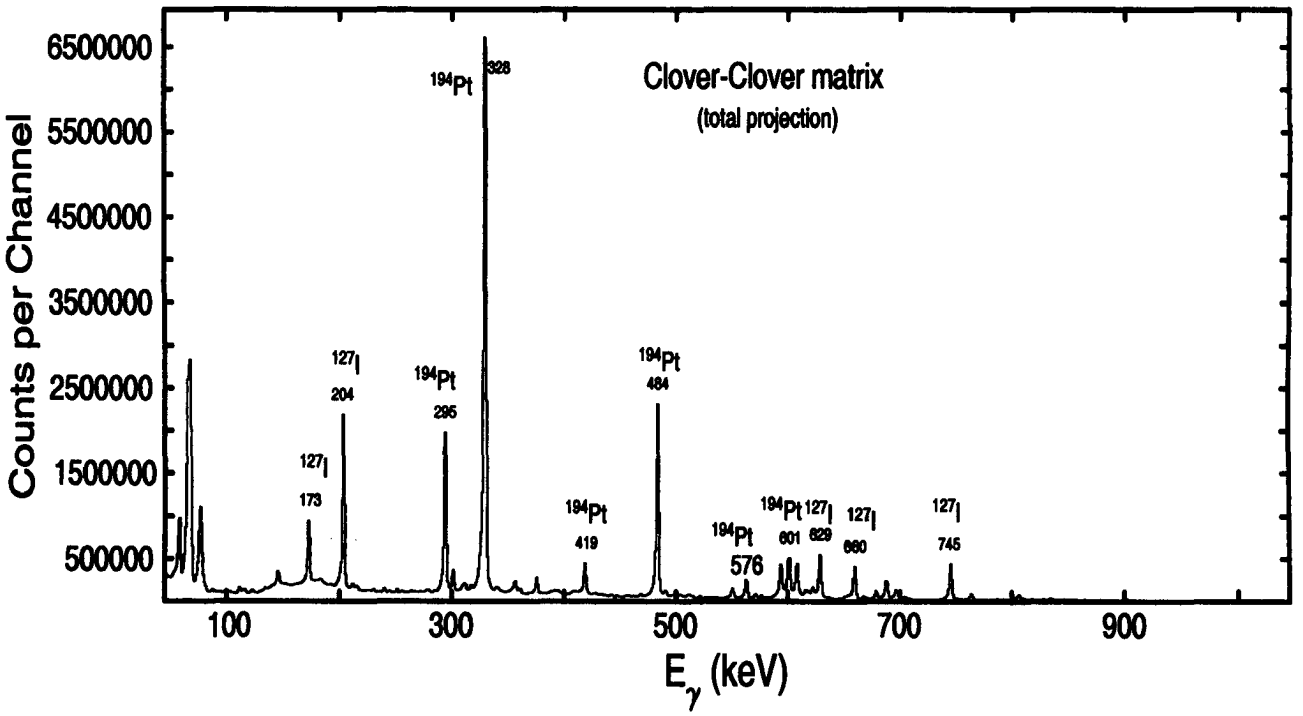

Figure 4.5: Total projection of the CLOVER-CLOVER matrix for the ^{194}Pt + ^{127}I reaction.

Yrast level means the lowest energy for that value of angular momentum (Y1 to Y5) and three in a side-band (S1 to S3) which is linked to the yrast band via connecting cross-band transitions (C1 to C3). The diagrams of Fig. 4.7 show the intensities of the γ rays produced when a particular transition in the level scheme is gated upon. Fig. 4.7 corresponds to the total projection, all of the intensity for each transition is shown. The intensity increases down the band as a natural consequence of the feeding mechanism. In practice it is necessary to place gates on the total projection as weaker transitions will often be dominated by stronger transitions from other nuclei which have similar energies. The spectrum produced by gating upon the lowest transition in the yrast band (Y1) is shown in Fig. 4.7. There is no photopeak at the energy of the transition being gated upon as the γ ray cannot be in coincidence with itself (be measured in two detectors at the same time): the presence of a photopeak would signify that another different transition within the nucleus has the same γ-ray energy. For these points just mentioned, we did in fact encounter such problems and the explanations are given above. A gate upon the transition transition Y3 would result in the coincidence spectrum shown in Fig. 4.7. The intensities of higher transitions are in the same proportion as the total projection. Lower transitions (in this case Y1 and Y2) are equal in intensity of the gated transition in the total projection. The side feeding into these levels cannot be in coincidence, it is therefore not observed. The transitions S1 and C1 cannot occur in the same decay as Y3 and so cannot be in coincidence. Fig. 4.7 shows the spectrum of γ rays in coincidence with the side-band transition S1. Through the coincidence requirements the decay path has been restricted to transitions S3, S2, S1, C1, Y2 and Y1. No other γ rays can be seen. Y1, Y2 and C1 can only be observed with S1 and so they are all equal in intensity, the intensity being determined by that of S1 in the total projection. Finally the spectrum of γ rays coincident with the connecting transition C3 is shown in Fig. 4.6, with Y1, Y2,

Y4 being equal in intensity, and the only other γ ray observed in coincidence is S3. In this simplified case, it has been necessary to ignore the energy efficiency of the germanium detectors.

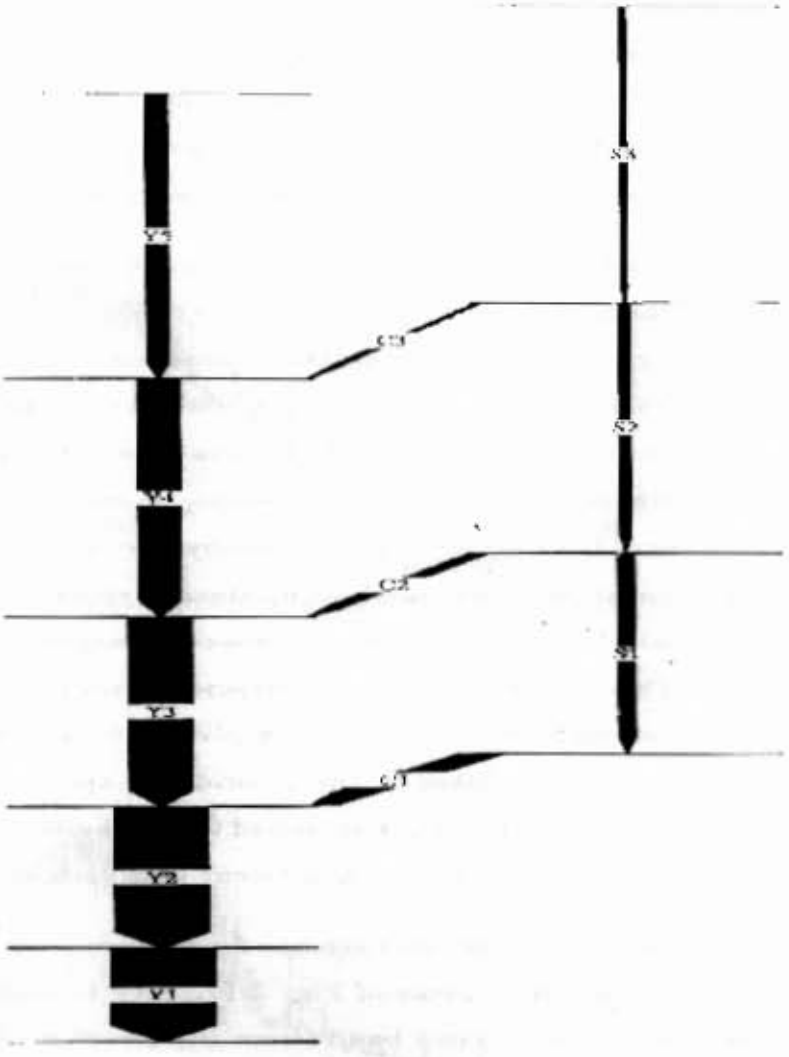

Figure 4.6: A hypothetical level scheme showing yrast (Y), side-band (S) and connecting (C) transitions [Hib93].

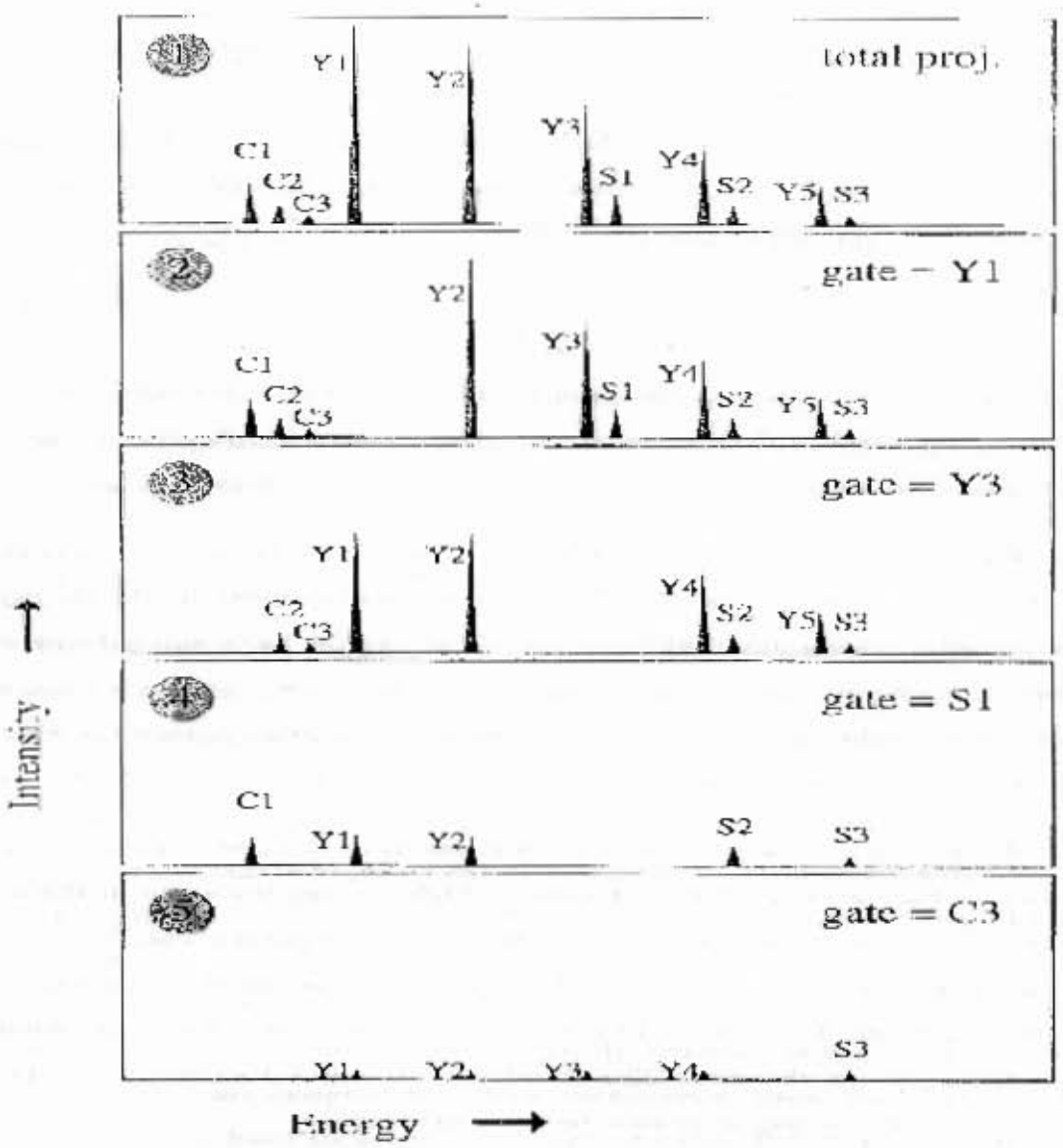

Figure 4.7: Spectra resulting from gates upon transitions in the previous figure [Hib93].

4.2 Results

Spectra from both experiments contain γ transitions between known levels in nuclei.These are shown in the appendices.

4.2.1 The $^{197}Au + ^{127}I$ Reaction

Some of the reaction products seen from the first experiments are shown in Table 4.1. In most instances for both experiments, the majority of the observed nuclei are the target-like fragments. Regan et al. have shown that it was possible to populate up to 10 isotopes of a single element associated with one complementary fragment in heavy ion reactions [Reg04]. Low-lying isomers in beam-like fragments made identification difficult as no timing information for these experiments were available. The spectra corresponding to the observed nuclei for the first experiment are illustrated in Fig. 4.10 to Fig. 4.16 and for the second experiment in Fig. 4.19 to Fig. 4.31 For the first experiment, only the second weekend data were analyzed. In the preceding section on level scheme construction, the only way to find out is to study the γ-ray coincidences. When a number of known γ rays are found to exist in coincidence, it is almost certain that a transfer took place. The reader will notice that in some spectra, some peaks could not be identified and their origins are not understood. Some of the relatively weakly produced nuclei such as ^{194}Pt are very close to the noise level. It will also be noticed that a number of lines associated with ^{150}Dy are observed for both experiments. This is due to the fact that the ^{127}I hit the target frame made of ^{27}Al. The observed nuclei for the first experiment, the number of transfered nucleons, the relative intensities of the observed gammas and the Q values are shown in Table 4.1 and for the second experiment in Table 4.2. The term relative intensities mentioned in both Tables 4.1 and 4.2 refer to the intensity of a transition and compared to the sum of all intensities of

transitions to the ground state of ^{197}Au and ^{194}Pt respectively.
The GRAZING program plots among other things the laboratory energy vs relative cross-sections as shown in Figs. 4.8, 4.9, 4.17 and 4.18. One can easily extract the values of these cross sections as tabulated in Tables 4.1.and 4.2.
The first of the spectra displayed is the cross-coincidence between ^{197}Au and ^{127}I whose γ-rays energies are well known, and are relatively abundant. By gating on the 651 keV γ ray of ^{127}I, one can see a number of γ rays from ^{127}I and ^{197}Au, and the same happens when gating on 279 keV γ ray from ^{197}Au. These are shown in Fig. 4.10.
The spectra that follow, Fig. 4.11, illustrate the transfer of one proton to and the loss of two neutrons from ^{197}Au, producing ^{196}Hg. The γ transitions gated upon were at E_γ = 426 keV and 635.4 keV. They are found to be mutually coincident, but not with γ rays from the projectile-like fragment ^{128}Te.

The following spectra, Fig. 4.12 clearly show transitions associated with ^{198}Hg at 636 keV and 695 keV associated with ^{126}Te. When gating on 635.4 keV, there is a possibility as shown that the 666 keV line could belong to ^{126}Te which is the projectile-like fragment. Some large peaks could not be identified in Fig. 4.12.

In Fig. 4.13, the ^{197}Au nucleus has gained one proton and two neutrons to produce ^{200}Hg, and its lines in the spectra are easily identified when gating on 368 keV and 579 keV. The 279 keV line associated to the ground state of ^{197}Au is the most dominant feature of these spectra. In Fig. 4.14 the ^{197}Au nucleus has lost one proton and two neutrons to produce ^{194}Pt. The corresponding 328 keV and 483 keV lines are observed in mutual coincidence. As one goes up in spin, it can be seen that the number of counts decrease dramatically to such an extent that the 328 keV line could easily be confused with noise, but as it will be shown for the second experiment the 328 keV and 483 keV lines are the

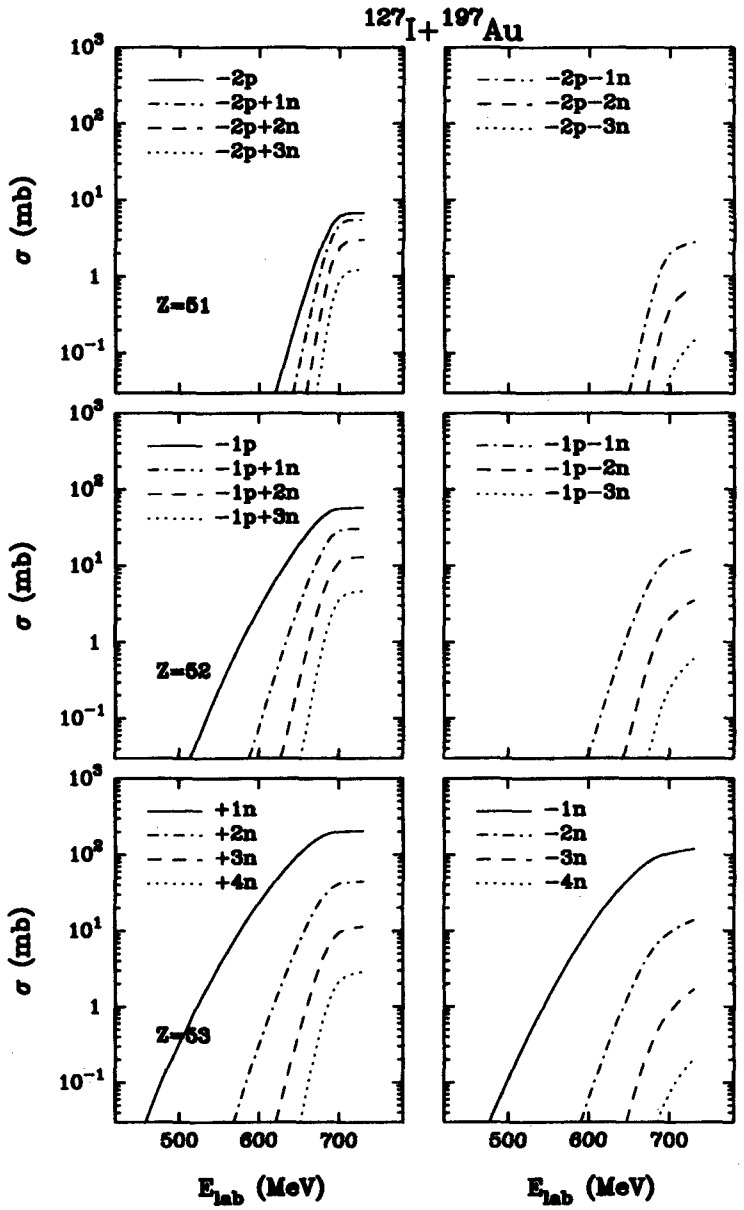

Figure 4.8: Relative cross section for the production of beam-like fragment vs energy using the GRAZING program for the first experiment.

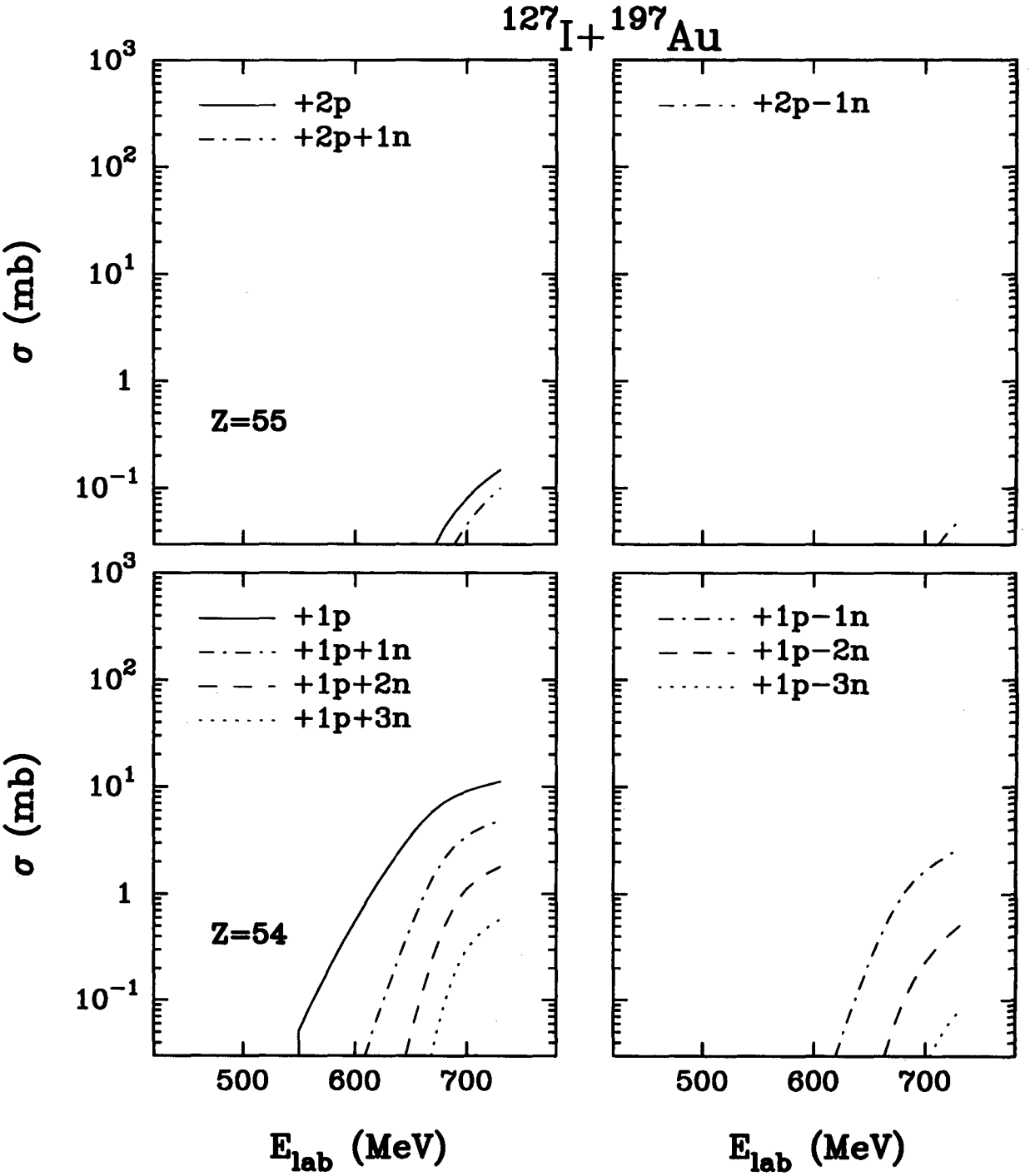

Figure 4.9: Relative cross section for production of beam-like fragments vs energy using the GRAZING program for the first experiment (continued).

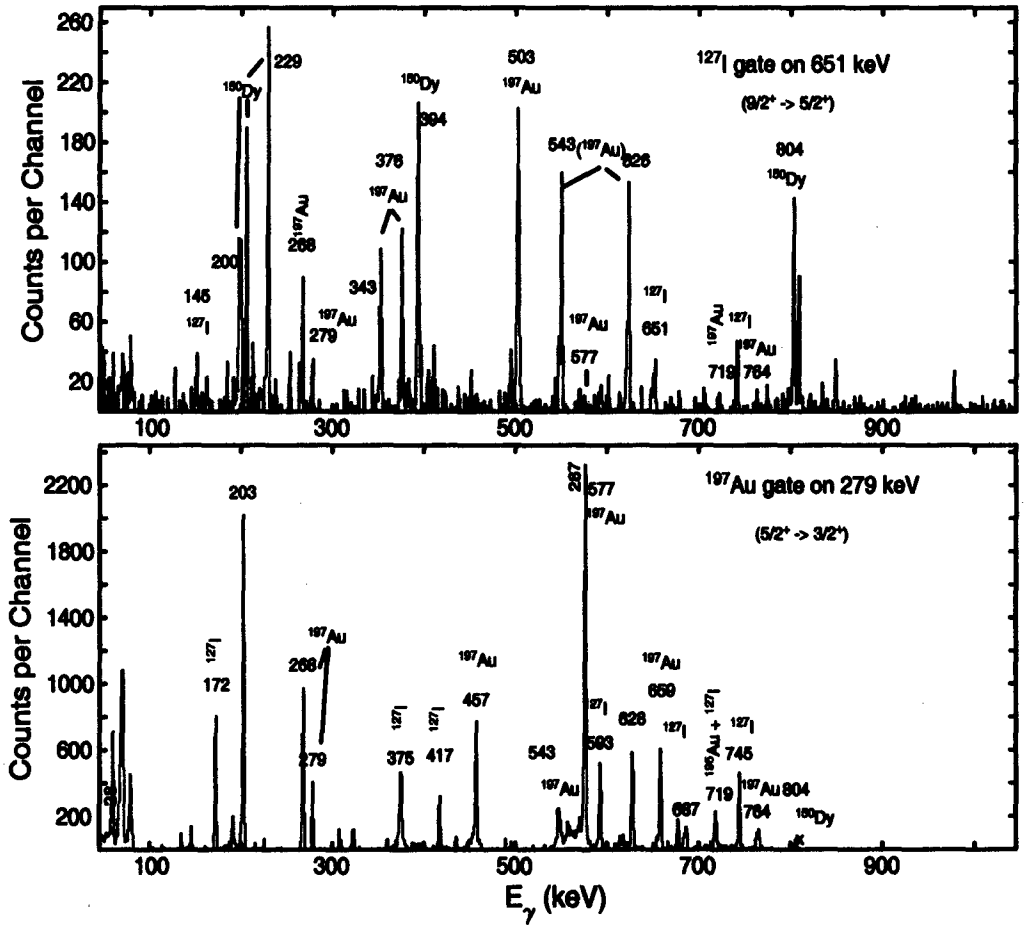

Figure 4.10: Spectra gated on 651 keV in ^{127}I and 279 keV in ^{197}Au observed in cross-coincidence.

most intense in ^{194}Pt. The projectile-like fragment was found, namely ^{130}Xe, but not in cross-coincidence with ^{194}Pt.

Fig. 4.15 shows the spectra of ^{196}Pt and ^{128}Xe in cross-coincidence. When gating on the 590 keV line associated with ^{128}Xe, the 443 keV and 704 keV line belonging to the same nucleus can be clearly seen so can the lines of ^{196}Pt. When gating on 521 keV associated with ^{196}Pt, some ^{128}Xe lines and the 355 keV line associated with ^{196}Pt can also be seen. In Fig. 4.16, the ^{197}Tl lines are clearly identifiable, but the most dominant features of these spectra are those

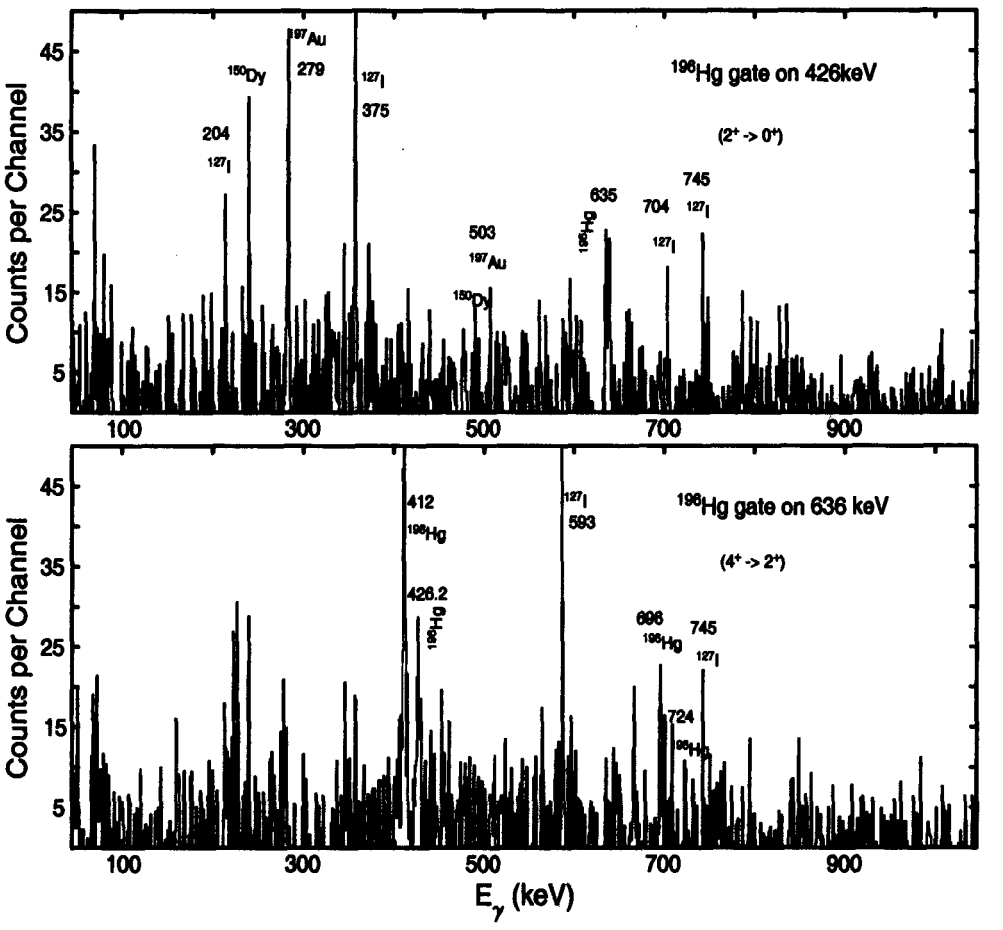

Figure 4.11: Spectra gated on 426 KeV and 635 keV in ^{196}Hg.

of ^{197}Au and ^{127}I and of course many randoms and noise. In this case ^{197}Au gained two protons and lost two neutrons. The 407 keV and 721 keV lines of ^{193}Au were found to be in mutual coincidence.

Odd-odd nuclei tend to be difficult to study, since they often have many weak decay paths and commonly possess isomeric states. In addition to the nuclei tabulated above for the first experiment, ^{198}Au and ^{126}I were observed to exist but their relative coincidence intensities could not be extracted as one is working with odd-odd nuclei where the observed γ-rays decay to the ground state. When gating for instance on 179 keV which is associated with ^{198}Au ($2^+ \rightarrow 2^-$)

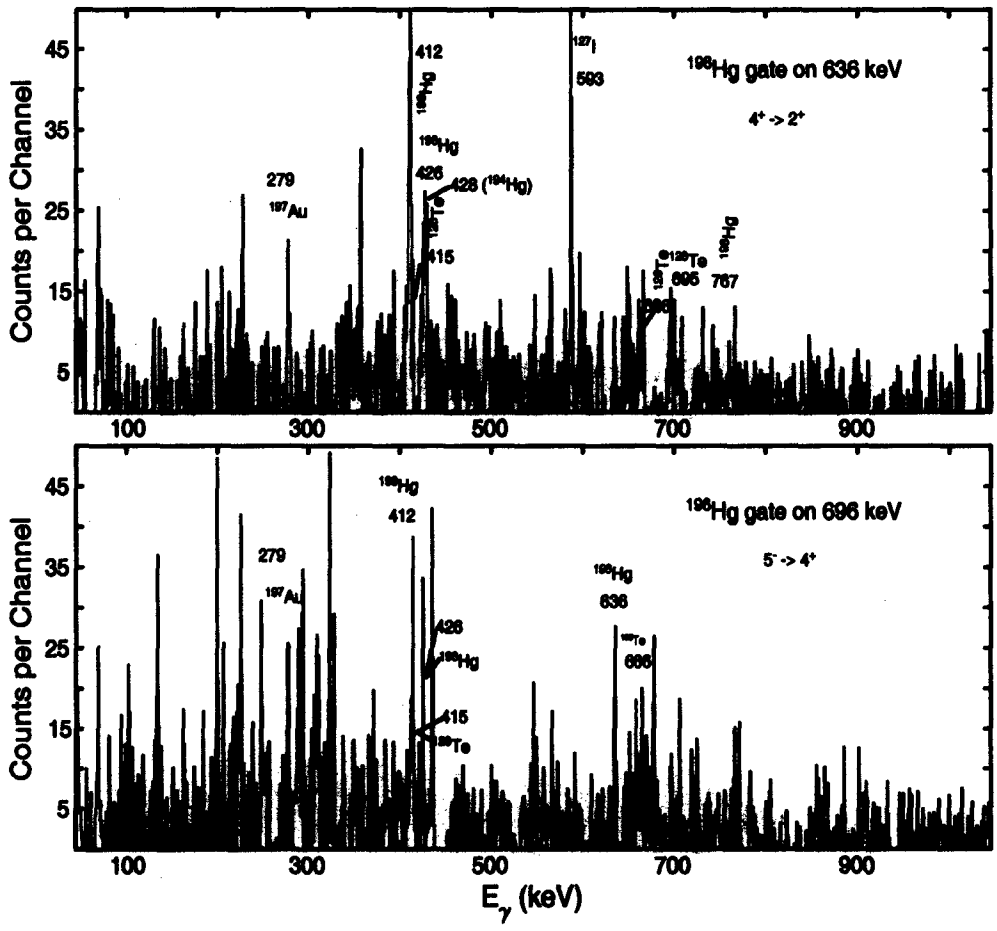

Figure 4.12: The top spectrum shows ^{198}Hg and ^{126}Te observed in cross-coincidence when the spectrum is gated on 636 keV in ^{198}Hg. The bottom spectrum is gated on 696 keV in ^{196}Hg.

one sees various transitions associated with ^{126}I namely 328 keV and 247 keV which decay from their excited states to the ground state 2^-. One can therefore assume that these two nuclei exist in coincidence.

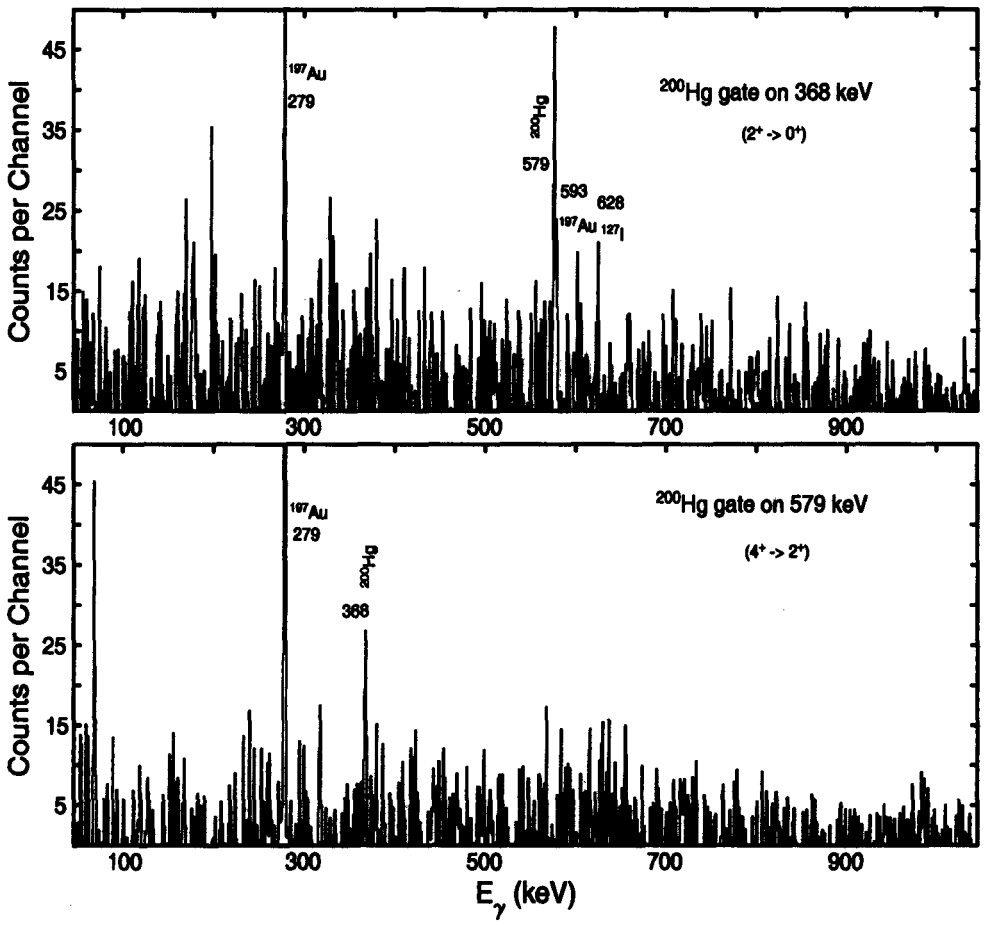

Figure 4.13: Spectra gated on 368 keV and 579 keV in ^{200}Hg.

4.2.2 The ^{194}Pt + ^{127}I Reaction

In the next few spectra it will be shown that a number of nucleon transfers have been observed. It will also be seen that in most if not all cases, the strongest transitions seen are the ones associated with ^{194}Pt and ^{127}I. The first spectra show the γ rays of ^{194}Pt and ^{127}I in coincidence. More projectile-like fragments were observed than in the previous experiment. This could be due to the fact that the statistics were much better than in the first experiment having used the data for three weekends as opposed to only one weekend of

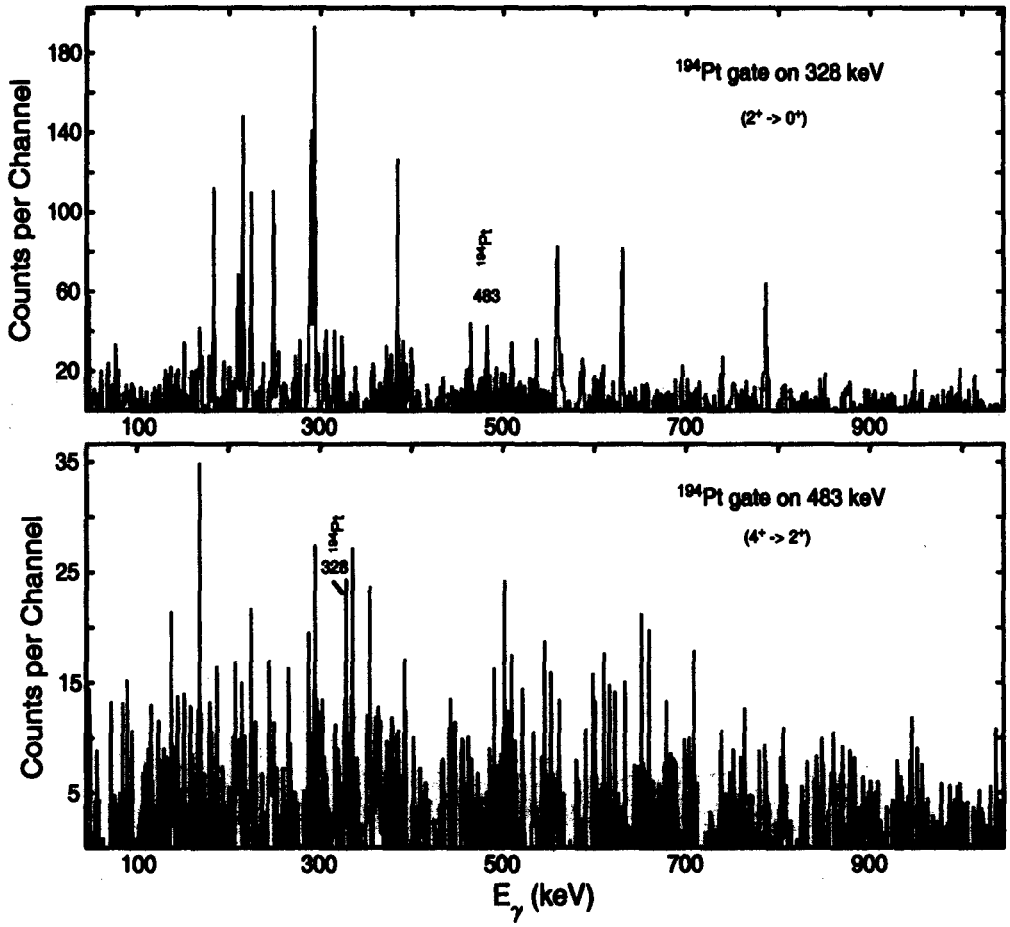

Figure 4.14: Spectra gated on 328 keV and 483 keV in ^{194}Pt.

contaminated data. These spectra are illustrated in Fig. 4.19.

The spectra illustrated in Fig. 4.20, show lines associated with ^{193}Au very clearly. ^{194}Pt has gained a proton and lost 2 neutrons. When gating on the 408 keV transition, one can see the first two transitions of the projectile-like fragments in coincidence, namely, ^{128}Te with it. The transitions 721 keV and 408 keV are in coincidence with each other. In this instance ^{127}I has lost one proton and gained two neutrons. The γ rays seen from ^{193}Au belong to the $h_{11/2}$ decoupled band (favoured sequence and not to the ground state band) [Iel].

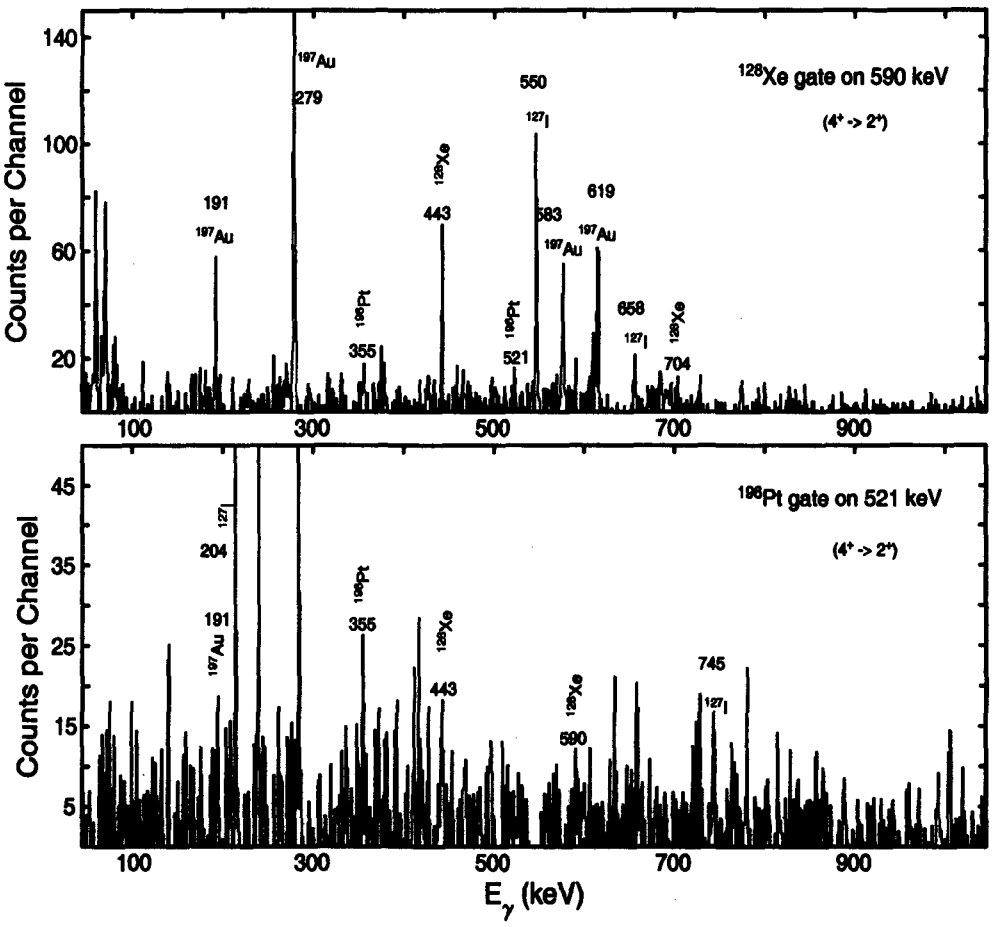

Figure 4.15: Spectra gated on 521 keV in ^{196}Pt and 590 keV in ^{128}Xe observed in cross-coincidence.

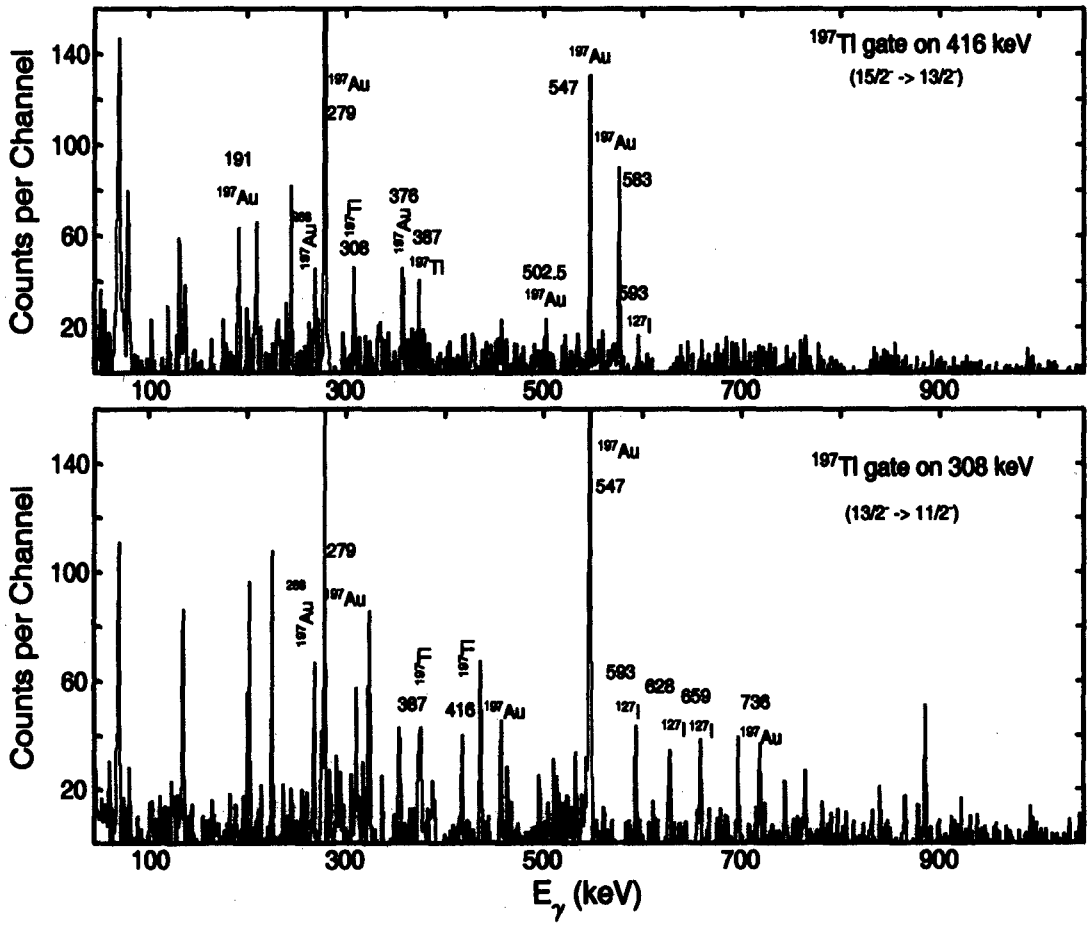

Figure 4.16: Spectra gated on 416 keV and 308 keV in ^{197}Tl.

Observed nuclei	Transfered nucleons	Relative Intensity	σ_{th} (mb)	Q (MeV)	N/Z
^{196}Hg	+1p -2n	1.93 ± 0.49	15	-1.981 ± 0.006	1.45
^{198}Hg	+1p	2.84 ± 0.58	60	6.310 ± 0.006	1.47
^{200}Hg	+1p +2n	0.65 ± 0.36	3	-2.780 ± 0.007	1.50
^{194}Pt	-1p -2n	0.41 ± 0.20	2	2.462 ± 0.005	1.49
^{196}Pt	-1p	0.50 ± 0.20	15	-0.101 ± 0.005	1.51
^{128}Xe	+1p	0.64 ± 0.38	15	-0.100 ± 0.005	1.37
^{197}Tl	+2p -2n	1.09 ± 0.34	3	-0.476 ± 0.003	1.43
^{193}Au	-4n	0.77 ± 0.38	2	-2.633 ± 0.003	1.44

Table 4.1: Reaction products from the first experiment, Relative intensities, σ_{th} calculated using the GRAZING program, Q-values and N/Z values.

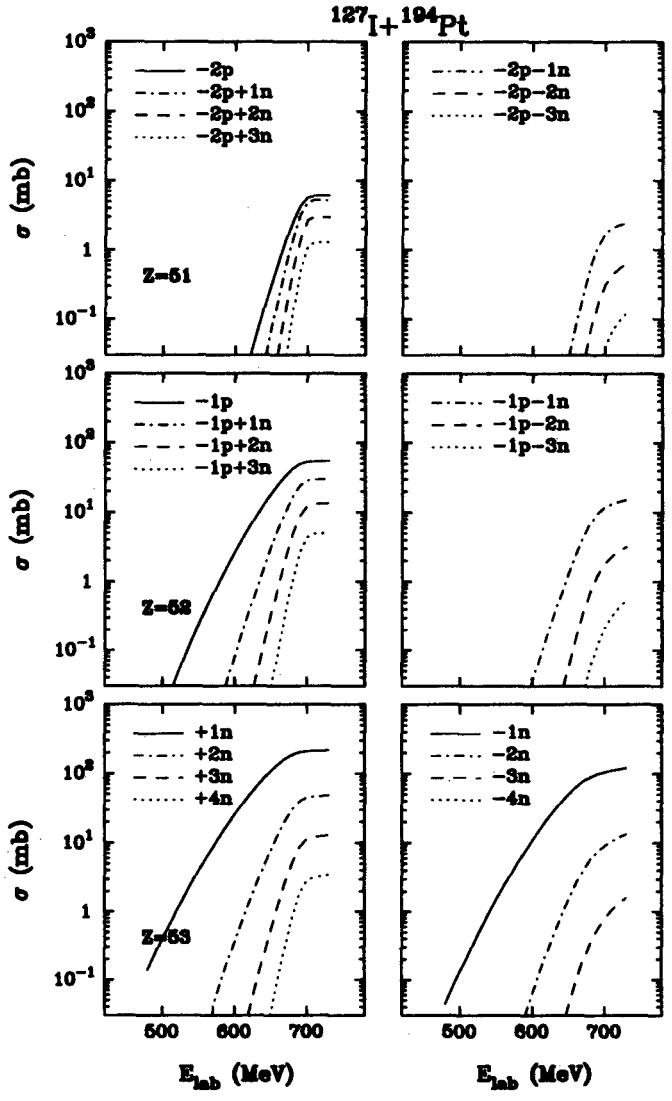

Figure 4.17: Relative cross section for the production of beam-like fragments vs energy plot using the GRAZING program for the second experiment.

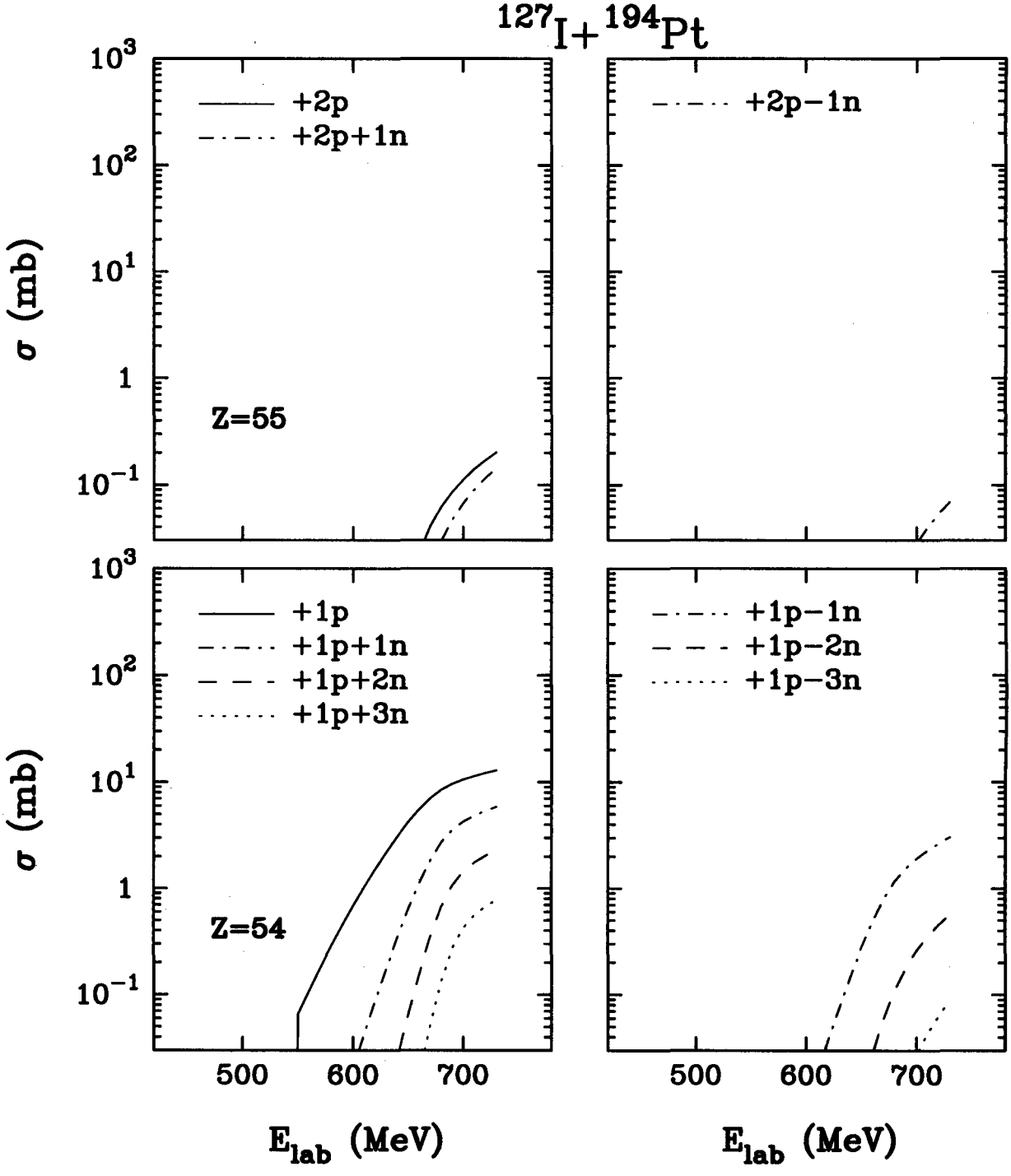

Figure 4.18: Relative cross section for the production of beam-like fragments vs energy using the GRAZING program for the second experiment (continued).

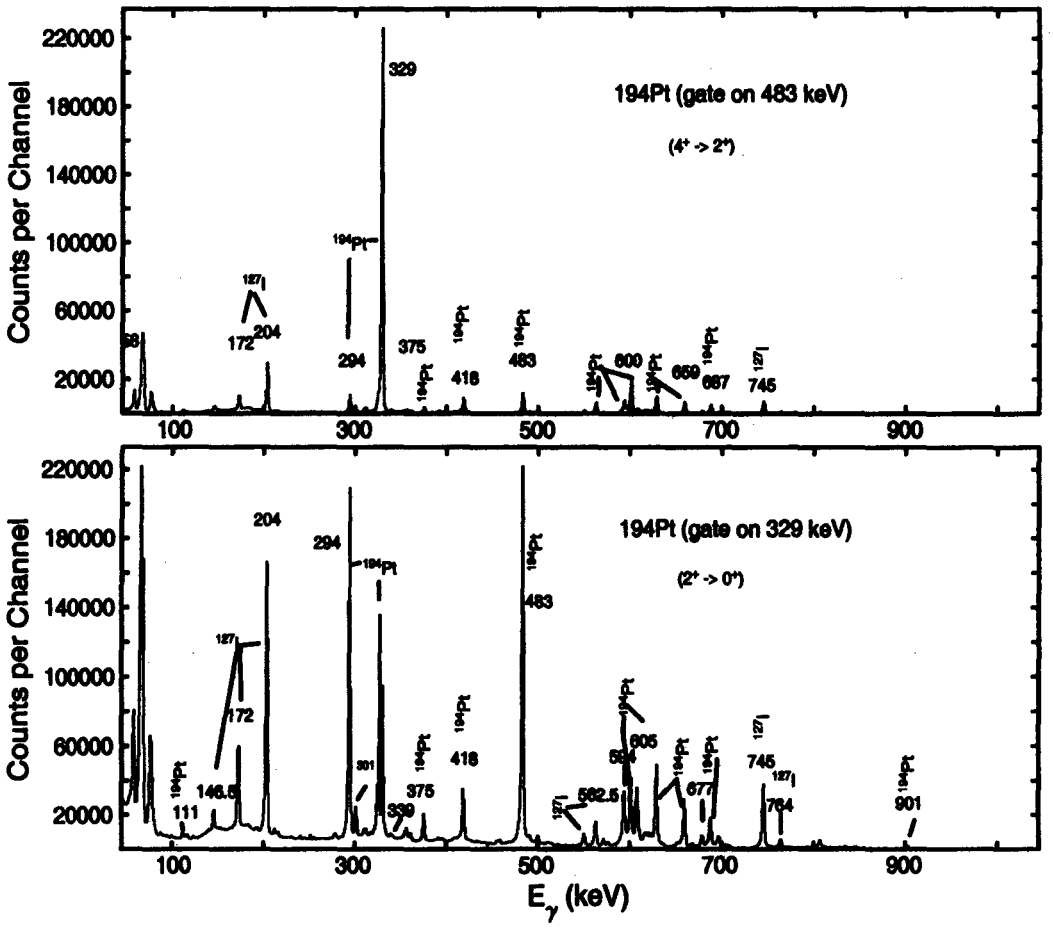

Figure 4.19: Spectra gated on 483 keV and and 329 keV in ^{194}Pt observed in cross-coincidence with ^{127}I.

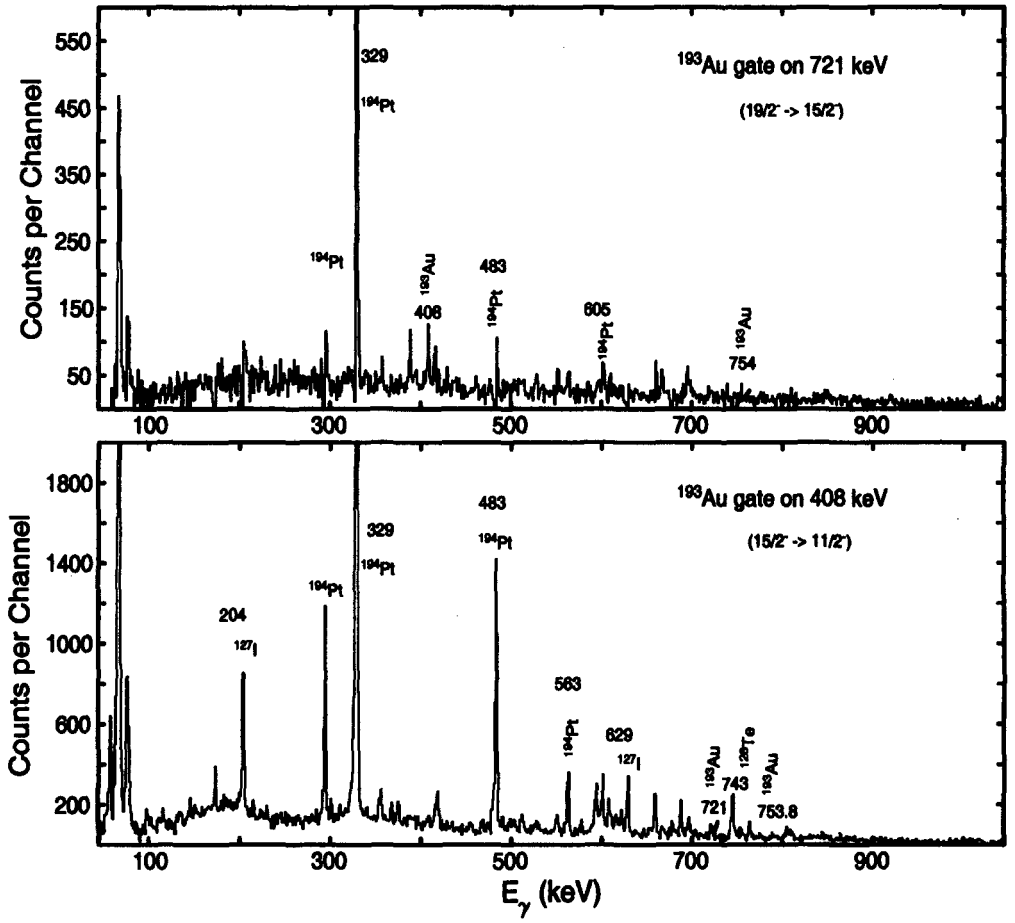

Figure 4.20: Spectra gated on 721 keV and 408 keV in ^{193}Au.

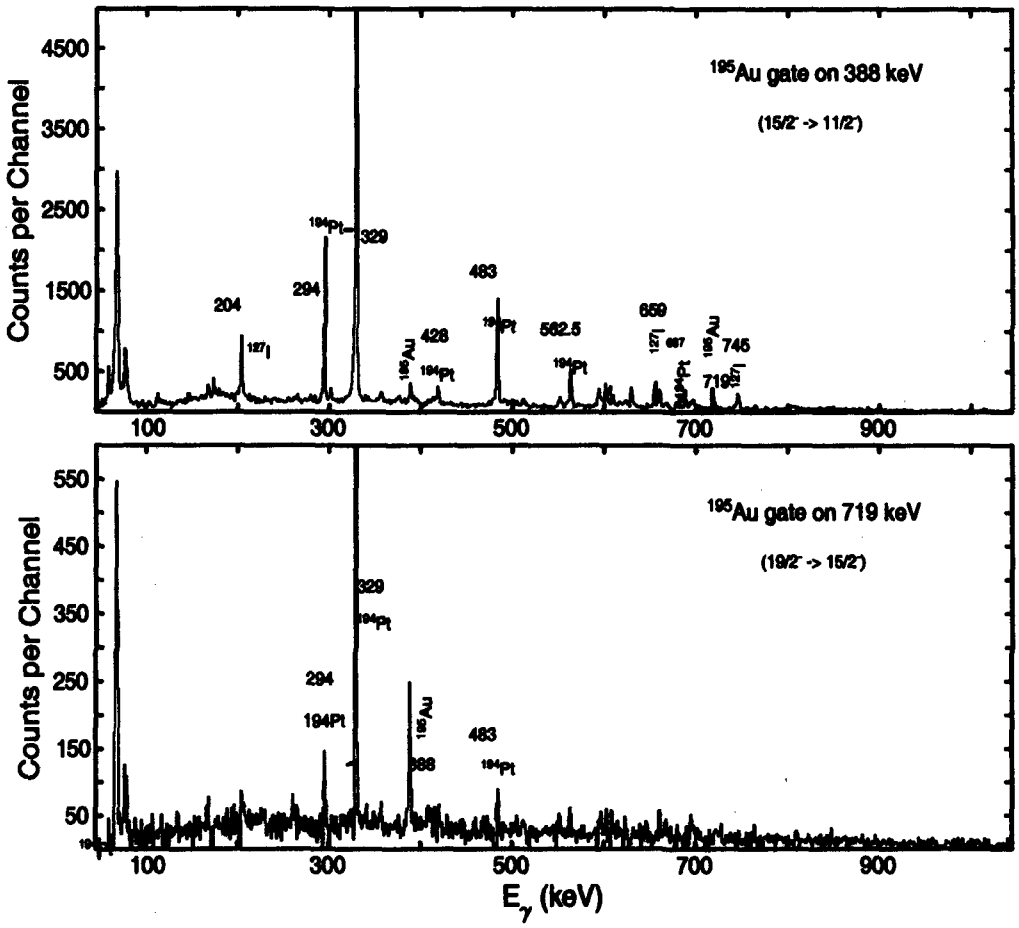

Figure 4.21: Spectra gated on 388 keV and 719 keV in ^{195}Au.

In Fig. 4.21, the spectra of ^{195}Au are shown with the same γ rays as in the first experiment. It was impossible to see anything above the 719 keV line. In the present case, ^{194}Pt has gained one proton.

^{126}Te is the projectile-like partner of ^{195}Au and both nuclei can clearly be seen in cross-coincidence when gating on the 666 keV lines of ^{126}Te. The 415 keV line of ^{126}Te associated with the $6^+ \rightarrow 4^+$ transition is also clearly visible. This is shown in Fig. 4.22. The 343 keV and 489 keV lines from Fig. 4.23 associated with ^{191}Ir, are clearly seen to be in coincidence. In this instance, ^{194}Pt has lost one proton and two neutrons. In Fig. 4.24, the 603 keV and 499 keV lines

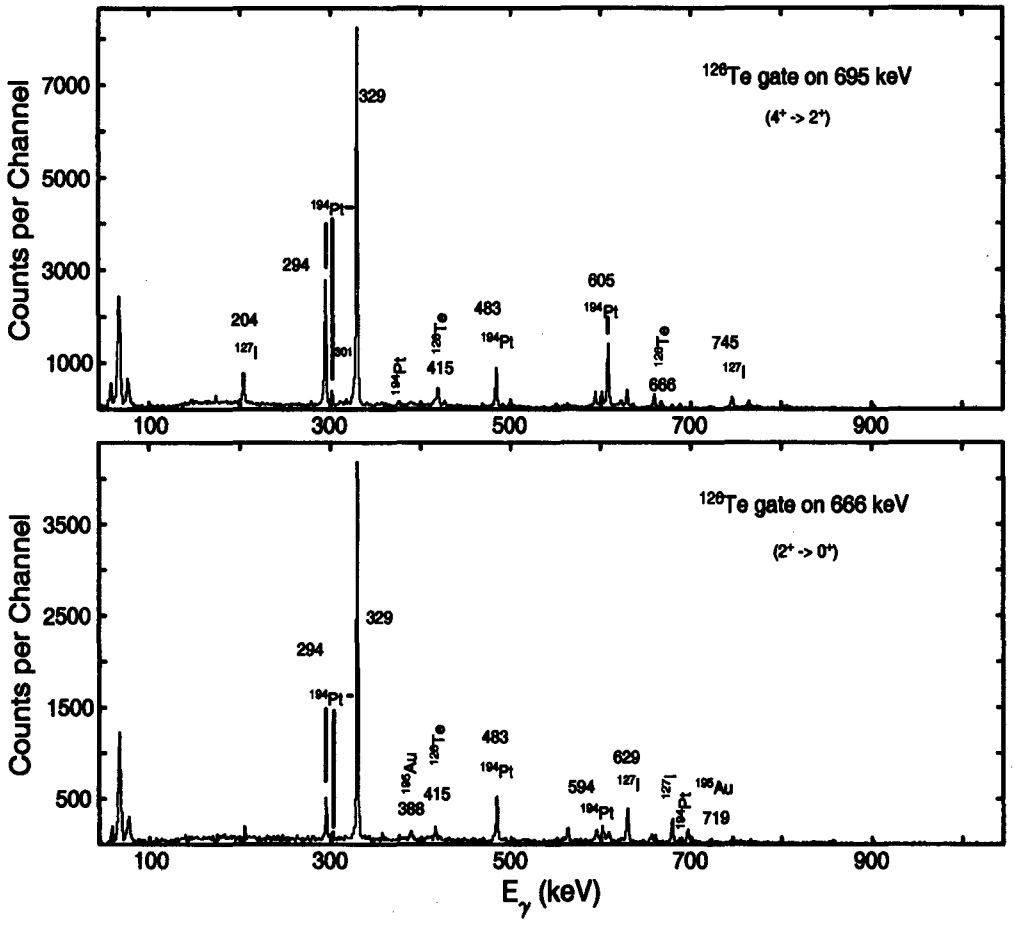

Figure 4.22: Spectra gated on 695 keV and 666 keV in ^{126}Te.

associated with ^{193}Ir are also seen to be in coincidence. In the case of ^{193}Ir, ^{194}Pt has lost one proton. When gating on the 603 keV line, the 603 keV line is in coincidence with the 499 keV and 358 keV lines. The 358 keV line is associated with the ground state transition ($\frac{7}{2}^+ \rightarrow \frac{3}{2}^+$). In Fig. 4.25, ^{194}Pt has gained two protons and lost two neutrons to produce ^{194}Hg. The γ rays associated with the first two excited states were observed to exist in coincidence namely the 428 keV and 637 keV lines. No projectile-like-fragments were observed. In Fig. 4.26, the 426 keV and 636 keV lines associated with ^{196}Hg are shown to be in coincidence. In this instance ^{194}Pt has gained two protons.

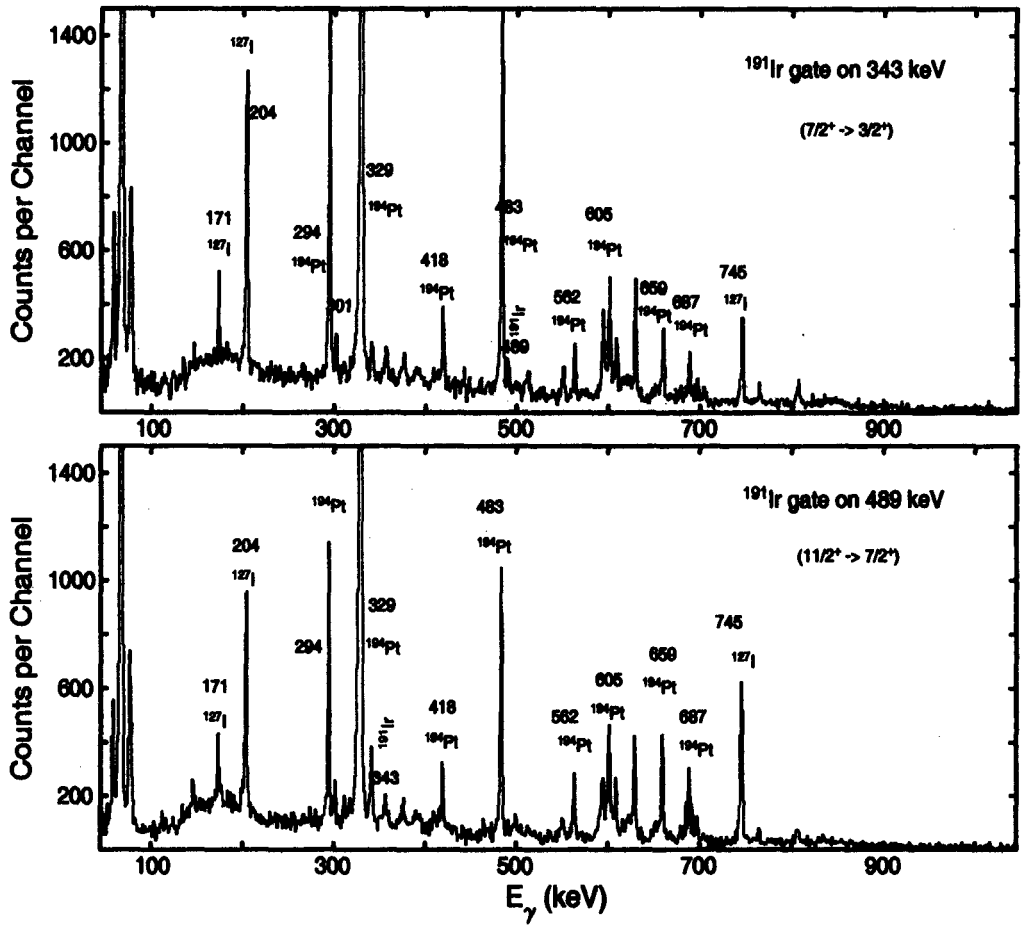

Figure 4.23: Spectra gated on 343 keV and 489 keV in ^{191}Ir.

The ^{128}Xe nucleus could be seen up to the 6^+ state. As shown in Fig. 4.27, the first two transitions are seen to be in coincidence, namely 443 keV and 590 keV together with 704 keV (6^+ state). In this instance ^{127}I gained one proton. Even though the target does not consist of 100% ^{194}Pt, it is 97.8 % pure, and contains some ^{192}Pt and some ^{196}Pt, the following spectra, Fig. 4.28, show ^{190}Pt, but not in cross-coincidence with ^{131}I as it is difficult to observe. It does not show any ^{192}Pt lines that are presented in Fig. 4.29. It can therefore be assumed that ^{194}Pt has indeed lost four neutrons. The 551 keV and 441 keV lines are seen in coincidence with each other and other lines of the same

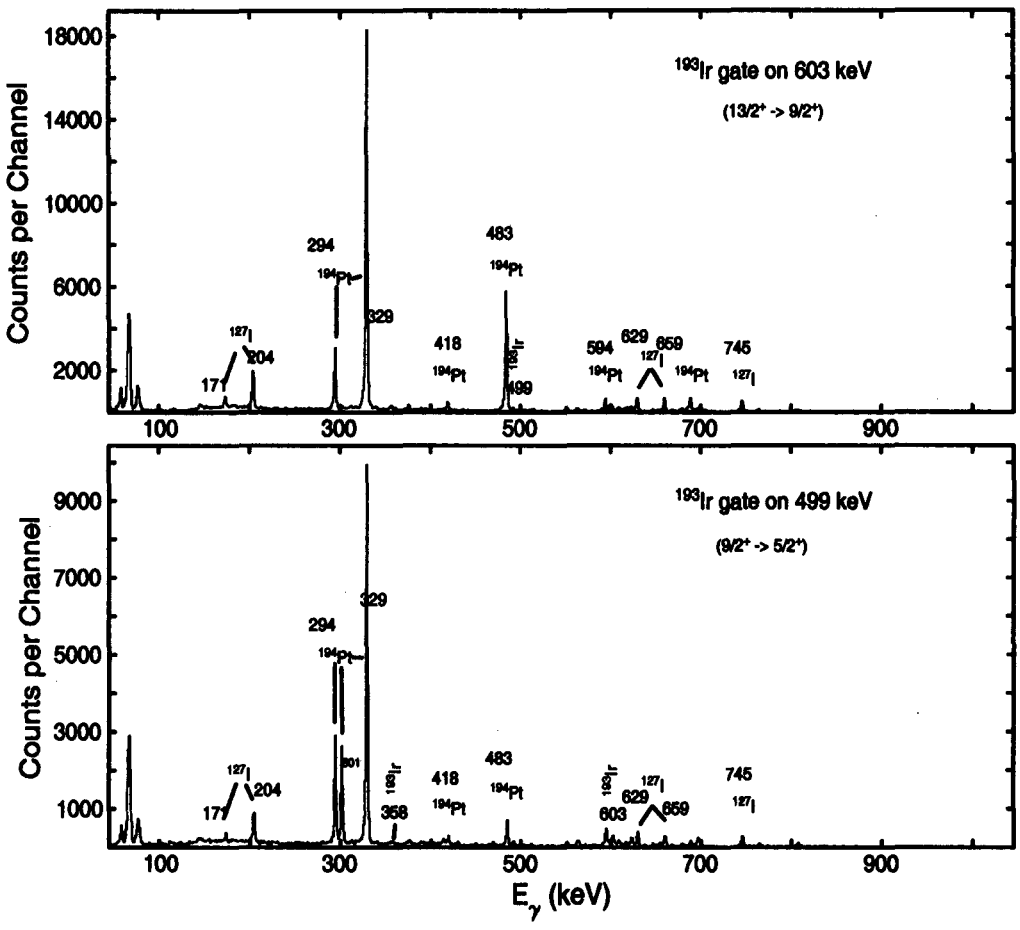

Figure 4.24: Spectra gated on 603 keV and 499 keV in ^{193}Ir.

isotope shown in the same spectra.

As discussed for the previous spectra of ^{190}Pt, there is some ^{192}Pt in the target, but very few lines associated with that particular isotope are present. In fact in this particular case ^{192}Pt is populated up to the 10^+ state, relatively high when comparing with the other isotopes of Pt, but not as many bands as with ^{194}Pt. It can therefore be concluded that two neutrons were lost from ^{194}Pt. The above is seen in Fig. 4.29. Fig. 4.30 shows the spectrum of ^{193}Pt. ^{194}Pt lost one neutron to produce ^{193}Pt. Two energies were chosen and were shown to be in coincidence with each other and others. One will notice that when gating on 341 keV and

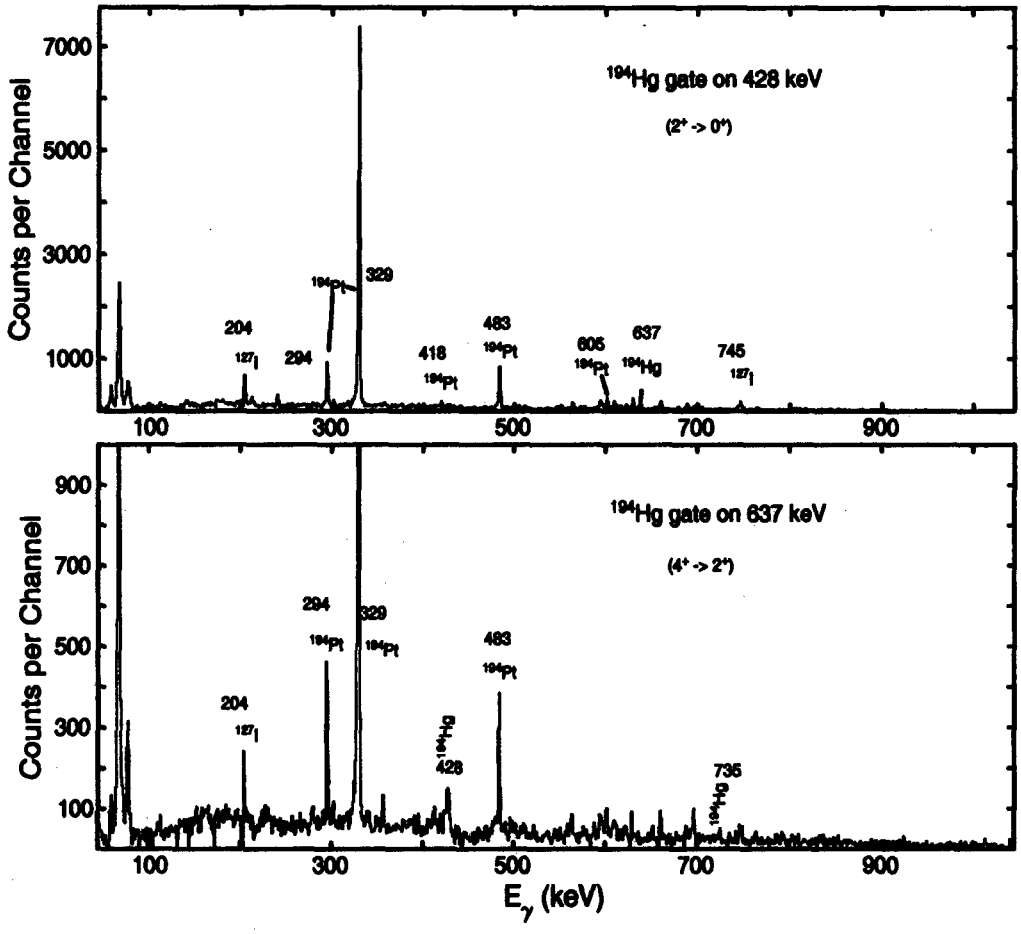

Figure 4.25: Spectra gated on 428 keV and 637 keV in ^{194}Hg.

512 keV, these lines are in coincidence with themselves. Most probably for the reason explained in the level scheme construction section at the begining of this chapter. The case of Fig. 4.31 case is of course as complicated as with ^{192}Pt, as the target contains some ^{196}Pt, but again besides the ground state band, none of the others available in the literature could be found. It is hence assumed that we populate ^{196}Pt through a direct contact between it and the projectile (^{127}I) and also through ^{194}Pt having gained two neutrons as two lines associated with the projectile-like fragment can be seen namely the 596 keV and 608 keV lines associated with ^{125}I. As for the first experiment, other nuclei could be

Observed nuclei	Transfered nucleons	Rel. Intensity	σ_{th} (mb)	Q (MeV)	N/Z
^{193}Au	+1p-2n	0.20 ± 0.07	10	1.201 ± 0.003	1.44
^{195}Au	+1p	0.24 ± 0.08	60	1.450 ± 0.004	1.47
^{126}Te	-1p	0.30 ± 0.09	60	1.450 ± 0.004	1.42
^{196}Hg	+2p	0.95 ± 0.12	6	1.542 ± 0.002	1.45
^{194}Hg	+2p-2n	0.14 ± 0.04	0.5	0.500 ± 0.003	1.43
^{193}Ir	-1p	0.27 ± 0.06	12	-1.722 ± 0.003	1.48
^{128}Xe	+1p	0.20 ± 0.05	12	-1.722 ± 0.003	1.37
^{191}Ir	-1p-2n	0.11 ± 0.06	2	0.483 ± 0.002	1.48
^{190}Pt	-4n	0.78 ± 0.11	4	1.000 ± 0.003	1.44
^{192}Pt	-2n	0.86 ± 0.14	15	1.032 ± 0.004	1.46
^{193}Pt	-1n	0.38 ± 0.05	200	-1.544 ± 0.005	1.47
^{196}Pt	+2n	1.32 ± 0.10	15	-2.263 ± 0.005	1.51
^{125}I	-2n	1.53 ± 0.30	15	-2.263 ± 0.005	1.36

Table 4.2: Reaction products from the second experiment, Relative intensities, σ_{th} using the GRAZING program, Q- values and N/Z values.

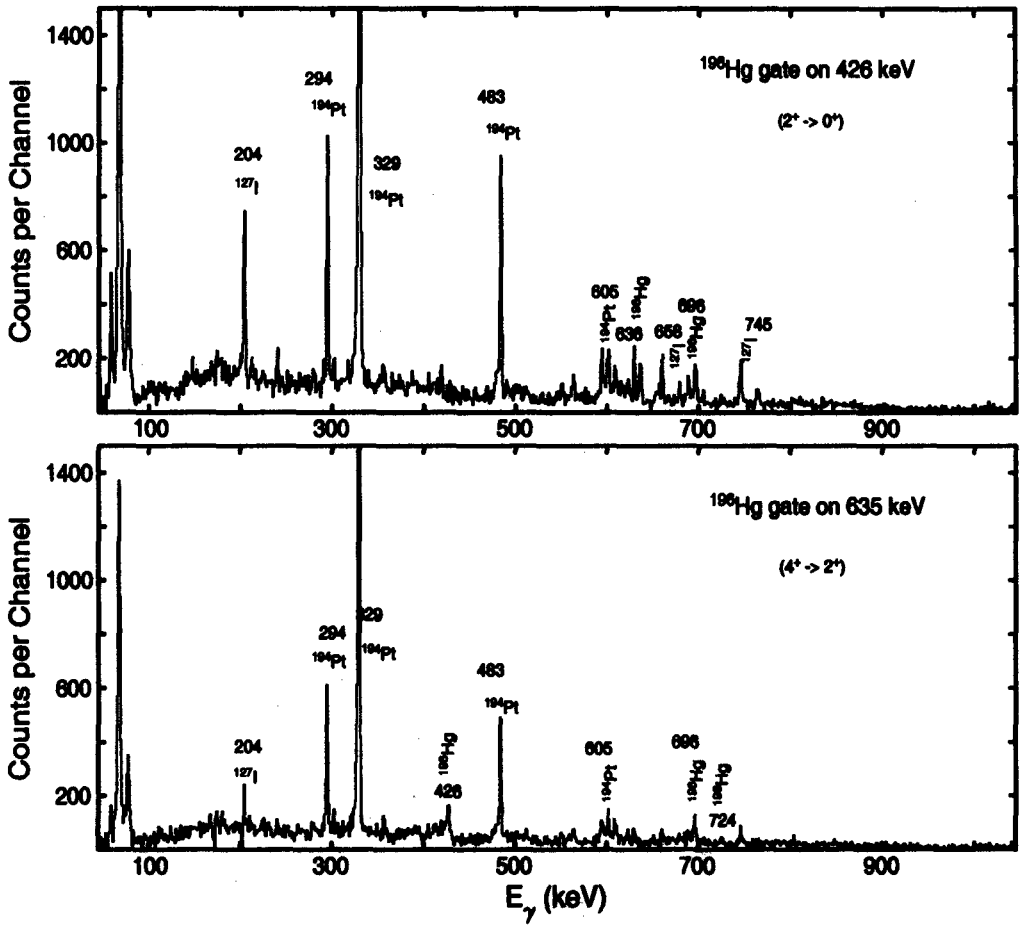

Figure 4.26: Spectra gated on 426 keV and 635 keV in ^{196}Hg.

observed but their coincidence intensities could not be extracted. When gating on 341 keV associated with ^{193}Pt, one can see only one γ ray associated with ^{128}I. Having only two γ rays from two different nuclei, it is difficult to decide whether the above exist in coincidence. The 596 keV transition associated with the ^{125}I is in coincidence with the 356 keV γ ray associated with ^{196}Pt. When gating on the latter, on sees two γ's associated with ^{125}I, namely the 596 keV and 608 keV transitions which decay from their respective excited states to the ground state. In Tables 4.1 and 4.2, the values σ_{th} refer to the relative cross sections predicted by the GRAZING program. The term Relative Intensities

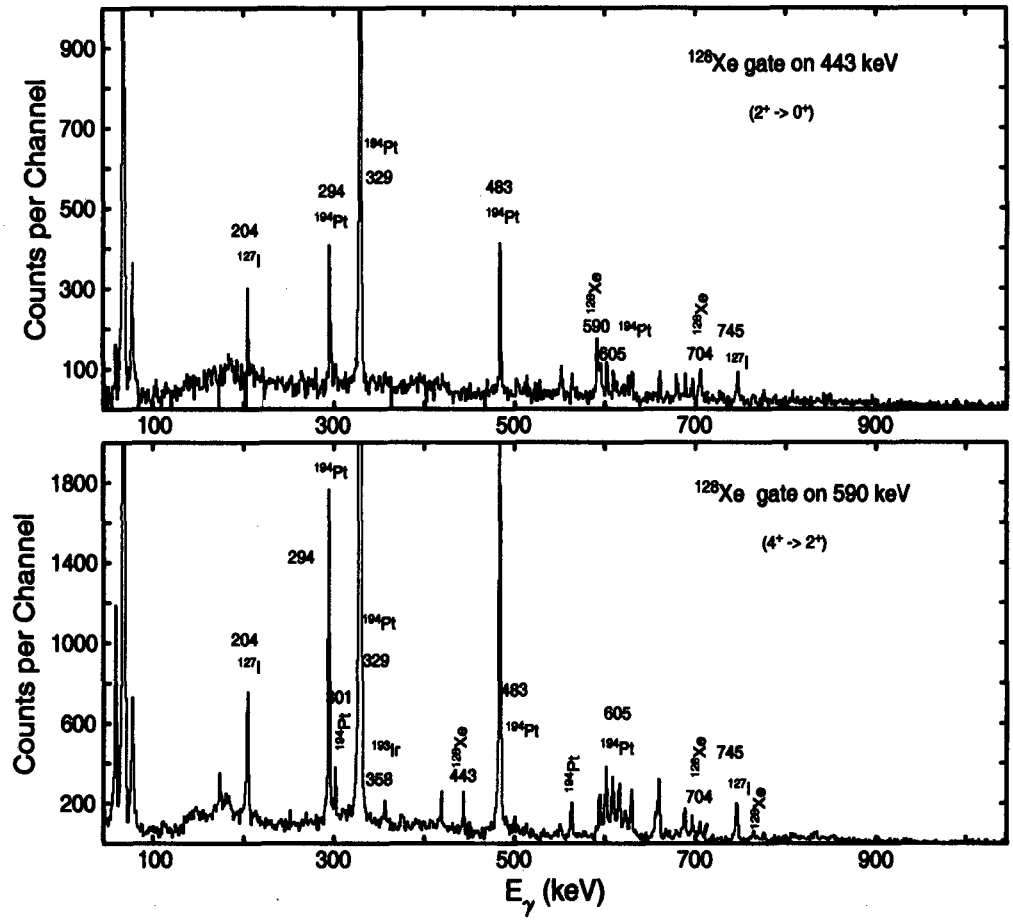

Figure 4.27: Spectra gated on 443 keV and 590 keV in ^{128}Xe. In the bottom spectrum, ^{128}Xe and ^{193}Ir can be seen in cross-coincidence.

in Tables 4.1 and 4.2 are those intensities relative to the strongest transitions in ^{197}Au and ^{194}Pt, respectively. The corresponding level schemes for the above spectra can be found in Appendices 1 and 2.

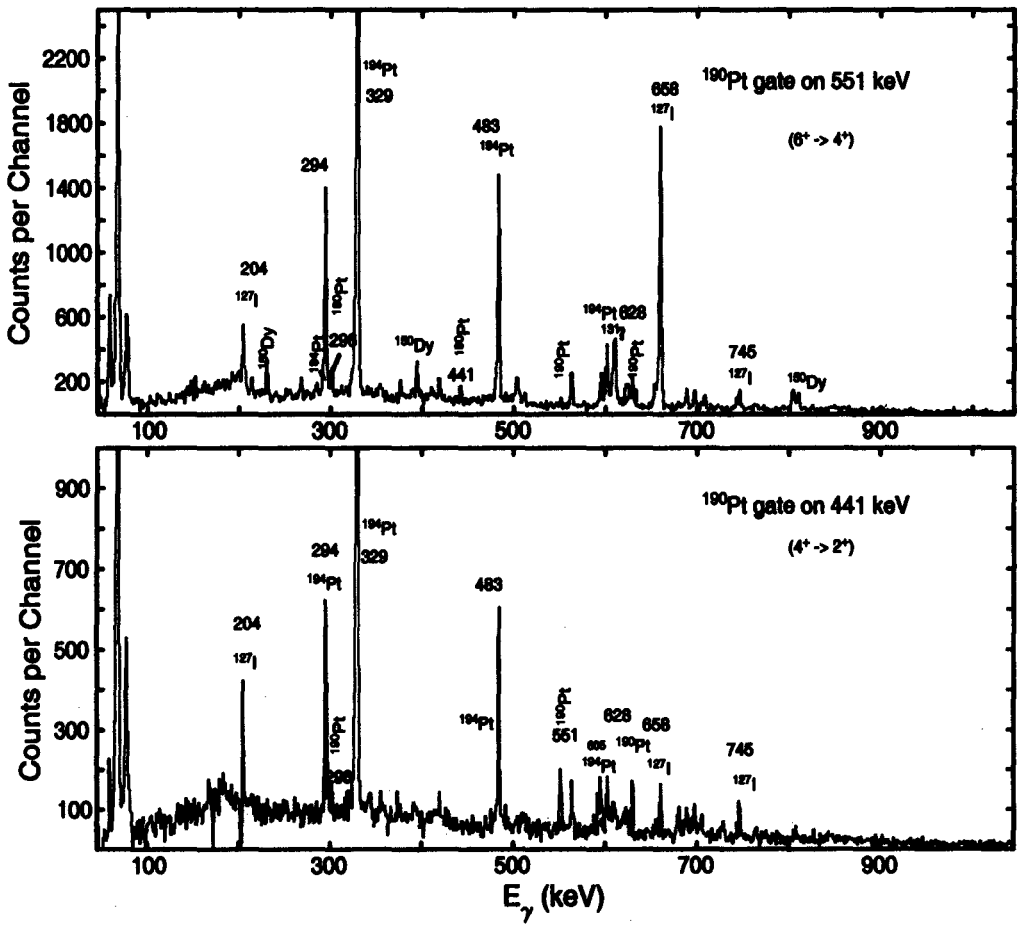

Figure 4.28: Spectra gated on 551 keV and 441 keV in ^{190}Pt.

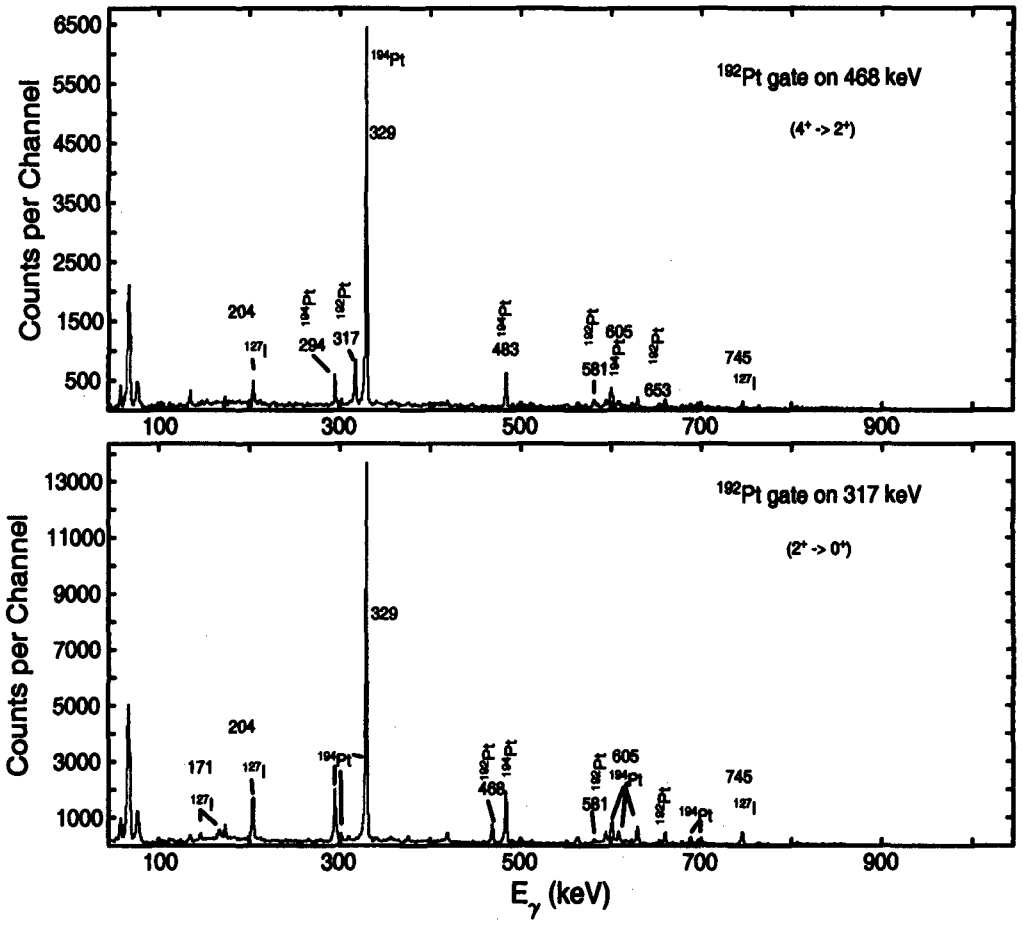

Figure 4.29: Spectra gated on 468 keV and 317 keV in ^{192}Pt.

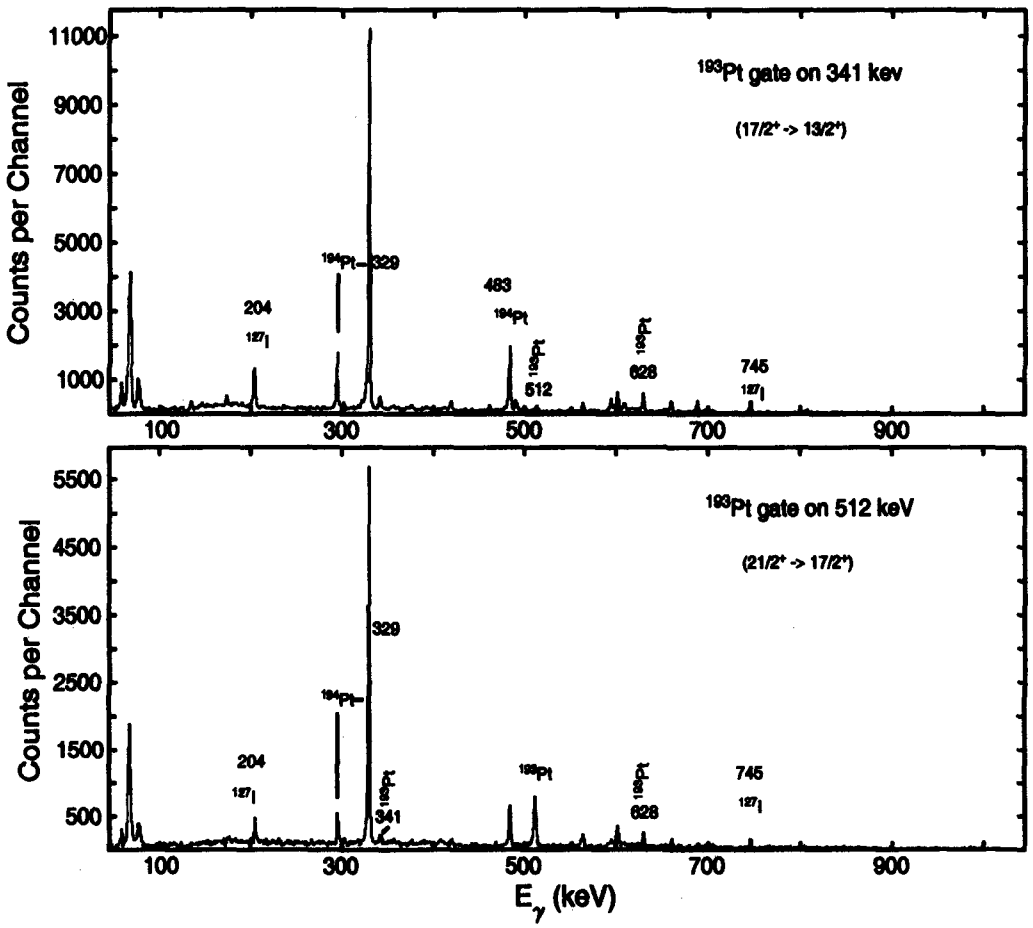

Figure 4.30: Spectra gated on 341 keV and 512 keV in ^{193}Pt.

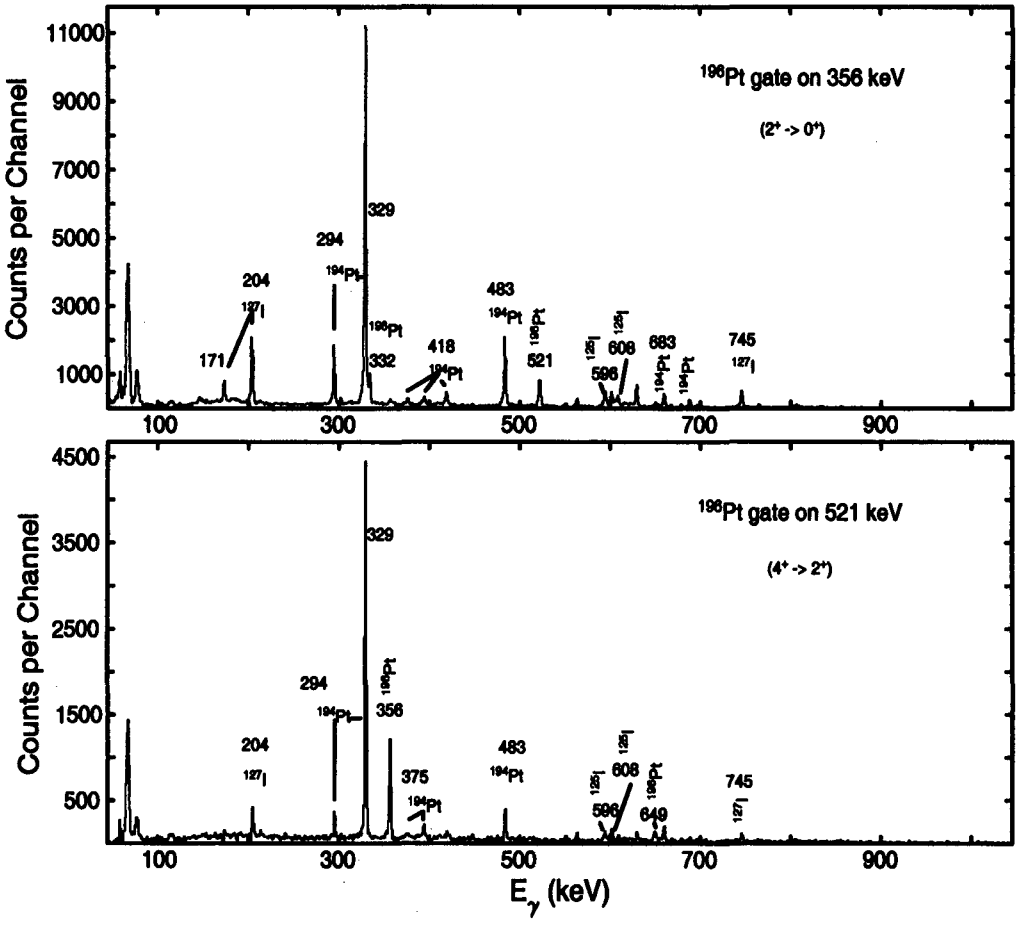

Figure 4.31: Spectra gated on 356 keV and 521 keV in ^{196}Pt.

4.2.3 *Energetics of Nuclear Reactions*

In a reaction X + a → Y + b, the conservation of total energy in our reactions gives [Kra88]:

$$m_x c^2 + T_X + m_a c^2 + T_a = m_Y c^2 + T_Y + m_b c^2 + T_b \tag{4.3}$$

where the Ts are the non-relativistic rest kinetic energies and the m's are the rest masses. The reaction Q value can be defined in analogy with the radioactive decay Q values, as the initial mass energy minus the the final mass energy:

$$Q_{gg} = (m_{initial} - m_{final})c^2 \tag{4.4}$$

$$Q_{gg} = (m_X + m_a - m_Y - m_b)c^2 \tag{4.5}$$

which is the same as the excess kinetic energy of the final products:

$$Q_{gg} = T_{final} - T_{initial} \tag{4.6}$$

$$Q_{gg} = T_Y + T_b - T_X - T_a \tag{4.7}$$

The Q-value may be positive, negative or zero. If Q is positive ($m_{initial} > m_{final}$ or $T_{final} > T_{initial}$) the reaction is said to be exothermic; in this case nuclear mass or binding energy is released as kinetic energy of the final products. When Q is negative ($m_{initial} < m_{final}$ or $T_{final} < T_{initial}$) the reaction is endothermic, and initial kinetic energy is converted into nuclear mass or binding energy. The changes in mass and energies are related by:

$$\Delta E = \Delta m c^2 \tag{4.8}$$

For transfer reactions, the two nucleon transfer strengths are strongly dependent on the Q-value, [Reg00]:

$$Q = Q_{gg} - Q(\Delta Z) \tag{4.9}$$

where

$$Q(\Delta Z) = [(\frac{Z_3 Z_4}{Z_1 Z_2}) - 1]V_{c.m} \tag{4.10}$$

Z_1 and Z_2 correspond to the projectile and target before the reaction. Z_3 and Z_4 correspond to the projectile-like and target-like fragments after the reaction. The more positive the Q-value, the higher the population. For neutron transfers, $Q = Q_{gg}$. Q_{gg} can be defined as the mass difference between initial and final products. $V_{c.m}$ is the Coulomb barrier in the center of mass frame and is calculated as follows:

$$V_{c.m} = \frac{1.44(Z_t Z_p)}{R} \tag{4.11}$$

and in the laboratory frame as

$$V_{lab} = \left(\frac{A_p + A_t}{A_t}\right) V_{cm} \tag{4.12}$$

where R is the interaction radius and is given by the following equation:

$$R = 1.16[A_p^{\frac{1}{3}} + A_t^{\frac{1}{3}} + 2] \tag{4.13}$$

Thus the Coulomb Barrier is defined as:

$$V_{lab} = \frac{1.44(\frac{A_p}{A_t} + 1)Z_p Z_t}{1.16(A_p^{\frac{1}{3}} + A_t^{\frac{1}{3}} + 2)} \tag{4.14}$$

where the subscripts p and t refer to projectile and target respectively. For the ^{197}Au + ^{127}I reaction, the laboratory frame Coulomb barrier is found to be 667.7 MeV and for the ^{194}Pt + ^{127}I reaction the laboratory frame Coulomb barrier is 678.02 MeV. These values have been calculated using Eq. 4.14. In general, deep-inelastic reactions can be understood in terms of a diffusion and relaxation process and toward equilibration of the neutron-to-proton ratio (N/Z), the kinetic energy and the angular momentum. The N/Z value is expected to equilibrate towards the value of the composite system. The N/Z values for the composite system for the first experiment are 1.45, ^{197}Au = 1.49 and ^{127}I

= 1.39. For the second experiment, the N/Z values for the composite system, ^{194}Pt and ^{127}I are 1.45, 1.49 and 1.39, respectively. In other words, the population of nuclei by the deep-inelastic transfer of nucleons is dictated by the mass and charge equilibration processes so that the N/Z value of the populated nuclei tends to that of the composite system or a fusion of the target and projectile [Lee97], [Asz99], [Asz00], [Dra96], [Coc00]. As mentioned in the theory section, in such reactions, where the projectile nucleus is incident upon the target at an energy above the Coulomb barrier but where the formation of of a compound nucleus is inhibited, the interacting nuclei come together long enough to exchange some nucleons before flying apart. The two outgoing fragments share the angular momentum and excitation energy brought about by the reaction. The angular momentum is divided into three components: that of the target-like fragment, that of the projectile-like fragment and the relative motion between the two. This last component depends on the degree of contact between the beam and the target nuclei. Previous studies have shown that in nucleon transfer reactions, it accounts for $\approx$ 5/7 of the total angular momentum available in the reaction, the amount one would expect using the theory of colliding spheres [Hib93], [Wil00]. The following will show the N/Z ratios of the detected reaction products. The N/Z values for the composite system for both experiments is 1.45 and the N/Z of ^{197}Au, ^{194}Pt and ^{127}I are very close to that of the composite system, and so are most of the reaction products. The targets are not very neutron rich and neither is the projectile, namely ^{127}I. Since, from the spectra displayed above, it is seen that the maximum number of nucleons transfered is four. This is low. We may conclude that the process is not solely deep-inelastic but mainly dominated by quasi-elastic reactions and by Coulomb excitation. The fact that few nucleons are transfered can help the conclusion that mainly quasi-elastic and grazing process is involved in addition to the Coulomb and deep-inelastic. The reason for all these processes taking

place could be attributed to the important thicknesses of the targets, where all the beam energy is deposited.The beam energy for for both experiments is 730 MeV, which means that we are only about 9% above the Coulomb Barrier. This is probably not enough to give us much chance of seeing real deep-inelastic reactions. Even at 10% above the barrier, one increases the chances of seeing more deep-inelastic reactions, but still not enough. Using thick targets in both experiments, means that the beam loses energy in the target and reacts at effectively lower beam energies, right down to the barrier. Hence the total cross-section will mainly be dominated by Coulomb excitation and quasi-elastic reactions. In his experiment, Kratz went above 30% above the barrier [Krat81]. Figs. 4.32 and 4.33 will illustrate the above. Butler et al. plot the Q-values of the reactions vs the relative intensities in order to determine whether a process is dominated by a quasi-elastic or deep-inelastic phenomenon [But98]. For example if the target has either lost or gained one proton, a line joining the two points can give a good indication as to the nature of the reaction. Lines that have a positive slope indicate quasi-elastic reactions whereas lines having a negative slope indicate deep-inelastic reactions. In the present work, in the first experiment ^{197}Au + ^{127}I, there is a case where the target has lost one proton to produce ^{196}Pt and gained one proton to produce ^{198}Hg. In Fig. 4.34, by drawing a line joining these two nuclei (red line), one can see that one is dealing with a case of quasi-elastic reaction as the slope joining the two points is positive. ^{194}Pt and ^{196}Hg were produced with ^{197}Au losing a proton and two neutrons and gaining a proton and losing two neutrons, respectively. Again by joining these two nuclei in Fig. 4.34, this time a negative slope is observed (green line). This is consistent with a deep-inelastic process. It is difficult to say whether these two neutrons were lost due to evaporation but ^{200}Hg was produced by a gain of one proton and two neutrons. By joining ^{200}Hg and ^{194}Pt in Fig.4.34 (blue line), the slope is slightly negative, hence it is possible that a

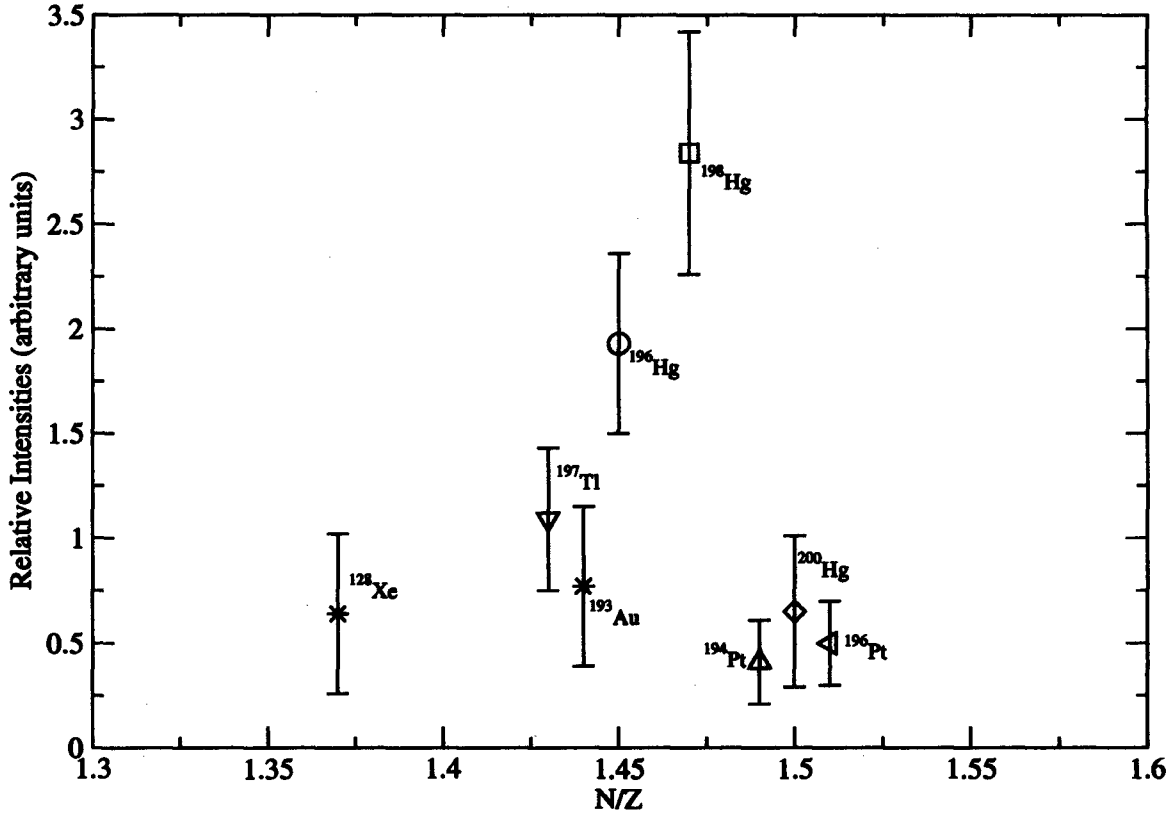

Figure 4.32: A plot of the N/Z values vs relative intensities for the first experiment (^{197}Au + ^{127}I)

deep-inelastic process has taken place.

In the second experiment ^{194}Pt + ^{127}I, the target has also lost one proton or gained one to produce ^{193}Ir and ^{195}Au, respectively. The line joining these two nuclei in Fig.4.35 (black line) is flat. It is not possible to draw a conclusion as to whether a quasi-elastic or deep-inelastic process took place. However ^{196}Pt and ^{192}Pt were produced with ^{194}Pt gaining two neutrons or losing two neutrons respectively. The line joining these two nuclei in Fig. 4.35 (purple line) has a negative slope. This is consistent with deep-inelastic reactions.

An important aspect of Coulomb barriers is the fact that the formula used to calculate the barrier is empirical and the parameters come from a fit to ex-

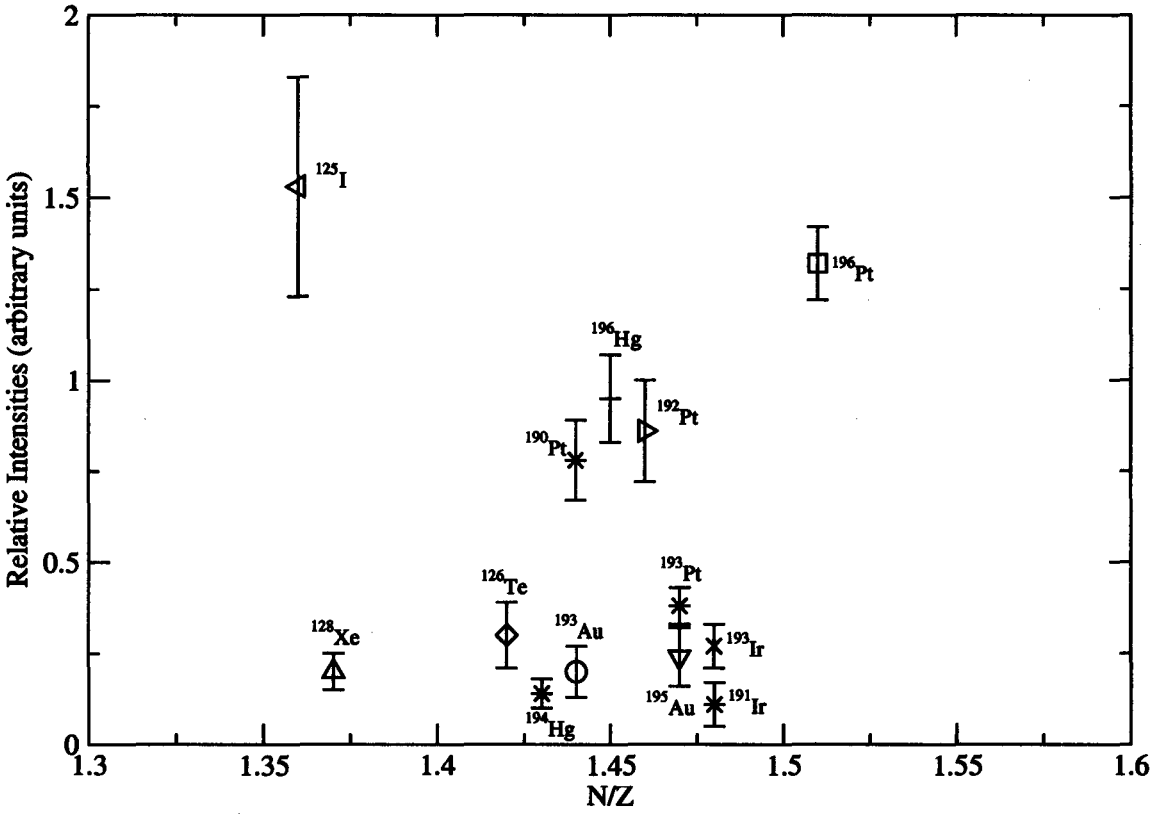

Figure 4.33: A plot of the N/Z values vs relative intensities for the second experiment (^{194}Pt + ^{127}I).

perimental data for much lighter systems. A simple program is available to calculate the "Bass barrier" which is frequently quoted for heavy systems, but was not used for this work [Bas74]. There are other formulae for calculating the Coulomb barrier. Eq. 4.15 is one of these which comes from other fits.

$$V_{Coul} = \frac{1.44 Z_p Z_t}{A_p^{\frac{1}{3}} + A_t^{\frac{1}{3}} + 3.5} \tag{4.15}$$

All these barrier calculations tend to give approximately the same results for "normal systems" i.e. S + Er or O + Sn, but they do not necessarily cope well or behave in the same way as each other when applied to heavier systems for which barriers often have not been measured and so which were not included

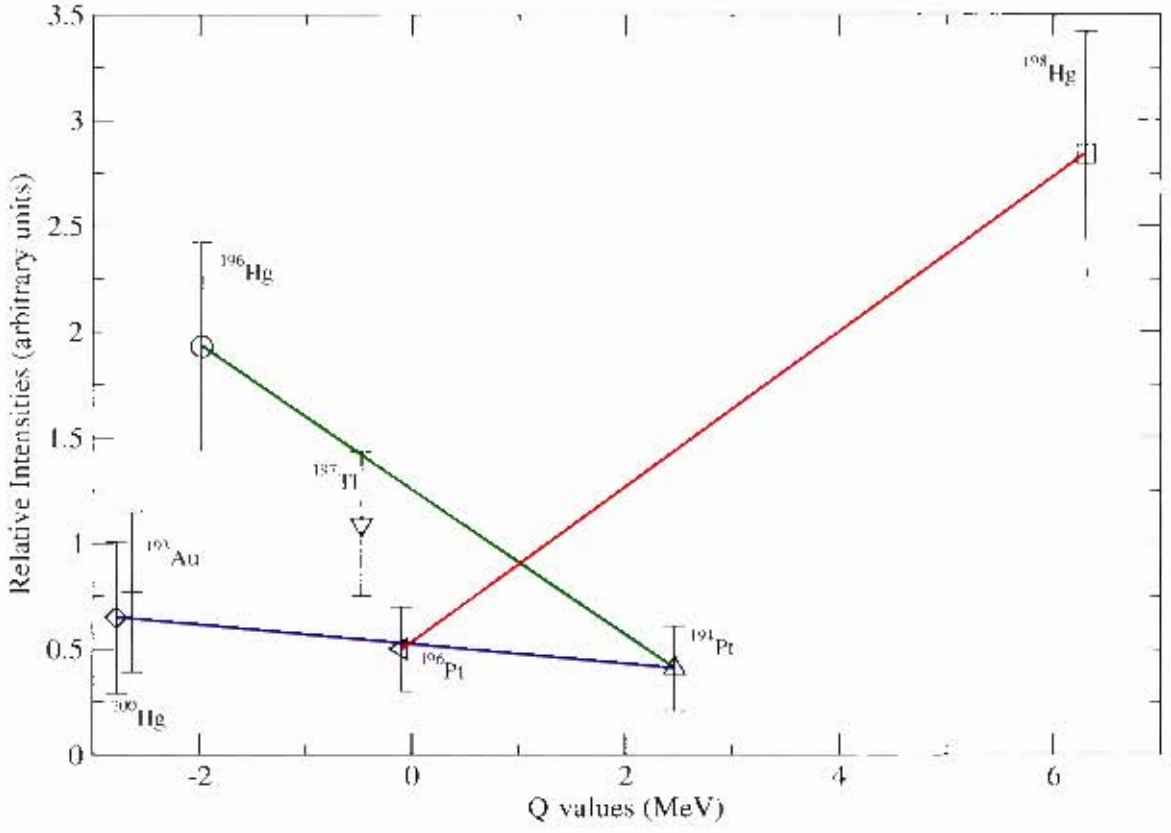

Figure 4.34: A plot of the Q-values vs relative intensities for the first experiment (^{197}Au + ^{127}I).

when making the original fit. One has to be cautious with the results one gets from whichever expression one uses [Wil02]. More measurements have been made for barrier distributions [Das98], and it appears that the standard expressions used over-estimate the barrier height for light systems but start to under-estimate for heavier ones. By the time we get to systems such as ^{197}Au + ^{127}I and ^{194}Pt + ^{127}I, the under-estimation may be important, but there are unfortunately no measurements for these heavy systems.

In the case of Wilson's experiment [Wil00], a Ni beam was used to bombard a Pb target. The Ni beam loses about 12 MeV/mg/cm^2 in the Pb target. This means

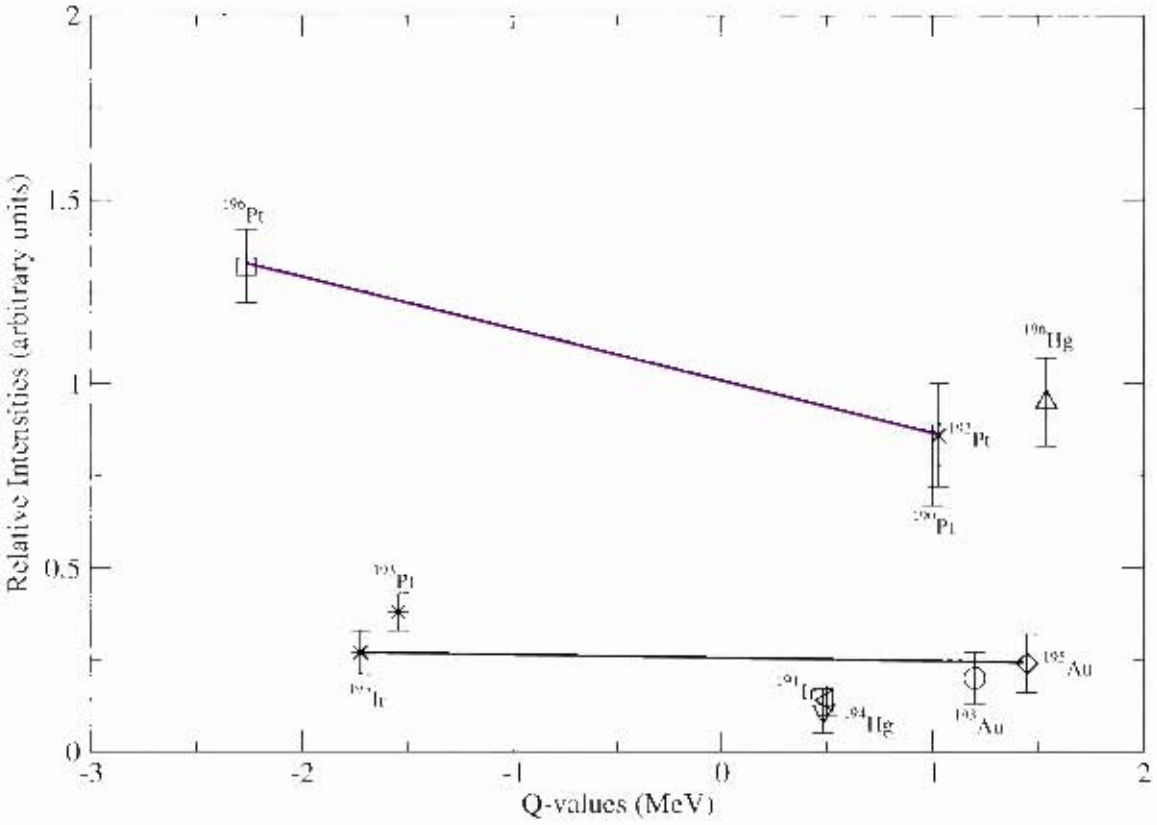

Figure 4.35: A plot of the Q-values vs relative intensities for the second experiment (^{194}Pt + ^{127}I).

that it penetrates approximately 4 mg/cm^2 before it reaches the Coulomb barrier. Hence the yields from above-barrier reactions are very significant. The Au and Pt targets are much better stoppers than Pb, and ^{127}I is much heavier than ^{64}Ni and has higher Z, so energy loss is significant. The ^{127}I beam penetrates slightly less than 2 mg/cm^2 of either Au or Pt before going below the barrier, assuming that the barrier is at 665 MeV. Hence there is relatively little yield from above-barrier reactions, and there will be a large contribution from Coulomb excitation. The advantage of Wilson and most others studying deep-inelastic reactions is that they have a beam energy at about 15 - 20 % above

the barrier and lose energy slower than in the present work. One can immediately see from Tables 4.1 and 4.2 that the GRAZING program calculations for σ_{th} are not at all in agreement with the extracted coincidence intensity values. The reasons are:

- In the GRAZING calculations, Polarollo generates the distribution of products of the reaction, whereas we measure the yields after these nuclei may have gone through a series of decay processes. Evaporation should be the most important process. If the product is formed at an excitation energy less than the neutron binding energy, no neutrons will be emitted. From the Q-values, one can in principle see whether there is enough energy for neutron evaporation.

- In the GRAZING program, pair transfers are not taken into consideration. It assumes that nucleons are transfered one at a time. Each transfer process is independent of the next. Hence for multi nucleon transfer channels, the cross-sections are calculated as successive one nucleon transfers. Pair transfers may be important, but are not included in the GRAZING treatment. The GRAZING program assumes a well defined incident energy and makes no allowance for energy loss due to target thickness. For these reasons, the GRAZING program may be inadequate in describing the present data.

When looking at the level schemes in Appendices 1 and 2, one will notice that the maximum spin populated is not very high (generally $\leq$10 $\hbar$). This does not mean that the theories described in Chapter 2 disagree with values obtained in the present work. The limitation of these theories is the fact that they are classical in nature, and should not be taken too literally. In most works involving these theories, there is a general but not precise agreement

between experimental results and theory. The precision is often a function of the experimental arrangement. For the first experiment, that is $^{197}Au + ^{127}I$, the theoretical values are: L_{max} = 178 $\hbar$, J_p = 23.54 $\hbar$ (rolling) and 13.67 $\hbar$ (sticking), J_t = 27.25 $\hbar$ (rolling) and 28.41 $\hbar$ (sticking).

For the second experiment, that is $^{194}Pt + ^{127}I$, L_{max} = 175.92 $\hbar$, J_p = 23.36 $\hbar$ (rolling) and 13.69 $\hbar$ (sticking), J_t = 26.90 $\hbar$ (rolling), 27.74 $\hbar$ (sticking). The spins obtained in this work are much lower than for either the rolling or the sticking predicted values. This can be attributed to a number of reasons:

- The process could be a quasi-elastic, grazing collision to which the theories do not apply.

- It could also be that the lifetimes of the higher spin states are so short, that in a thick target, the γ-ray lines are smeared out due to the Doppler effect. The nucleus is still slowing down in the target when the γ rays are emitted from higher spin states. It is therefore difficult to conclude what the highest spin populated in the reaction was.

- The beam energy constrained by the cyclotron performance was only $\approx$ 9.5% above the barrier. These experiments are usually attempted at 15% or more above the barrier. The barrier might also be underestimated as explained earlier.

- In the experimental arrangement, we did not have timing information or a high-fold selectivity.

Chapter 5

CONCLUSIONS

The questions raised in Chapter I (Introduction) will be answered now.

- Question: How are the transfers affected by whether there is an unpaired proton in the target?

  Answer: The ^{197}Au target has an unpaired proton and as can be seen from the intensity values in Table 4.1, the one proton transfer intensity has a value of 2.84 (arbitrary units) to produce ^{198}Hg which is the strongest transfer channel. No pure two proton transfer could be observed. The majority of transfers involve either one or two protons, with an even number of neutrons. No single neutron transfers were observed for the first experiment. The +1p-2n and +2p-2n reaction products could be observed, and the ratio of their intensities shows that the +1p-2n is favoured over the +2p-2n by a factor of 1.77 $\pm$ 0.69. In the ^{194}Pt experiment, the +1p-2n reaction is favoured over the +2p-2n reaction by a factor of 1.42 $\pm$ 0.64. Hence, the difference between the two experiments for these reactions is not significant, whereas the GRAZING program predicts a ratio of 5 for the first experiment, and a ratio of 20 for the second experiment. Thus, these values disagree significantly with relative yields inferred from the experimental intensity ratios. In the ^{194}Pt experiment, pure 1p and 2p transfers could be observed, and the ratio of the intensities favours the proton pair transfer by a factor of 3.96 $\pm$ 1.43. The GRAZING calculations favour the single proton transfer over the proton pair transfer by

a factor of 8.33. Hence, the difference between the GRAZING prediction and the experimental value is very significant. Also in the ^{194}Pt experiment, it is interesting to note that the +2n and -2n intensity ratio is 0.67 ± 0.09, whereas the GRAZING predictions show that there is no preference for gaining or losing a pair of neutrons. In the ^{197}Au experiment, it is interesting to note that the intensity ratio for the +1p transfer over the -1p transfer is 5.68 ± 1.39. It is an indication that ^{197}Au will tend to gain a proton from the beam rather than losing one. This is also consistent with the Q-values shown in Table 4.1, where the Q-value for +1p is 6.310 ± 0.006 and the Q-value for -1p is -0.101 ± 0.005. The GRAZING program predicts that for the ^{197}Au experiment, the ratio for the +1p and -1p reaction products is 4, which is in reasonable agreement with the experimental value of 5.68 ± 1.39. In the ^{194}Pt experiment, the ratio of the +1p and -1p reaction products is 0.89 ± 0.36. This may be due to the fact that the protons ^{194}Pt are fully paired. In Table 4.2, the Q-value for the +1p transfer is 1.450 ± 0.004 and the Q-value for the -1p transfer is -1.722 ± 0.003. Hence, in contrast to the ^{197}Au case, the difference in Q-values is relatively small. However, GRAZING predicts that the ratio of +1p and -1p is 5. Thus, the difference between the experimental value and that predicted by the GRAZING program is significant in this case.

- Question: Are pairs of nucleons preferentially exchanged due to the quantum nature of the nuclear fluid?

  Answer: The two proton transfer over the one proton transfer for the second experiment (^{194}Pt + ^{127}I) was favoured by a factor of 3.96 ± 1.43. This was found from the measured intensities shown in Table 4.2. However the GRAZING program predicts that the cross-section for a two proton transfer is a factor of ten lower than for a single proton transfer. Further-

more, the ratio of the intensities for the -2n transfer over the -1n transfer is 2.26 ± 0.51. The GRAZING program prediction for the ratio of the -2n over the -1n transfer is 0.075. Hence, the ratio of the experimental intensities divided by the ratio of the cross-sections predicted by GRAZING is $\simeq$ 30. This suggests that pair transfers, particularly for neutrons, are preferred for the ^{194}Pt target. The same conclusion could not be drawn for the first experiment (^{197}Au + ^{127}I) for proton transfers, because no pure 2p transfer from the target to the beam was observed. Also, no single neutron transfers were observed, whereas four target-like products corresponding to either the gain or loss of a pair of neutrons were identified. Three of these products include a transfer of a pair of neutrons from the ^{197}Au target to the beam. Also, the population of ^{193}Au may be interpreted as the transfer of two pairs of neutrons to the beam. Hence, there are indications that neutron pair transfers to the beam are favoured for the ^{197}Au target.

- Question: Are nucleons exchanged in an entirely statistical manner?
  Answer: For the ^{197}Au experiment, the one proton transfer has the highest intensity and has produced ^{198}Hg. The second highest intensity was for the transfer of one proton and the loss of two neutrons to produce ^{196}Hg. As can be seen in Fig. 4.34, the line joining the ^{196}Hg and ^{194}Pt nuclei indicates that the transfer of one proton to and from the ^{197}Au target is deep-inelastic in character. However as discussed in the point above, in the second experiment a proton pair transfer is favoured over one proton transfer by a factor of 3.96 ± 1.43. As can be seen from Fig. 4.35, the line joining the ^{196}Pt and ^{192}Pt nuclei shows that the ± 2n transfers are consistent with deep-inelastic processes. Thus, there is no evidence that the nucleons are exchanged in an entirely statistical manner.

- Question: Do such collisions show any preference for populating any particular shape?

  Answer: ^{197}Au, ^{194}Pt and ^{127}I are slightly oblate with β values of -0.131, -0.130 and -0.148, respectively [T2l]. With the exception of ^{191}Ir, ^{193}Ir and ^{128}Xe which have a positive quadrupole deformation (prolate), all the other reaction products are oblate with β values ranging from -0.130 to -0.156. Therefore, as protons are gained, the target-like fragments tend to be oblate, whereas ^{191}Ir and ^{193}Ir, which correspond to the loss of one proton from ^{194}Pt, are prolate. The oblate deformations of the targets are a consequence of the proton numbers (Z = 79 and 78) approaching the Z = 82 closed shell. Hence, as protons are transfered to the targets, the oblate deformations decrease. Conversely, removing a proton from ^{194}Pt populates Ir (Z = 77) nuclei, which are weakly prolate.

5.1 Further work

Having discussed the results in the previous chapter and answering these questions does not mean that one should stop here in terms of this type of experiment. The first extension of this work would be to repeat the same experiment but at energies of about 20% above the Coulomb barrier. As discussed in the previous chapter, this would enable one to see more reaction products at higher spins. One should also obtain timing information.

- If a thin target was used when studying particle-γ coincidence, it would be appropriate to compare results with the predictions of the GRAZING program. Of course it would mean that Doppler shifts would have to be calculated. Corrections from a proper determination of the kinematics of the beam-like and/or target-like products would need to be applied. The products do not simply travel in the direction of the beam.

- It would also be interesting to study reactions with a beam and/or target such as $^{127}I + ^{198}Pt$, or $^{128}Xe + ^{194}Pt$ or ^{197}Au, $^{136}Xe + ^{198}Pt$ or ^{197}Au. These experiments should be studied at the present energy of 730 MeV which is approximately 9% above the barrier and then at about 20% above the barrier, again using thick and thin targets for every case.

- It would be interesting to study reactions of the following type: a prolate nucleus bombarding an oblate target. This reaction would enable one to see if any particular shape would be populated.

The above shows that there is still a lot to be done in this fascinating field. The experiments presented in this thesis constitute the first such measurements with the AFRODITE array in the field of heavy ion induced transfer reactions.

Chapter 6

REFERENCES

- [Abd87] Y. Abdelrahman, J.L. Durell, W. Gelletly, W.R. Phillips, I. Ahmad, F. Holzmann, R.V.F. Janssens, T.L. Khoo, W.C. Ma, M.W. Drigert, Phys. Lett. B199 (1987), p 504

- [Asz99] S.J. Asztalos, I.Y. Lee, K. Vetter, B. Cederwall, R.M. Clark, M.A. Deleplanque, R.M. Diamond, P. Fallon, K. Jing, L. Phair, A.O. Macchiavelli, J.O. Rasmussen, F.S. Stephens, G.J. Wozniak, J.A. Becker, L.A. Bernstein, D.P. MacNabb, P.F. Hua, D.G. Sarantites, J.X. Saladin, C.H. Yu, J.A. Cizewski, R. Donangelo, Phys. Rev. C60 (1999), 044307

- [Asz00] S.J. Asztalos, I.Y. Lee, K. Vetter, B. Cederwall, R.M. Clark, M.A. Deleplanque, R.M. Diamond, P. Fallon, K. Jing, L. Phair, A.O. Macchiavelli, J.O. Rasmussen, F.S. Stephens, G.J. Wozniak, J.A. Becker, L.A. Bernstein, D.P. MacNabb, P.F. Hua, D.G. Sarantites, J.X. Saladin, C.H. Yu, J.A. Cizewski, Phys. Rev. C61 (2000), 014602

- [Bas74] R. Bass, Nucl. Phys. A231, (1974), p 45

- [Bas80] R. Bass, Nuclear Reactions with Heavy Ions (1980), Springer-Verlag

- [Bea96] C.W. Beausang, J. Simpson, J. Phys. G: Nucl. Part. Phys. 22, (1996), p 527

- [Bec94] F.A. Beck, P.J. Nolan, D.B. Fossan, Ann. Rev. Nuc. Part. Sci. 44, (1994), p 561

- [Boc77] R. Bock, B. Fischer, A. Gobbi, K. Hildenbrand, W. Kohl, U. Lynen, I. Rode, H. Stelzer, G. Auger, J. Galin, J.M. Lagrange, B.B. Back, R. Albrecht, Nukleonika 22 (1977), p 529

- [Boc82] R. Bock, Y.T. Chu, M. Dakowski, A. Gobbi, E. Grosse, A. Olmi, H. Sann, D. Schwalm, U. Lynen, W. Muller, S. Bjornholm, H. Esbensen, W. Wolfli, E. Morenzoni, Nucl. Phys. A388 (1982), p 334

- [Bro90] R. Broda, M.A. Quader, P.J. Daly, R.V.F. Janssens, T.L. Khoo, W.C. Ma, M.W. Drigert, Phys. Lett. B251, (1990), p 245

- [Bro91] R.A. Broglia, A. Winther, Heavy Ion Reactions, Frontiers of Physics, Vol. 84, Parts 1 and 2, Addison-Wesley (1991), ISBN 0201513927

- [But98] P.A. Butler, J.F.C. Cocks, P.T. Greenless, Proc. Int. Conf. on Fission and properties of Neutron-Rich Nuclei (World Scientific, ed. Hamilton, Philips, Carter) (1998), p 28

- [Coc00] J.F.C. Cocks, P.A. Butler, K.J. Cann, G.D. Jones, J.F. Smith, P.M. Jones, R. Julin, S. Juutinen, D. Muller, M. Piiparinen, A. Savelius, R. Broda, B. Fornal, I. Ahmad, D.J. Blumenthal, M.P. Carpenter, B. Crowell, R.V.F. Janssens, T.L. Khoo, T.Lauritsen, D. Nisius, S. Asztalos, R.M. Clark, M.A. Deleplanque, R.M. Diamond, P. Fallon, I.Y. Lee, A.O. Macchiavelli, R.W. MacLeod, F.S. Stephens, P. Bhattacharyya, C.T. Zhang, J. Phys. G 26 (2000), p 23

- [Cor01] L. Corradi, A.M. Vinodkumar, A.M. Stefanini, D. Ackerman, M. Trotta, Phys. Rev. C63, (2001), 021601

- [Dal95] P.J. Daly, C.T. Zhang, R.H. Mayer, D.T. Nisius, P. Bhattacharyya, I.P. Bearden, M. Sferrazza, Z.W. Grabowski B.Fornal, R. Broda, W. Krolas, T. Pawlat, I. Ahmad, M.P. Carpenter, R.V.F. Janssens, T.L. Khoo, T. Lauritsen, D. Bazzacco, S. Lunardi, C. Rossi-Alvarez, G. De Angelis and GASP Collaboration. 5th International Spring Seminar on Nuclear Physics. New Perspectives Proceedings in Nuclear Structure. Ravello (1995), p 91. Ed. by A. Covello, World Scientific Press, Singapore (1996)

- [Das94] C.H. Dasso, G. Pollarolo, A. Winther, Phys. Rev. Lett. 73, (1994), p 1907

- [Das98] M. Dasgupta, D.J. Hinde, N. Rowley, A.M. Stefanini, Annu. Rev. Nucl. Part. Sci. (48), (1998), p 401

- [Dra96] G.D. Dracoulis, Trends in nuclear structure with heavy ions. Nucl. Instr. Meth. A 382, (1996), p 1

- [Duc99] G. Duchêne, F.A. Beck, P.J. Twin, G. de France, D. Curien, L. Han, C.W. Beausang, M.A. Bentley, P.J. Nolan, J. Simpson, Nucl. Instr. Meth. A 432 (1999), p 90

- [FK84] H. Freiesleben, J.V. Kratz, Phys. Rep. 106 (1984), p 1

- [Fun97] F. Funke, G.Wirth, J.V. Kratz, W. Bruchle, F. Wo, K. Summerer, Z.Phys.A357, (1997), p 303

- [Gav80] A. Gavron, Phys. Rev. C21, (1980), p 230

- [Gav93] A. Gavron, Computational Nuclear Physics 2, Nuclear Reactions, Springer-Verlag New York, Inc, (1993), p 108

- [Gob80] A. Gobbi and W. Norenberg, Heavy Ion Collisions, vol. 2, North Holland Publishing Company (1980)

- [Gol79] L.J.B. Goldfarb, W. Von Oertzen, in Heavy Ion Collisions, vol. 1, North Holland Publishing Company (1979)

- [Hib93] I.M. Hibbert, PhD Thesis, University of Manchester (1993)

- [Hot90] M.A.C. Hotchkis, J.L. Durell, J.B. Fitzgerald, A.S. Mowbray, W.R. Phillips, I. Ahmad, M.P. Carpenter, R.V.F. Janssens, T.L. Khoo, E.F. Moore, L.R. Morss, Ph. Benet, D. Ye, Phys. Rev. Lett. 64 (1990), p 3123

- [Hot91] M.A.C. Hotchkis, J.L. Durell, J.B. Fitzgerald, A.S. Mowbray, W.R. Phillips, I. Ahmad, M.P. Carpenter, R.V.F. Janssens, T.L. Khoo, E.F. Moore, L.R. Morss, Ph. Benet, D. Ye, Nucl. Phys. A530 (1991), p 111

- [Iel] http://ie.lbl.gov/ensdf

- [Jon95] P.M. Jones, L. Wei, F.A. Beck, P.A. Butler, T. Byrski, G. Duchêne, G. de France, F. Hannachi, G.D. Jones, B. Kharraja, Nucl. Instr. Meth. A362, (1995), p 556

- [Kau59] R. Kaufman and R. Wolfgang, Phys. Rev. Lett. 3 (1959) p 232

- [Kau61] R. Kaufman and R. Wolfgang, Phys. Rev. 121 (1961), p 192

- [Kau61b] R. Kaufman and R. Wolfgang, Phys. Rev. 121 (1961), p 206

- [Kra88] K.S. Krane, Introductory Nuclear Physics, John Wiley and Sons, New York, (1988)

- [Krat81] J.V. Kratz, J.Poitou, W. Bruchle, H. Gaggeler, M. Schadel, G. Wirth, R. Lucas, Nucl. Phys. A357 (1981), p 437

- [Kro03] W. Krolas et al., Nucl. Phys. A724 (2003), p 289

- [Kwi01] P.Kwinana, MSc Thesis, UWC, 2001

- [Law97] J.J. Lawrie, AUTOCAL-NEW, Software program on VAX, iThemba LABS (1997)

- [Lee90] I.Y. Lee, Nuclear Physics A550 (1990), p 641c

- [Lee97] I.Y. Lee, S. Asztalos, M.A. Deleplanque, B. Cederwall, R.M. Diamond, P. Fallon, A.O. Macchiavelli, L. Phair, F.S. Stephens, G.J. Wozniak, S.G. Frauendorf, J.A. Becker, E.A. Henry, P.F. Hua, D.G. Sarantites, J.X. Saladin, C.H. Yu, Phys. Rev. C 56, pp 753-759 (1997)

- [Leh96] G. Lhersonneau, P. Dendooven, G. Canchel, J. Huikari, P. Jardin, A. Jokinen, V. Kolhinen, C. Lau, L. Lebreton, A.C. Mueller, Nucl. Instr. Meth. A373 (1996), p 415

- [Lil90] J.S. Lilley, Nuclear Physics News, Vol.1 (2), (1990)

- [Mab03] G.K. Mabala, PhD Thesis, University of Cape Town, (2003)

- [Mor81] L.G. Moretto and R.P. Schmitt, Rep. Prog. Phys. 44 (1981) p 533

- [New98] R.T. Newman, J.J. Lawrie, B.R.S. Babu, M.S. Fetea, S.V. Fortsch, S. Naguleswaran, J.V. Pilcher, D.A. Rave, C. Rigollet, J.F. Sharpey -Schafer, C.J. Stevens, F.D. Smit, G.F. Steyn, C.V. Wikner, D.G. Aschman, R. Beetge, R.W. Fearick, G.K. Mabala, S. Murray, D.G. Roux , W. Whittaker and N.J.

Ncapayi, Proceedings of Balkan School on Nuclear Physics, September 1-10, 1998 Baltalimani, Istanbul, Turkey, Balkan Physics Letters, 182 (1998).

- [Nnd] http://www.nndc.bnl.gov
- [NSP] http://ns.ph.liv.ac.uk/MTsort/manual
- [Pil92] J.V. Pilcher, NAC Internal Report, National Accelerator Centre, Faure (1992)
- [Pol99] G. Pollarolo, Pramana J. of Phys. 53 (3), (1999), p 473
- [Pol02] http://www.to.infn.it/~nanni~/
- [Qui93] A.B. Quint, J.G. Keller, V. Ninov, K. Poppensieker, W. Reisdorf, K.H. Schmidt, Z. Phys. A346 (1993), p 119
- [Rad95] D.C. Radford, Nucl. Instr. Meth. A361, p 306 (1995)
- [Rad95a] D.C. Radford, Nucl. Instr. Meth. A361, p 297 (1995)
- [Reg97] P.H. Regan, A.D. Yamamoto, F.R. Xu, A.O. Macchiavelli, D. Cline, J.F. Smith, S.J. Freeman, J.J. Valiente-Dobon, K. Andgren, R.S. Chakrawarthy, M. Cromaz, P. Fallon, W. Gelletly, A. Gorgen, A. Hayes, H. Hua, S.D. Langdown, I-Y. Lee, C.J. Pearson, Zs Podolyak, R. Teng, C. Wheldon, Phys. Rev. C55 (1997), p 2305
- [Reg00] P.H. Regan, Post Graduate Nuclear Experimental Techniques Course Notes, University of Surrey (2000), http://www.phy.surrey.ac.uk/~phs1pr/lecture-notes/

- [Reg03] P.H. Regan, A.D. Yamamoto, F.R. Xu, C.Y. Wu, A.O. Macchiavelli, D. Cline, J.F. Smith, S.J. Freeman, J.J. Valiente-Dobon, K. Andgren, R.S. Chakrawarthy, M. Cromaz, P. Fallon, W. Gelletly, A. Gorgen, A. Hayes, H. Hua, S.D. Langdown, I-Y. Lee, C.J. Pearson, Zs. Podolyak, R.Teng, C. Wheldon, Phys. Rev. C68 (2003), 044313

- [Reg04] P.H. Regan, J.J. Valiente-Dobon, C. Wheldon, C.Y. Wu, J. Smith, D. Cline, R.S. Chacrawarthy, R. Chapman, M. Cromaz, P. Fallon, S.J. Freeman, A. Gorgen, W. Gelletly, A. Hayes, H. Hua, S.D. Langdown, I-Y. Lee, Y. Liang, A.O. Macchiavelli, C.J. Pearson, Zs. Podolyak, R. Teng, D. Ward, D.D. Warner, A.D. Yamamoto, Laser Phys. Lett. 1, (2004), p 317

- [Rej97] M. Rejmund, K.H. Maier, R. Broda, B. Fornal, M. Lach, J. Wresinski, J. Blomqvist, A. Gadea, J. Gerl, M. Gorska, H. Grawe, M. Kaspar, H. Schaffner, C. Schlegel, R. Schubart, H.J. Wollersheim, Z. Phys A359, (1997), p 243

- [Rej98] M. Rejmund, K.H. Maier, R. Broda, B. Fornal, M. Lach, J. Wresinski, J. Blomqvist, A. Gadea, J. Gerl, M. Gorska, H. Grawe, M. Kaspar, H. Schaffner, C. Schlegel, R. Schubart, H.J. Wollersheim, Eur.J. Phys. A1, (1998), p 261

- [Rou01] D.G. Roux, PhD Thesis, University of Cape Town, (2001)

- [Row91] N. Rowley, G.R. Satchler, P.H. Stelson, Phys. Lett. B254, (1991), p 25

- [Sch84] W.U. Schroder and J.R. Huizenga, Treatise on Heavy-Ion Science, Vol.2, Chapter 3, edited by D.A. Bromley (1984) Plenum Press

- [Sha88] J.F. Sharpey-Schafer and J. Simpson, Prog. in Part. and Nucl. Phys. 21, (1988), p 293

- [She99] S.L. Shepherd, P.J. Nolan, D.M. Cullen, D.E. Applebe, J. Simpson, J. Gerl, M. Kaspar, A. Kleinboehl, I. Peter, M. Rejmund, H. Schaffner, C. Schlegel, G. de France, Nucl. Instr. Meth. A434 (1999), p 373

- [Sim00] J. Simpson, Heavy Ion Physics 11 (2000), p 159

- [Tak88] H. Takai, C.N. Knott, D.F. Winchell, J.X. Saladin, M.S. Kaplan, L. de Faro, I-Y. Lee, O. Dietzach, Phys. Rev C38 (1988), p 1247

- [T2l] http://t2.lanl.gov/data/map.html

- [Val04] J.J. Valiente-Dobon, P.H. Regan, C. Wheldon, C.Y. Wu, N. Yoshinaga, K. Higashiyama, J.F. Smith, D. Cline, R.S. Chakrawarthy, R. Chapman, M. Cromaz, P. Fallon, S.J. Freeman, A. Gorgen, W. Gelettly, A. Hayes, H. Hua, S.D. Langdown, I-Y. Lee, X. Liang, A.O. Macchiavelli, C.J. Pearson, Zs. Podolyak, G. Sletten, R. Teng, D. Ward, D.D. Warner, A.D. Yamamoto, Phys. Rev. C69 (2004), 024316

- [Wil00] A.N. Wilson, C.W.Beausang, N.Azmal, D.E. Appelbe, S.Asztalos, P.A. Butler, R.M. Clark, P. Fallon, A.O. Macchiavelli, Europ. Phys. J. A9, (2000), p 183

- [Win90] A. Winther, Fisika 22, (1990), p 41

- [Win94] A. Winther, Nucl. Phys. A572, (1994), p 191

- [Win95] A. Winther, Nucl. Phys. A594, (1995), p 203

Appendix A

LEVEL SCHEMES FOR THE FIRST EXPERIMENT

In the first appendix, the level schemes for the first experiment are displayed. These level schemes are known from many sources and were confirmed from the spectra displayed in Chapter 4 even though not very high spins were reached. The only source of reference consulted for the level schemes in this Appendix and the next one are from the ENSDF (Evaluated Nuclear Structure Data File) at NNDC (National Nuclear Data Center) located at the Brookahaven National Laboratory web site [Nnd].

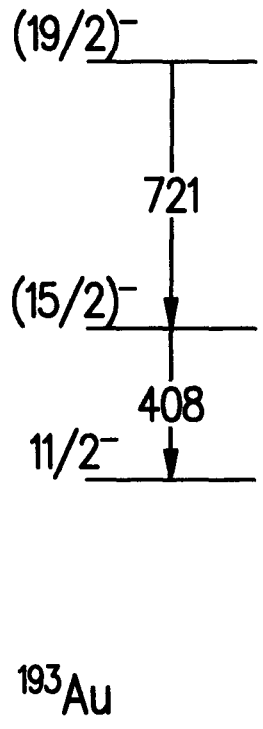

Figure A.1: Level scheme for ^{193}Au.

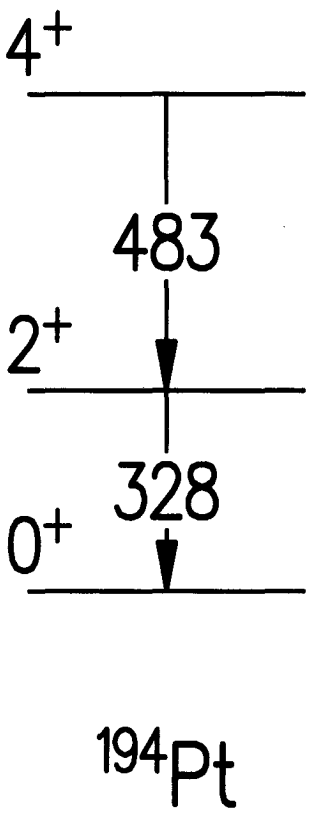

Figure A.2: Level scheme for ^{194}Pt.

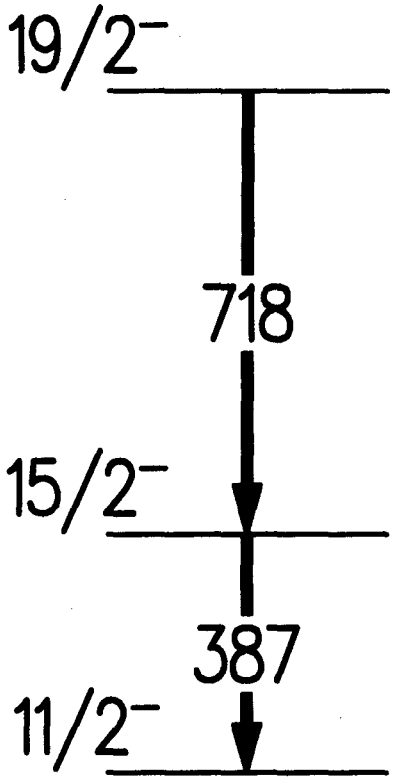

^{195}Au

Figure A.3: Level scheme for ^{195}Au.

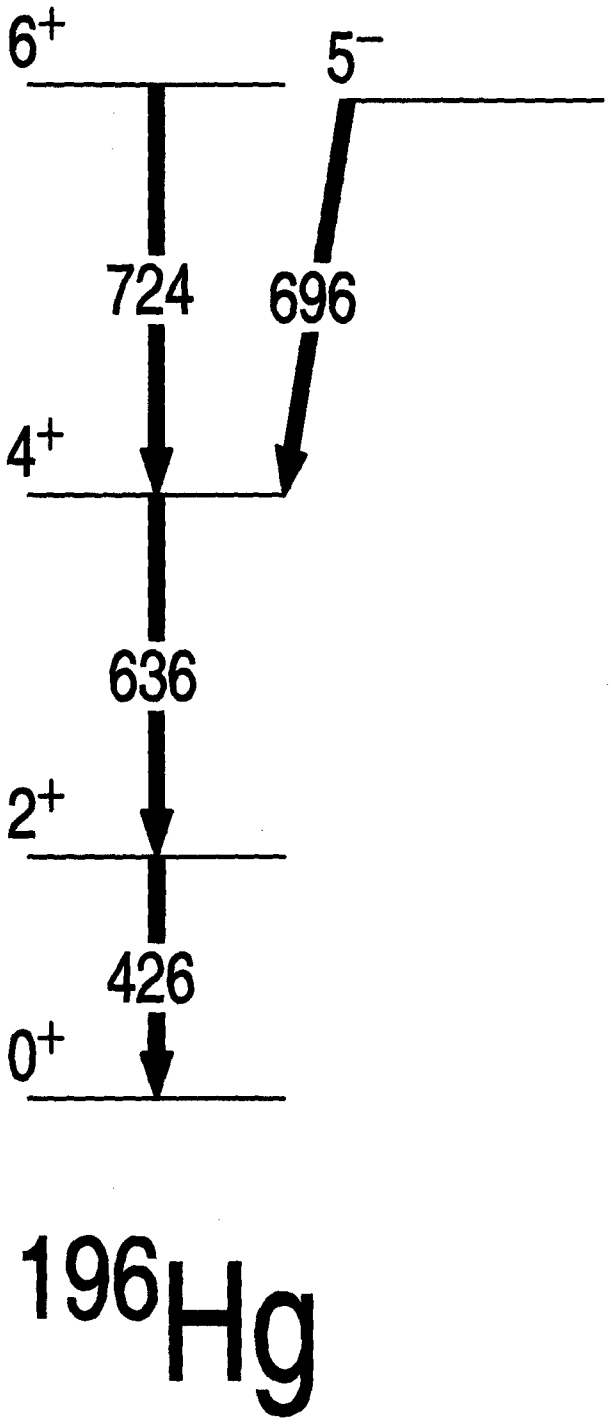

Figure A.4: Level scheme for ^{196}Hg.

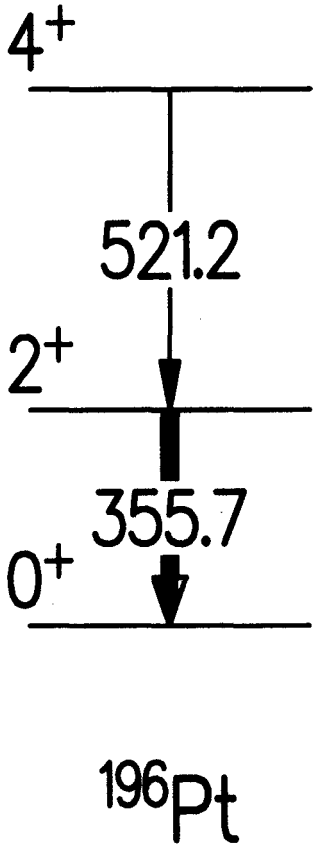

Figure A.5: Level scheme for ^{196}Pt.

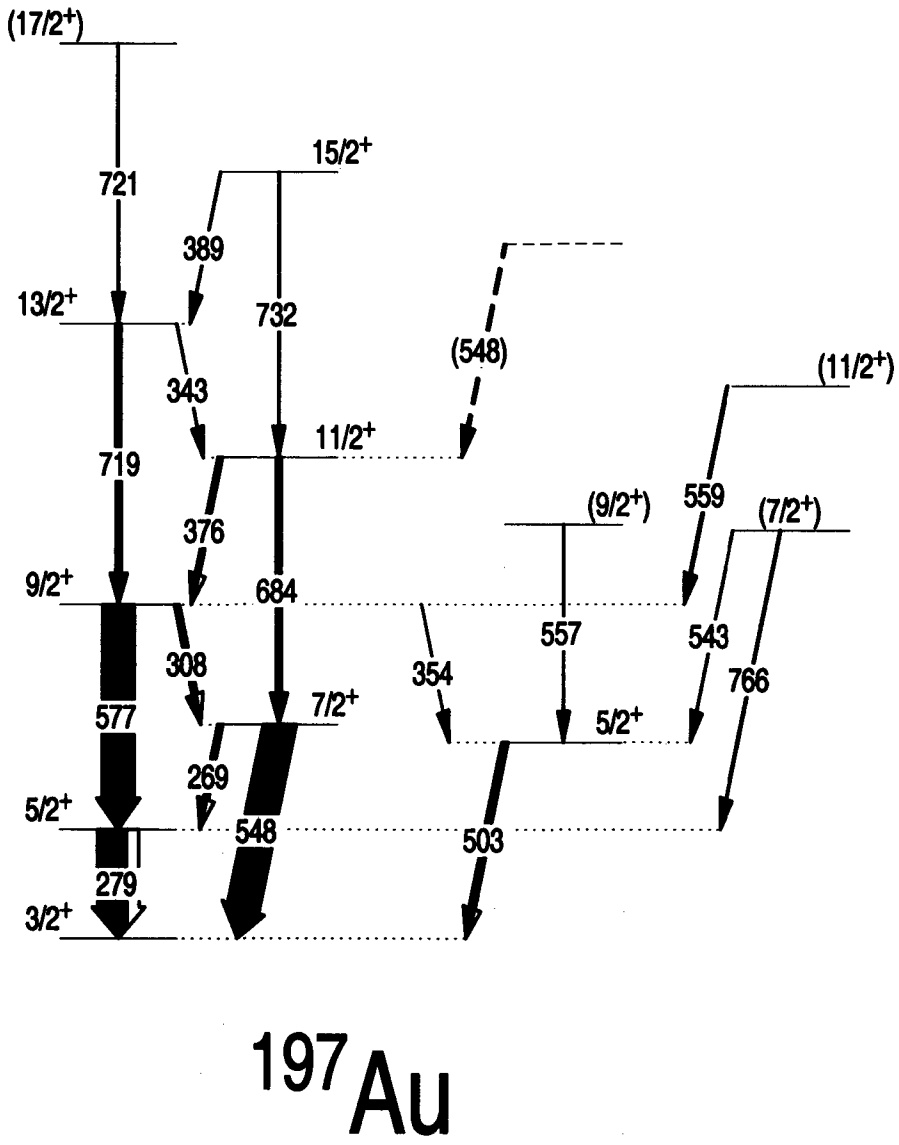

Figure A.6: Level scheme for ^{197}Au.

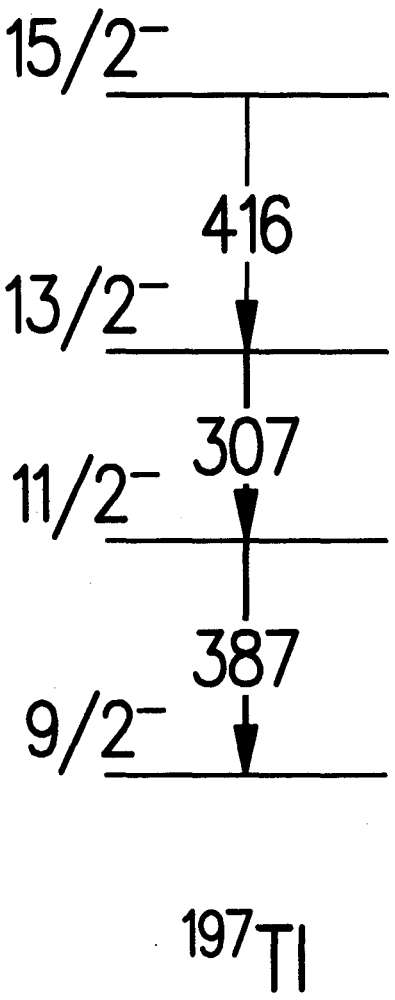

Figure A.7: Level scheme for ^{197}Tl.

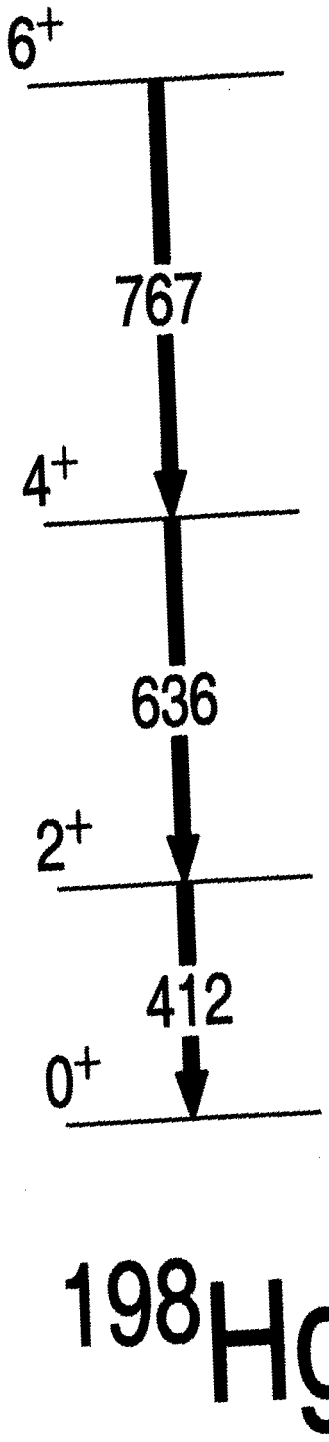

Figure A.8: Level scheme for ^{198}Hg.

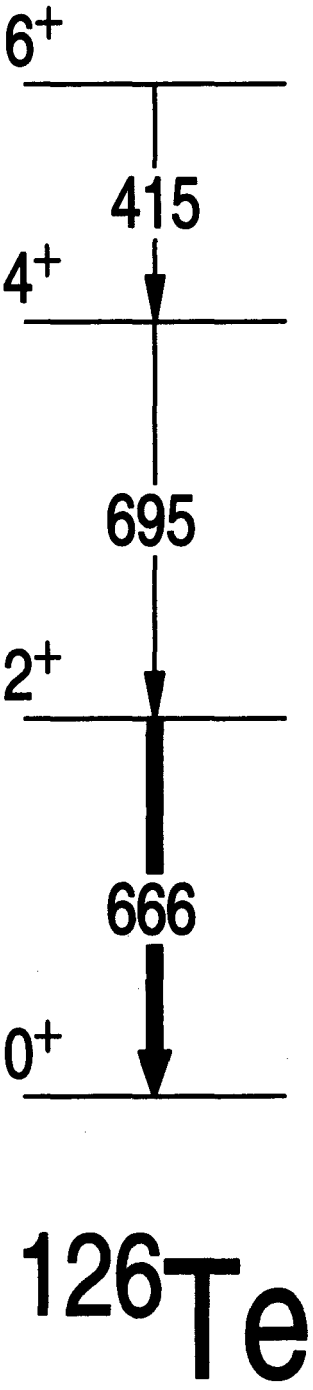

Figure A.9: Level scheme for ^{126}Te.

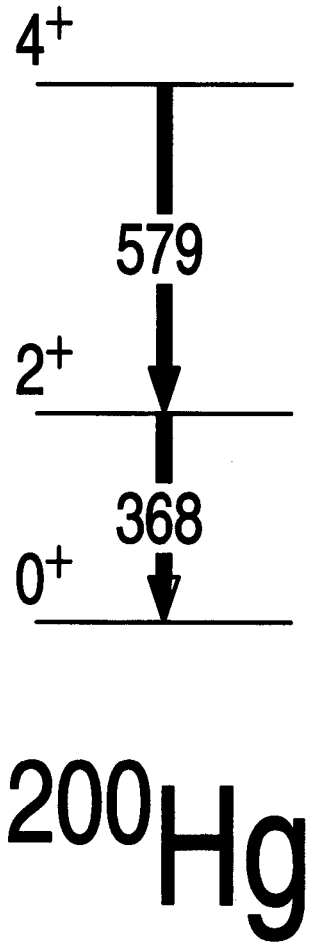

Figure A.10: Level scheme for ^{200}Hg.

Appendix B

LEVEL SCHEMES FOR SECOND EXPERIMENT

In the second appendix, the level schemes corresponding to the spectra in Chapter 4 are displayed. The level schemes apply to the second experiment.

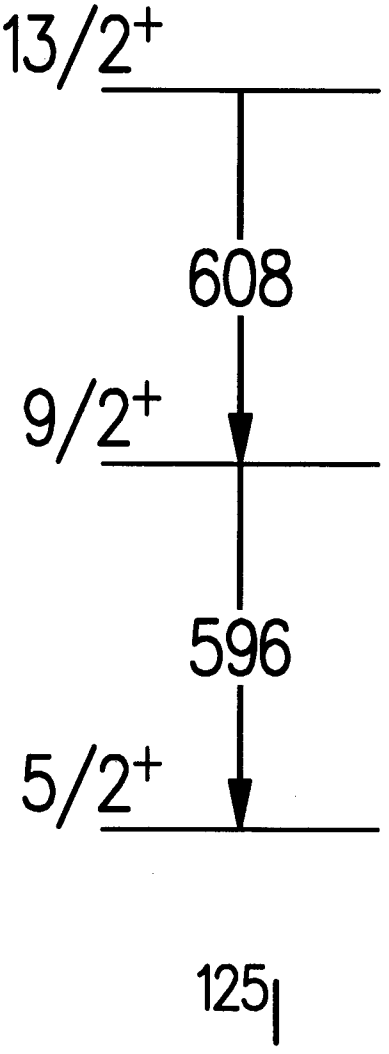

Figure B.1: Level scheme for ^{125}I.

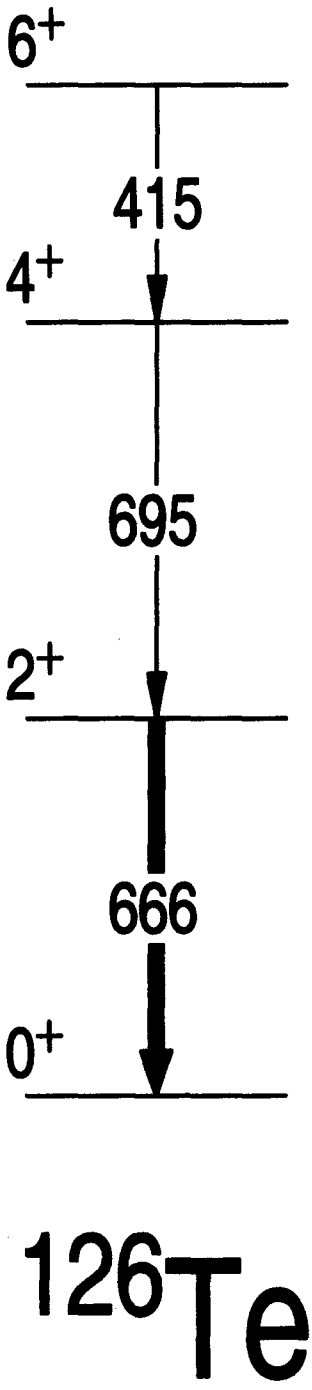

Figure B.2: Level scheme for ^{126}Te.

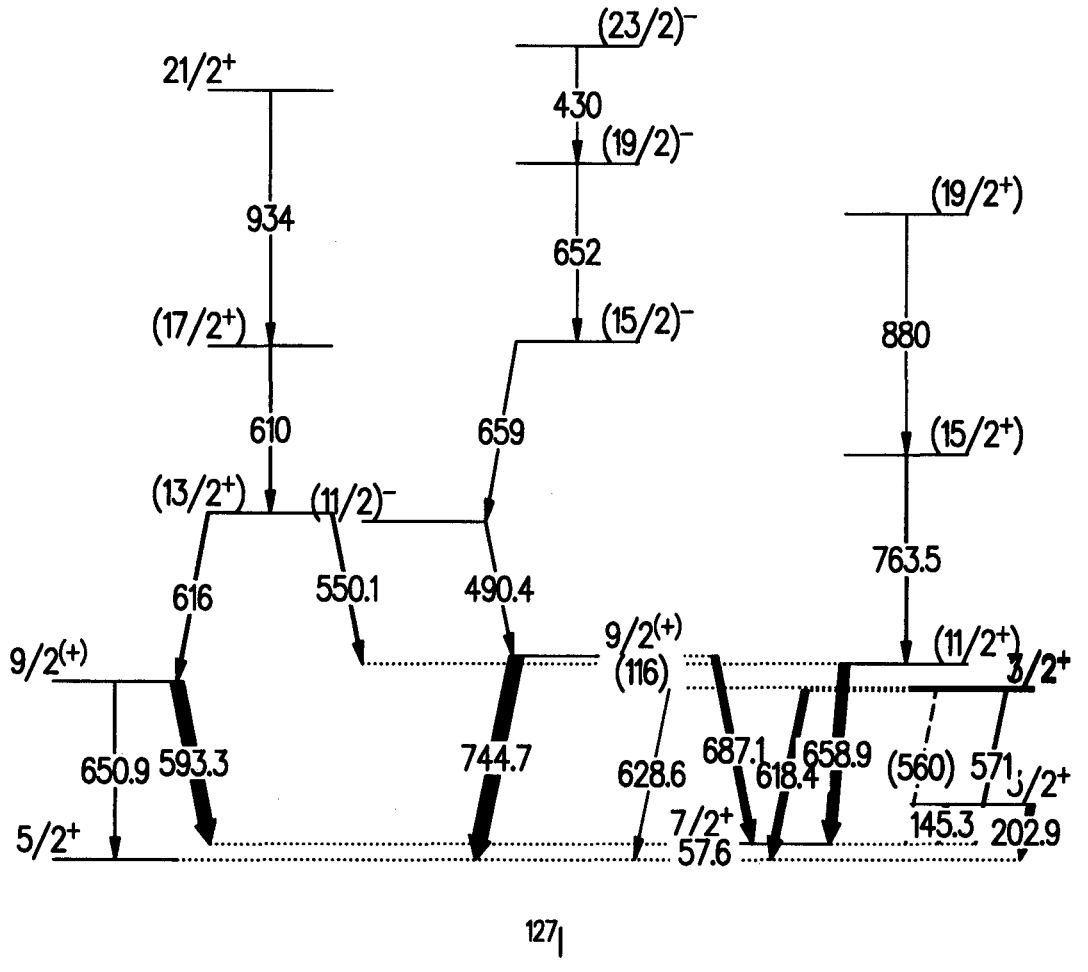

Figure B.3: Level scheme for ^{127}I.

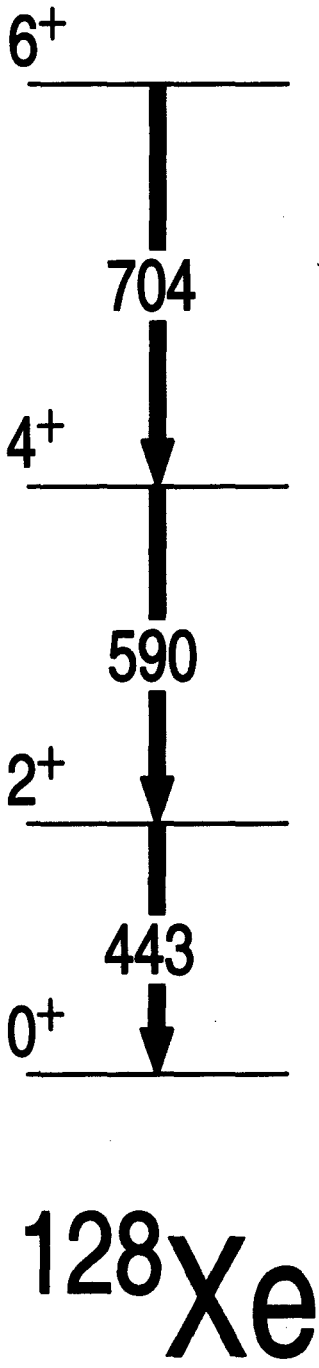

Figure B.4: Level scheme for ^{128}Xe.

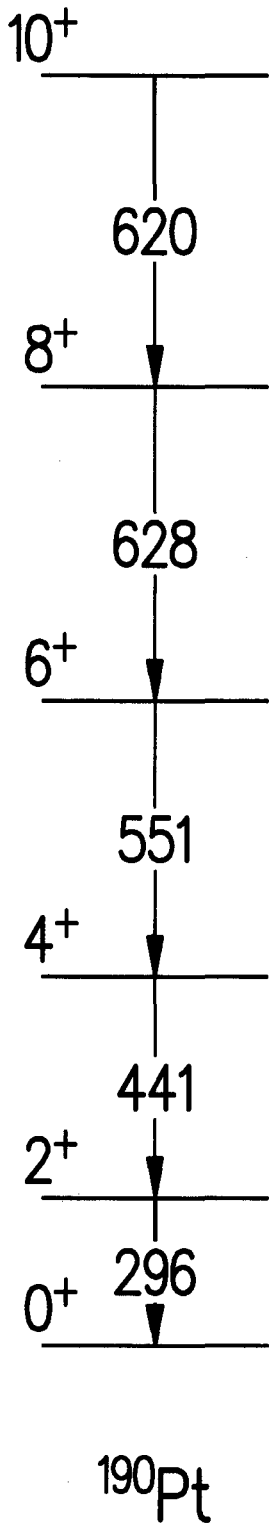

Figure B.5: Level scheme for ^{190}Pt.

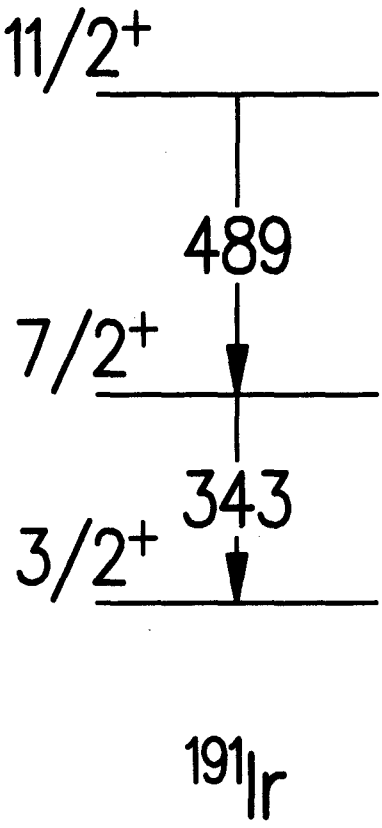

Figure B.6: Level scheme for ^{191}Ir.

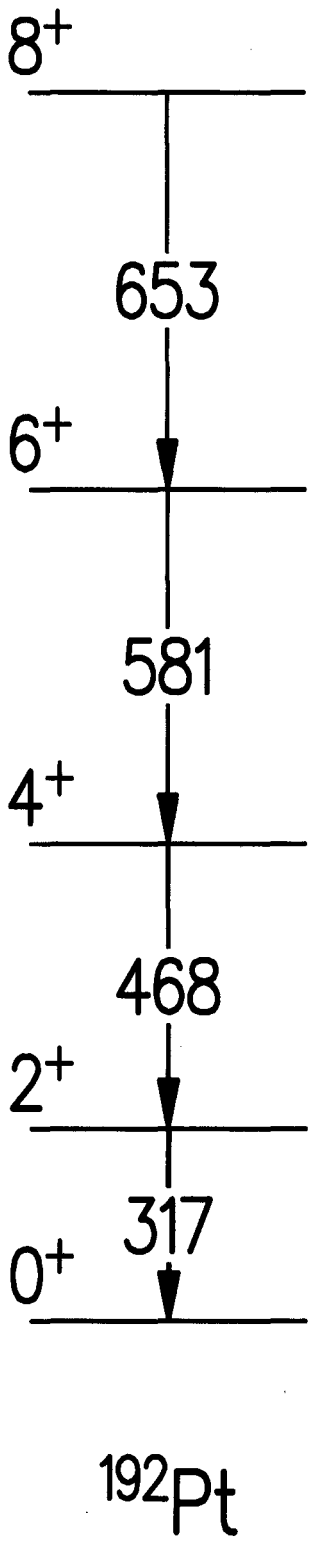

Figure B.7: Level scheme for ^{192}Pt.

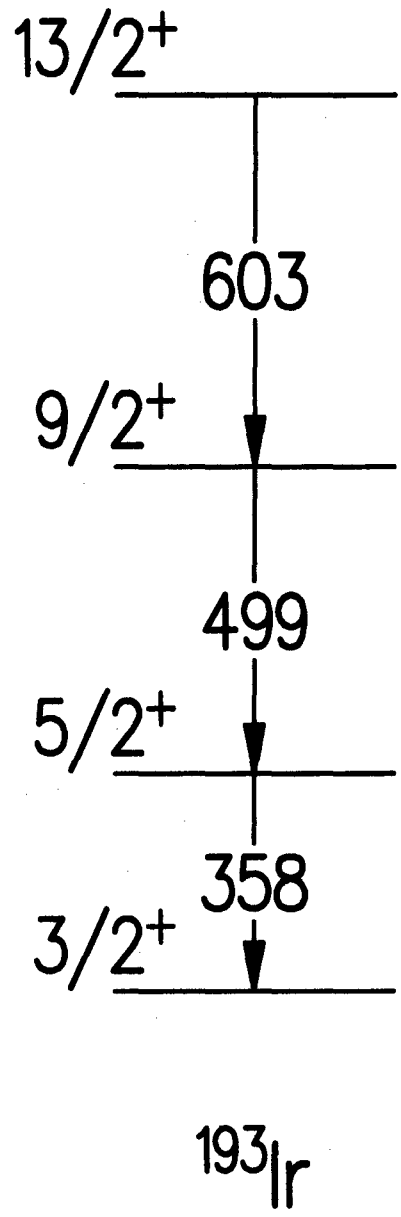

Figure B.8: Level scheme for ^{193}Ir.

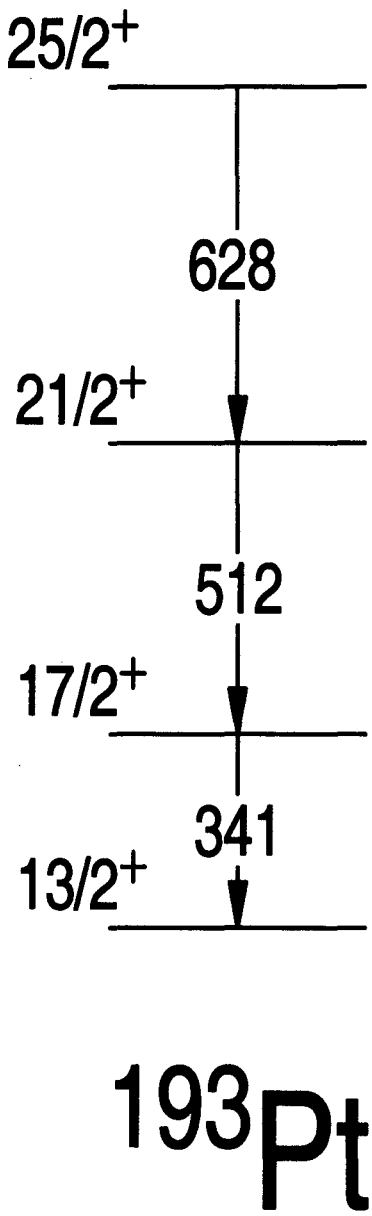

Figure B.9: Level scheme for ^{193}Pt.

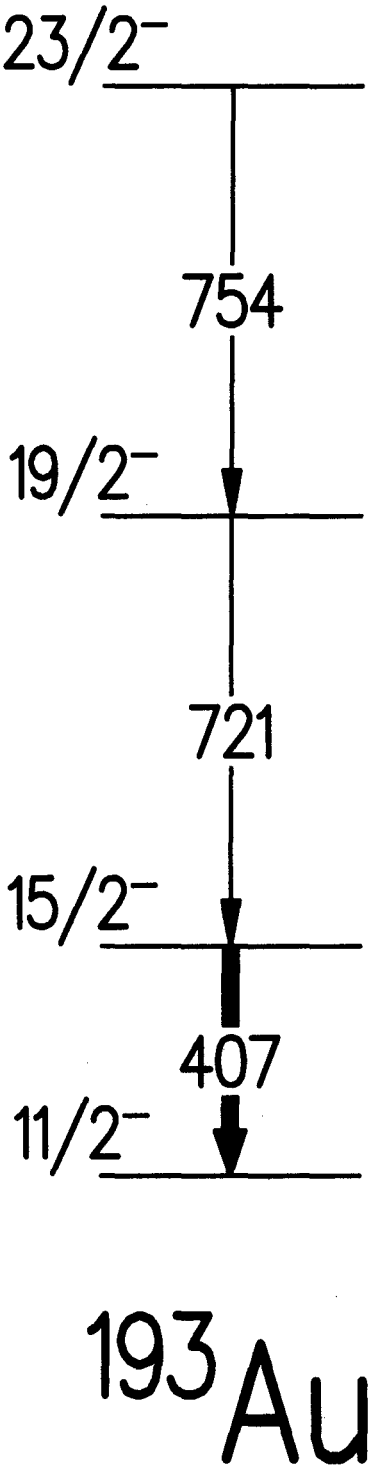

Figure B.10: Level scheme for ^{193}Au.

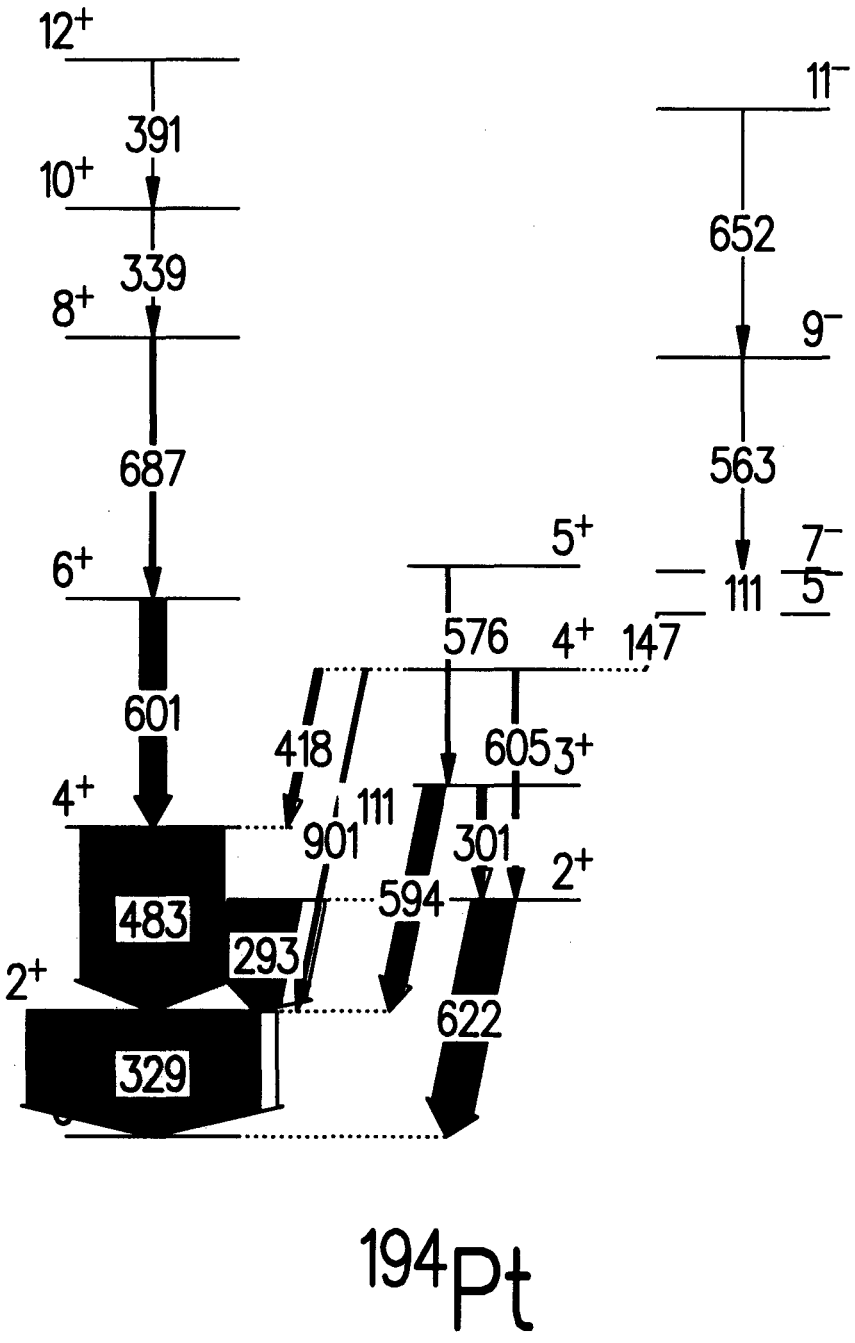

Figure B.11: Level scheme for ^{194}Pt.

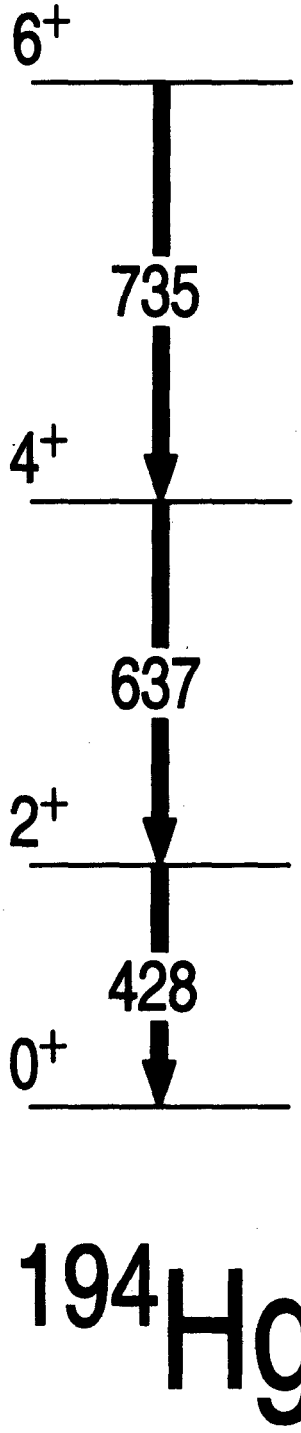

Figure B.12: Level scheme for ^{194}Hg.

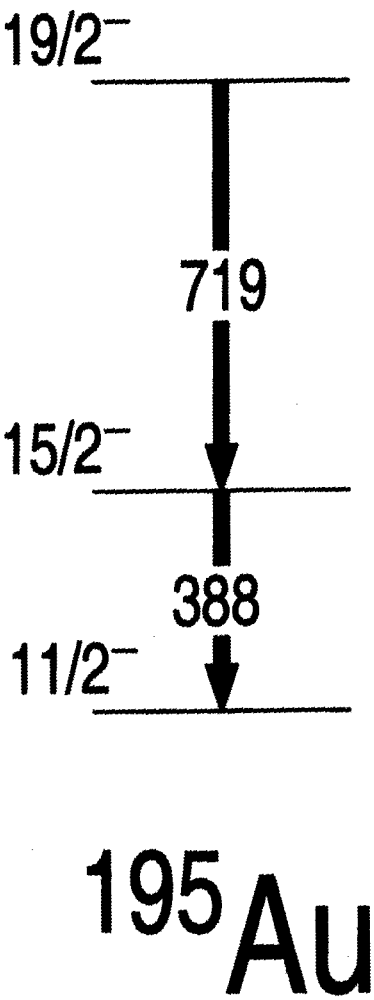

Figure B.13: Level scheme for ^{195}Au.

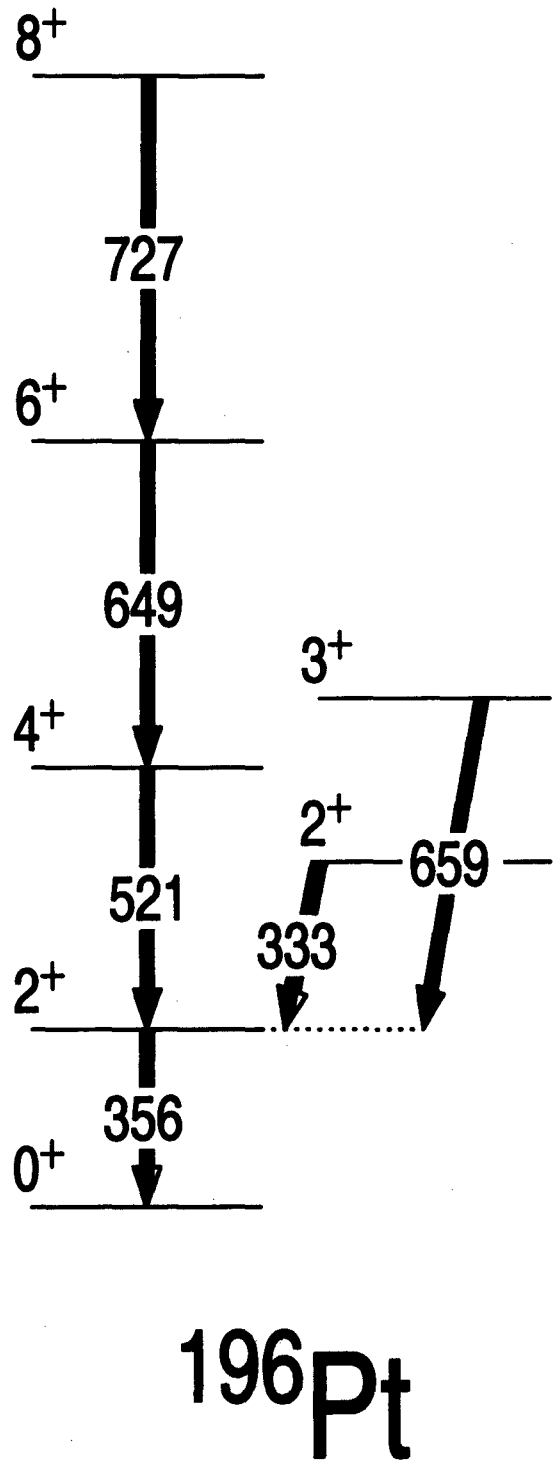

Figure B.14: Level scheme for ^{196}Pt.

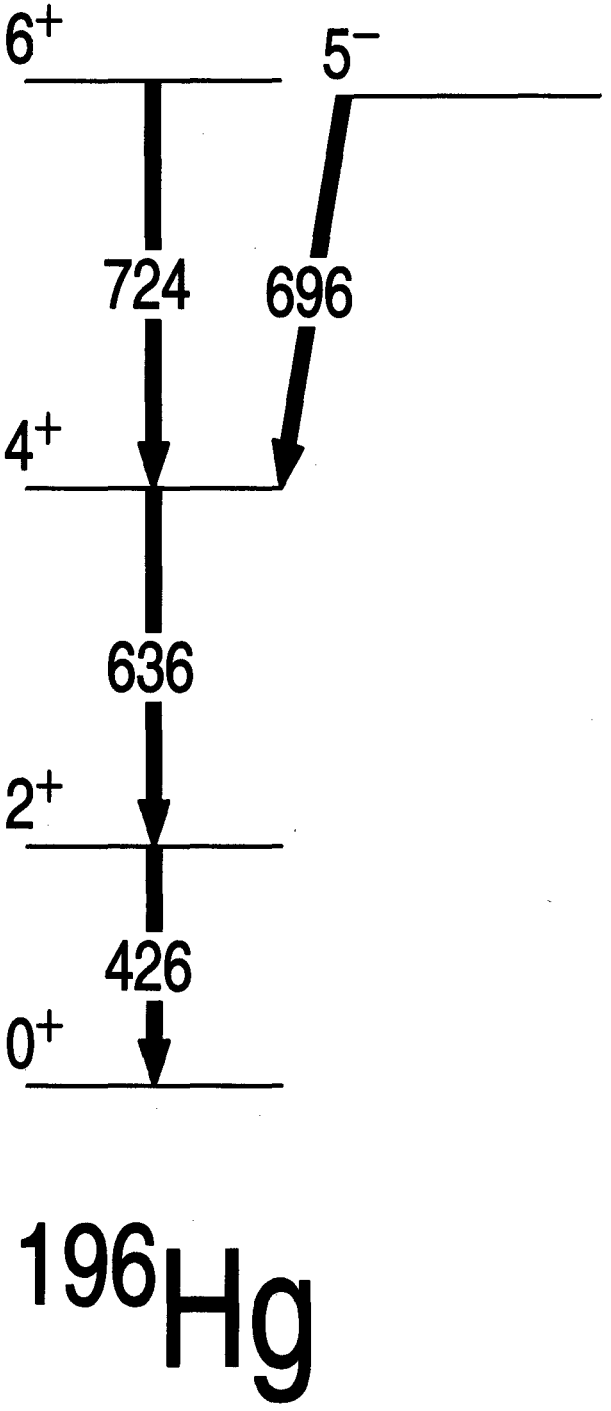

Figure B.15: Level scheme for ^{196}Hg.

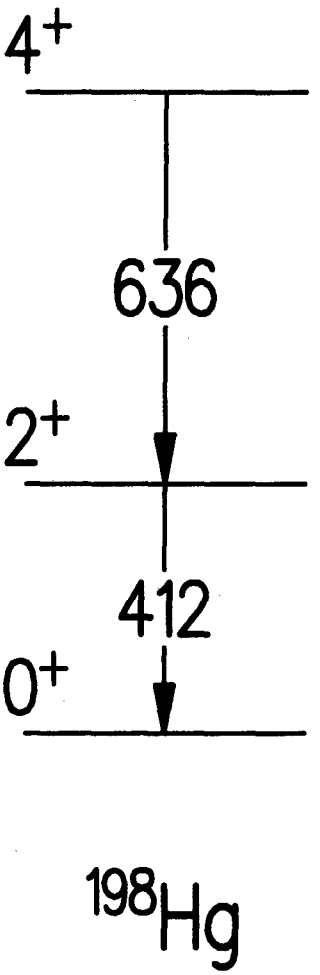

Figure B.16: Level scheme for ^{198}Hg.